THERMAL MODELS AND ENERGY SAVING STRATEGIES FOR ROTATIONAL MOLDING OPERATIONS

A Thesis

Presented to

The Academic Faculty

by

Kalyanjit Ghosh

In Partial Fulfillment

of the Requirements for the Degree

Master of Science in Mechanical Engineering

Georgia Institute of Technology

July 2004

THERMAL MODELS AND ENERGY SAVING STRATEGIES
FOR
ROTATIONAL MOLDING OPERATIONS

Approved by:

Srinivas Garimella, Chairman

Sheldon M. Jeter

Jonathan S. Colton

Date Approved: 7 / 8 / 2004

This thesis is dedicated, with heartfelt love, to

MY PARENTS

for all the love, inspiration and support they have given me over the years.

ACKNOWLEDGMENTS

First and foremost, I would like to express my sincerest gratitude to my advisor Dr. Srinivas Garimella. He gave me the idea for this project and always helped me during the course of this research. He always expected the highest quality of work and I thank him sincerely for maintaining the highest standards in all aspects of life and making this a point in every discussion.

I would also like to thank Dr. Sheldon Jeter and Dr. Jonathan Colton from the Woodruff School of Mechanical Engineering for being on my thesis committee. Their thoughtful criticism and suggestions were invaluable in preparing this document. I would also like to thank Schafer Systems Inc, Adair, IA, who supported this study through a research grant. I wish to thank all members of Sustainable Thermal Systems Laboratory (STSL) for working as a team, which made the lab more than a workplace. In alphabetical order, many thanks to: Akhil, Biswajit, Jesse, Lalit, Matt, Sangsoo, Tim and Viswanath. A special note of thanks to Viswanath, who helped me complete a section of this research while I was not doing well physically. Thanks to my roommate, Lalit, who also helped me a lot when I was not well. Guys, you were great. Last but not the least, Soumyajit, working at far off MIT, always brought in the extra inspiration. He has been much more than a friend for all these years.

Thank you all.

TABLE OF CONTENTS

ACKNOWLEDGMENTS **iv**

TABLE OF CONTENTS **v**

LIST OF TABLES **viii**

LIST OF FIGURES **x**

LIST OF SYMBOLS **xiii**

SUMMARY **xix**

CHAPTER 1:INTRODUCTION **1**

1.1 Motivation and Problem Description 1

1.2 Thesis Outline 3

CHAPTER 2:LITERATURE REVIEW **4**

2.1 Background 4

2.2 Mathematical Models of Conventional Rotational Molding 4

2.3 Alternative Heating and Cooling Mechanisms 8

2.4 Need for Further Research 9

CHAPTER 3:MATHEMATICAL ANALYSIS – BASE LINE CASE **11**

3.1 Mold Geometry and Plastic Properties 11

3.2 Molding Conditions 13

3.3 Thermal Model for the Rotational Molding Process 14

3.3.1 Stage 1: Free Convection Heating in Furnace 17

3.3.1.1 Phase 1 – Single Phase Heating 18

3.3.1.2 Phase 2 – Phase-Change Melting 22

3.3.2 Stage 2: Free Convection Cooling in Ambient 28

3.3.2.1 Phase 1 – Phase-Change Melting 28

3.3.2.2 Phase 2 – Single Phase Cooling 29

3.3.2.3 Phase 3 –Solidification 30

3.3.3 Stage 3: Forced-Convection Cooling in Ambient 34

3.4 Results and Discussion 36

3.4.1 Temperatures and Heat Transfer Coefficients 36

3.4.2 Discussion 41

CHAPTER 4: PROCESS OPTIMIZATION 48

4.1 Effect of Heating Duration 48

4.2 Effect of Pre-Cooling Duration (Post-Cooling Fixed at 23 minutes) 51

4.3 Effect of Pre-Cooling and Post-Cooling Durations (Total Cooling Constant at 46 minutes) 53

4.4 Optimal Duty Cycle 56

CHAPTER 5: MODELING OF AUXILIARY MASS AND OVERALL ENERGY CONSUMPTION 57

5.1 Introduction 57

5.2 Thermal Analysis 59

5.3 Gas Consumption Calculations 61

5.4 Results 62

CHAPTER 6: ALTERNATE HEATING AND COOLING MECHANISM 67

6.1 Proposed System Description 67

6.2 Selection of Heat Transfer Fluid 67

6.3 Thermal Models 70

6.4 Heat Transfer Fluid (HTF) Circulation Options 72

6.4.1 Heating Option A – Direct Jacket Heating 73

6.4.2 Corresponding Cooling Options 77

6.4.2.1 Open-Loop Cooling Water (Option 1) 77

6.4.2.2 Closed-Loop Cooling Water and Storage Tank (Option 2) 78

6.4.3 Heating Option B – Jacket Heating with Pre-Heat/Recuperation 80

6.4.4 Corresponding Cooling Options 82

6.4.4.1 Open-Loop Cooling (Option 3) 82

6.4.4.2 Closed-Loop Cooling (Option 4) 82

6.5 Results and Discussion 85

CHAPTER 7:CONCLUSIONS AND RECOMMENDATIONS 98

7.1 Conclusions 98

7.2 Recommendations 99

APPENDIX A 100

APPENDIX B 116

APPENDIX C 123

REFERENCES 127

LIST OF TABLES

Table 3.1:	Dimensional Inputs and Property Information	13
Table 3.2:	Molding Conditions	14
Table 3.3:	Predicted Duration of Individual Phases of the Rotational Molding Process	36
Table 3.4:	Results at end of Phase 1 of Stage 1 (Transient Heating of Powder in Furnace)	36
Table 3.5:	Results at end of Phase 2 of Stage 1 (Phase-Change Melting of Powder in Furnace)	37
Table 3.6:	Results at end of Phase 1 of Stage 2 (Phase-Change Melting of Powder in Free-Convection Cooling)	38
Table 3.7:	Results at end of Phase 2 of Stage 2 (Single-Phase Melt Cooling in Free Convection)	38
Table 3.8:	Results at end of Phase 3 of Stage 2 (Solidification of Melt in Free-Convection)	39
Table 3.9:	Results at end of Phase 1 of Stage 3 (Solidification of Melt in Forced-Convection)	39
Table 3.10:	Variation in Convective Coefficients for Rotational Molding Process	40
Table 4.1:	Cycle Times and Other Parameters for Baseline and Optimized Processes	56
Table 5.1:	Dimensional and Structural Details of the Auxiliary Mass	58
Table 5.2:	Volumes, Surface Areas and Masses of Auxiliary Housing	59
Table 5.3:	Impact of Auxiliary Housing on Energy and Fuel Consumption in Rotational Molding (Baseline and Optimized Processes)	66
Table 6.1:	Operating Temperature Ranges for Dow Fluids (Dow 2004)	69
Table 6.2:	Thermo-physical Properties of Dow Fluids at Temperatures in the Operating Range (0-350^{o}C) (Dow 2004)	70
Table 6.3:	Recuperation Fluid Details	80
Table 6.4:	Overall Comparison of Various Options	89
Table 6.5:	Heating Costs for the Various Configurations	97

Table A.1:	Geometry Calculations	100
Table A.2:	Summary of Heat Transfer Calculations for Run 30 of Single-Phase Transient Heating (2 minutes 25 seconds into Molding Process; $\Delta t = 5$ sec)	101
Table A.3:	Summary of Heat Transfer Calculations for Run 70 of Phase-Change Melting in Furnace (10 minutes 35 seconds into Molding Process; $\Delta t = 5$ sec)	102
Table A.4:	Summary of Heat Transfer Calculations for Run 20 of Phase-Change Melting in Free-Convection (18 minutes 35 seconds into Molding Process; $\Delta t = 5$ sec)	104
Table A.5:	Summary of Heat Transfer Calculations for Run 95 of Single-Phase Transient Cooling in Free-Convection (28 minutes into Molding Process; $\Delta t = 5$ sec)	106
Table A.6:	Summary of Heat Transfer Calculations for Run 25 of Phase-Change Solidification in Free-Convection (37 minutes 55 seconds into Molding Process; $\Delta t = 5$ sec)	108
Table A.7:	Summary of Heat Transfer Calculations for Run 140 of Phase-Change Solidification in Forced-Convection (51 minutes 35 seconds into Molding Process; $\Delta t = 5$ sec)	110
Table A.8:	Calculation of Individual Volumes of the Auxiliary Mass	114
Table A.9:	Calculation of Individual Surface Areas of the Auxiliary Mass	115
Table B.1:	Dimension Details of Crossflow Heat Exchanger	118
Table C.1:	Design Conditions	123
Table C.2:	Heat Exchanger Dimensions	123

LIST OF FIGURES

Figure 1.1:	Typical Rotational Molding Unit	2
Figure 1.2:	Assembly of Molds on the Frame	2
Figure 3.1:	Mold Geometry under Consideration	12
Figure 3.2:	Variation of Specific Heat of Plastic with Temperature	15
Figure 3.3:	Variation of Conductivity of Plastic with Temperature	16
Figure 3.4	Variation of Density of Plastic with Temperature	16
Figure 3.5:	Representative Segments during Melt Solidification	17
Figure 3.6:	Segmental Divisions of Mold Wall during Phase 1 of Stage 1	19
Figure 3.7:	Cross-sectional View of Mold during Phase 1 of Stage 1	19
Figure 3.8:	Energy Transfer during Phase 1 of Stage 1	21
Figure 3.9:	Segmental Divisions of Mold Wall and Plastic-Melt during Phase 2 of Stage 1	23
Figure 3.10:	Cross-Sectional View of Mold during Phase 2 of Stage 1	24
Figure 3.11:	Growth of Melt Front during Phase 2 of Stage 1	27
Figure 3.12:	Cross-Sectional View of Mold during Phase 2 of Stage 2	29
Figure 3.13:	Segmental Divisions for Phase 3 of Stage 2	30
Figure 3.14:	Cross-Sectional View of Mold during Phase 3 of Stage 2	31
Figure 3.15:	Variation in Solid and Melt Layers during Phase 3 of Stage 2	35
Figure 3.16:	Duration of Individual Phases for the Entire Cycle	37
Figure 3.17:	Temperature Profiles during the Molding Process	42
Figure 3.18:	Locations of the Melting and Solidification Fronts	45
Figure 3.19:	Variations of Masses of Molten and Solid Phases	45
Figure 3.20:	Temperature Gradient Across the Mold at Representative Times During Molding	46
Figure 3.21:	Effect of Segment Size on Temperature Predictions	47
Figure 4.1:	Energy Flows as a Function of Heating Duration	49
Figure 4.2:	Heat Transfer Rates for Various Heating Durations	49

Figure 4.3:	Variations in Masses with Different Heating Durations	50
Figure 4.4:	Energy Flows as a Function of Pre-Cooling Duration	51
Figure 4.5:	Heat Transfer Rates as a Function of Pre-Cooling Duration	52
Figure 4.6:	Variations in Masses with Different Pre-Cooling Durations	52
Figure 4.7:	Energy Flows as a Function of Pre-Cooling Duration (Fixed Total Cooling Duration)	54
Figure 4.8:	Heat Transfer Rates for Different Pre- and Post-Cooling Durations (Fixed Total Cooling Duration)	55
Figure 4.9:	Variations in Masses for Different Pre- and Post- Cooling Durations (Fixed Total Cooling Duration)	55
Figure 5.1:	Assembly of Molds in the Actual Manufacturing Process (Top and Bottom Views)	57
Figure 5.2:	Approximated Model of the Housing (Top and Bottom Views)	58
Figure 5.3:	Variation in Temperature of Auxiliary Mass (Optimized Cycle)	63
Figure 5.4:	Variation in Heat Transfer Rate with Time (Optimized Cycle)	64
Figure 5.5:	Variation in Temperature of Auxiliary Mass (Baseline Cycle)	64
Figure 5.6:	Variation in Heat Transfer Rate with Time (Baseline Cycle)	65
Figure 5.7:	Energy and Fuel Consumption for the Original and Optimized Processes	66
Figure 6.1:	Mold Cross-Section with Integral Heating/Cooling Fluid Channels	68
Figure 6.2:	HTF Flow Circulation around the Mold during Heating	68
Figure 6.3:	Variation of Specific Heat of the DOW Fluids	69
Figure 6.4:	Energy Transfer during Transient Heating of Plastic Powder	73
Figure 6.5:	Circulation of HTF during Heating (Option A)	74
Figure 6.6:	Open-Loop Cooling (Option 1)	78
Figure 6.7:	Closed-Loop Cooling with Water Storage (Option 2)	79
Figure 6.8:	Circulation of HTF during Heating (Option B)	81
Figure 6.9:	Open-Loop Cooling with Recuperation (Option 3)	83
Figure 6.10:	Closed-Loop Cooling with Recuperation (Option 4)	84
Figure 6.11:	Temperature Profile for Direct Jacket Heating and Open-Loop Water Cooling	86
Figure 6.12:	Temperature Profile for Direct Jacket Heating and Closed-Loop Cooling	87

Figure 6.13: Temperature Profile for Jacket Heating with Pre-Heat/Recuperation and Open-Loop Water Cooling 91
Figure 6.14: Temperature Profile for Jacket Heating with Pre-Heat/Recuperation and Closed-Loop Water Cooling 92
Figure 6.15: Energy Consumption for Various Configurations 93
Figure 6.16: Fuel Consumption for Various Configurations 94
Figure 6.17: Variation of Heating and Cooling Durations for Various Jacket Heating and Cooling Combinations 96
Figure A.1: Approximated Model of the Housing (Top and Bottom Views) 113
Figure B.1: Crossflow Heat Exchanger Design for the Flue Gas Heat Exchanger 116
Figure B.2: Salient Features of the Flue Gas Heat Exchanger 117

LIST OF SYMBOLS

A, *A*	cross sectional area
$air_{m^3/sec}$	air flow rate
C	constant
$cross_{sec}$	cross section of square tubes
c_h	center height
c_w	center width
C_p	specific heat
D, *D*	diameter
$E_{r,}$ E_p	enthalpies of reactants, products
Energy	energy consumption
f	friction factor
f_p	fin pitch
f_t	fin thickness
fluegas	flue gas
$fuel_{m^3/sec}$	fuel flow rate
h, *h*	height
h_{coeff}	heat transfer coefficient
h_{fusion}	heat of fusion
HTF	heat transfer fluid
k, *k*	conductivity

L, l	length
MMASS	molar mass
m	constant
m, mass	mass
N_t	number of tubes
N_c	number of centers
N_{fins}	number of fins
N_{pass}	number of tubes per pass
Nu	Nusselt number
perim	perimeter
powder	plastic powder
P_T	tube pitch
$Powder_{Height}$	height of the residual powder in the mold cavity
Pr	Prandtl number
Q_{front}	thermal energy being delivered to phase-change front
Q_j	thermal energy leaving node j
$Q_{phasechange}$	thermal energy used in phase change process
$Q_{St,j}$	thermal energy stored in node j
Ra	Rayleigh number
Re	Reynolds number
sol_{seg}	segmental thickness of solidified-melt
St	Stanton number
T	temperature
Total	total

T_{Melt}	melting point of plastic
t, *t*	thickness
thk	tube thickness
time	time
vel	velocity
vol	volume
w	width

Subscripts

Al	aluminum
air	air
amb	ambient
avg	average parameter
aux	auxiliary housing
b,a	blocked by fins
botplate	bottom plate
c	core face factor
cf	recuperative heat transfer fluid
channel	channel
connectors	steel connector tubes
conv	convection term
d, air	direct heat transfer on air-side
effect	effective parameter
f	end of a time-step
f,a	free flow factor

fl, HTF	heat transfer fluid
flow	heat transfer fluid flow
fuel	fuel
fittings	fittings
fraction	fraction
front	melt or solidification interface
furnace	furnace used for heating
fusion	fusion
housing	housing
hx	heat exchanger
hyd, *h*	hydraulic
i	inner parameter
id, air	indirect heat transfer on air-side
in	inlet
innersurface	inner surface
j	segmental node number
jacket	jacket
l	length
melt	melt
melt/powder	melt-powder interface
mold	aluminum mold
next	next time step
o	outer parameter
out	outlet

p	plastic
pl	melt form of plastic
phasechange	phase-change process
rad	radiation term
rate	rate
St	storage term
s	start of a time-step
seg	segment
sol	solidified-melt
total	total
tube	tube
wall	mold wall
width	width
wtr	water

Greek Symbols

Δp	pressure drop
Δt	duration of time step
Δ_h	heat value
δ_{pl}	time-averaged melt thickness
δ_{seg}	thickness of each melt segment
δ_{sol}	time-averaged solidified-melt thickness
ε	emissivity of mold surface
ε_f	effectiveness
$\eta_{f,air}$	fin efficiency

μ	viscosity
π	pi
ρ	density
σ	Stefan-Boltzmann constant

SUMMARY

Transient heat transfer phenomena in the rotational molding of plastic parts are modeled in this study. Natural convection and radiation from the furnace and flue gases to the mold housing are analyzed. Other models include transient heat transfer through the mold, single-phase conduction through the particulate plastic material prior to phase change, melting of the plastic and heating of the liquid pool. Subsequent staged cooling of the mold and solidification of the plastic using a combination of free and forced convection and radiation, are also modeled. Information about the properties of the plastic in powder, liquid and solid forms is obtained from the literature. Assumptions about the behavior of the plastic powder and the molten plastic during the rotational operations are made in accordance with the available literature. The mold wall, melt, and solidified plastic regions are divided into a number of finite segments to track the temperature variation with time during the molding process. The corresponding variations in masses and thicknesses of the melt and solidified plastic regions are estimated. This information is used to estimate the energy consumption rates for various phases of the process. The model is applied to a specific molding process in a commercial rotational molding plant. Parametric studies of the effect of heating and cooling durations on the plastic temperatures and the energy consumption rates are conducted. These analyses provide insights about opportunities for optimization of the heating and cooling schedules to reduce overall energy consumption and improve throughput. The heat input from the furnace reduces from 1.53 MJ for the baseline to 1.33 MJ for the optimized process for a single mold. Optimal natural and forced convection cooling schedules are proposed based on the analysis.

The overall energy and gas consumption for the rotational molding process, taking into consideration the thermal mass of the auxiliary housing (steel) required to hold the molds, is estimated on a per-batch basis. In addition, a preliminary design for an alternative system for heating and cooling the molds using a high temperature heat transfer fluid (HTF) flowing through jackets integral to the molds is proposed. The HTF provides efficient heat transfer to and from the mold and reduces energy consumption,

particularly due to the absence of the auxiliary mass of the housing that must be heated and cooled by flue gases in the conventional process. Two different options for the alternative system are considered. In the first option, the hot HTF from a system reservoir heats the batch of molds directly. In the other, in which thermal energy from the heat transfer fluid is recuperated, hot HTF from the previous cooling batch is used to pre-heat the molds, thus reducing external heat addition. For each of these two options, further energy savings are also realized by implementing waste heat recovery during the cooling stages. This recovered energy is available for supplying process heating needs in the plant. From this study, it was found that for a batch of 14 molds, the energy consumption of the base-line furnace-heated molds is 80 MJ, while 73 MJ is required in the optimized case. For this optimized case, of the 73 MJ required, 54 MJ is required for the heating of the auxiliary mass of the rotational molding apparatus. By implementing the liquid heated and cooled system, this energy consumption per batch is reduced to 25.2 MJ, much of it due to the elimination of the need to heat and cool the auxiliary mass. In addition, nearly 27% of the energy input for the jacket heating cycle (25.2 MJ) is recovered through recuperation from the cooling process and used for pre-heating the next batch. Finally, the waste heat recovery scheme enables recovery of 200 kg of water at 56^{o}C to be used in other processes in the plant.

CHAPTER 1

INTRODUCTION

1.1: Motivation and Problem Description

Rotational molding is a manufacturing process for producing hollow plastic parts. According to Crawford (1996), this process "is unique amongst plastic moulding processes because the heating, shaping and cooling of the plastic all take place inside the mould with no application of pressure." However, as Beall (1998) rightly puts it, "the technology of rotational molding has been developed by and remains concentrated among the molders, plastic material manufacturers, mold makers, and machinery builders within the industry."

In this process, molds carrying the plastic powder are mounted on the arm of the machine, which rotates about a central axis. The mold, in turn, rotates about its own (perpendicular) axis, which results in a biaxial rotational system. While in the uniformly heated furnace, the plastic melts and sticks to the inner surface of the mold cavity. After this stage, the frame housing, on which the molds are mounted, is moved to a cooling chamber, where ambient air initially cools it, followed by forced-convective cooling. The solidified plastic part retains the shape of the inner surface of the mold cavity. This process is unique because the plastic melts in the mold instead of molten plastic being forced into the mold cavity. The use of biaxial rotation of the mold during heating and cooling results in uniform heat transfer.

A typical rotational molding unit is shown in Figure 1.1. Figure 1.2 shows an assembly of molds on the frame. The main motivation behind this study is to obtain a better understanding of the thermal processes in rotational molding and reduce energy consumption where possible. In this work, numerical models are developed for the heating, melting, solidification and cooling of the plastic in the molds.

Figure 1.1: Typical Rotational Molding Unit

Figure 1.2: Assembly of Molds on a Frame

The effects of changing the heating and cooling durations of the molding cycle are investigated and energy savings opportunities are identified. The consumption of a large fraction of energy for thermal cycling of the mold housing is recognized and alternative fluid-coupled heating and cooling techniques are proposed and analyzed.

1.2: Thesis Outline

The thesis is organized as follows:

Chapter 1 introduces the basic rotational molding process and explains the motivation for the current study.

Chapter 2 reviews the literature on rotational molding processes. In particular, it lists the advantages of this process and discusses previous mathematical models. In addition, it identifies the deficiencies in the current understanding of the thermal aspects of this process, and substantiates the need for additional research.

Chapter 3 describes the mold geometry, plastic powder and properties, and the approach used for modeling the transient thermal processes. Details of the temperature profiles across the system in each phase of the process are predicted, and energy flows in a baseline process are computed from these analyses.

Chapter 4 discusses optimization techniques for the baseline process and presents an optimized duty cycle based on energy consumption.

Chapter 5 models the auxiliary thermal mass of the mold (frame) and conducts a detailed thermal analysis of the additional energy consumption due to this mass. It also analyzes the natural gas consumption for the baseline process through a simple thermodynamic analysis.

Chapter 6 discusses an alternate heating and cooling scheme using a heat transfer fluid (HTF) flowing through jackets integral to the molds. Four HTF flow options with and without recuperation and waste recovery are addressed.

Chapter 7 provides conclusions from this research and recommendations for further study.

CHAPTER 2

LITERATURE REVIEW

2.1: Background

Although the rotational molding of plastics was introduced as early as 1855 by Peters (Bruins 1971), much of the analytical work on the subject started in the 1990s. The Peters patent (No. 1301) (Beall 1998), discusses the elementary processes of this molding technique such as the biaxial rotational mechanism and the external cooling methods (Bruins 1971). With the introduction of polyethylene powders in 1958 (Bruins 1971), the rotational molding process received a big thrust, and the powdered form of polyethylene used since then resulted in products competitive in price with injection and other blow-molded items. Unlike injection and blow molding processes, this process does not involve pressure molding, and does not require coring (used primarily for water cooling), thus resulting in comparatively inexpensive parts (Bruins 1971). While low-density polyethylene (LDPE) and high density polyethylene (HDPE) were the principal materials used initially for this process, since 1980, linear low-density polyethylene (LLDPE) has become the most widely used material because its molecules retain their low density and are packed more tightly than the other strains. Additional information about the rotational molding process may be found in Bruins (1971), Beall (1998) and Crawford (1996).

2.2: Mathematical Models of Conventional Rotational Molding

Throne (1976) studied the rotational molding of a thermoplastic powder of nominal 35-mesh size. The primary emphasis in that study was on the material attached to the inner mold surface, which was considered to be in static contact with it. Heat transfer to the powder circulating in the mold cavity was neglected. A series, lumped-parameter model was used to formulate the heat-transfer equations and to plot transient temperature profiles at the mold wall and several locations within the layer of plastic.

The model, however, does not consider the heat of fusion during melting. In an earlier work by Rao and Throne (1972), an overview of the principles of the rotational molding process was provided. Specifically, a model for the molding process in a horizontal cylinder rotating about its long axis was described. They also discussed the relative importance of various process parameters such as rotational speeds, solid and liquid phase properties of the plastic being molded, and processing temperatures. Rules of thumb about the importance of these parameters were also discussed. They provided criteria for the selection of mold materials on the basis of properties such as thermal diffusivity and thermal conductivity, and presented transient temperature profiles for the mold. Through the analysis of the liquid phase, they pointed out that there is little bulk liquid flow within the mold, and also analyzed the importance of surface wetting and capillary forces.

Gogos *et al.* (1998) developed a theoretical model for the rotational molding process, and also identified the key dimensionless groups that affect processing time. These groups are as follows: 1) Dimensionless powder-end time; 2) Dimensionless plastic melting temperature; 3) Plastic-to-mold thermal capacitance ratio; 4) Inside-to-outside heat transfer coefficient ratio; 5) Dimensionless energy required for phase change; 6) Dimensionless plastic conductance; 7) Mold curvature effect; 8) Dimensionless mold conductance; and 9) Plastic curvature effect. These groups were defined to account for the influence of physical, thermal, and geometrical properties. The theoretical model was solved using a differential numerical approach as well as a lumped-parameter approximation for the heating and phase-change melting processes. They assumed a set of base-case model parameters obtained from the literature (Tadmor and Gogos 1979; Griffith and Nassersharif 1990; Nugent *et al.* 1992) for polyethylene powder rotationally molded within a steel mold. They compared the results from these two models with experimental data from Nugent (1990) and found good agreement between their two models and these data. However, the study analyzed only the single-phase heating and the phase-change melting process until the powder melts and deposits on the mold wall (subsequent solidification and cooling were not investigated). The non-dimensional powder-end time was plotted versus each dimensionless group, keeping the remaining variables constant at the values corresponding to the base case parameters. It

was found to depend mainly on the following four dimensional groups: 1) Dimensionless plastic melting temperature; 2) Plastic-to-mold thermal capacitance ratio; 3) Dimensionless energy required for phase change; and 4) Dimensionless plastic conductance.

In another study (Olson *et al.* 1997), the same group of investigators introduced a finite-element scheme known as the Arbitrary Lagrangian Eulerian technique to model the set of non-linear heat transfer equations. As in their previous work, the study analyzed only the single-phase heating and the phase-change melting processes. The temperatures predicted in this work were within 1 percent of the results from their previous finite-difference models; however, they were only in fair agreement with the experimentally obtained data of Nugent (1990), some of the discrepancy being attributed to the temperature measurement techniques. Using identical mold properties and convective heat transfer coefficients, they also implemented a fully implicit scheme with central difference approximations for the space derivatives in another study (Gogos *et al.* 1997) to obtain results that yield similar agreement with the same experimental data. In a later paper (Olson *et al.* 1998), they utilized the axisymmetric Arbitrary Lagrangian Eulerian technique to model the moving plastic interface during the heating and melting phases. It was inferred from their findings that the plastic deposition rate was non-uniform inside the mold, which resulted from large variations in mold temperatures over the rotational molding cycle. They concluded that transient local heat transfer phenomena and changes in plastic layer thickness must be accounted for in future models.

Sun and Crawford (1993) obtained the temperature profiles for the rotational molding process for a variety of mold materials using simulation programs developed by them. They also conducted experiments on single-axis rotation of a cylindrical mold, and biaxial rotation of a cube mold. These tests showed that rotational speed was not particularly significant in determining temperature profiles, which led them to treat the powder bed as a static system in their analyses. They found that the experimentally observed trends were qualitatively similar to those predicted by their simulations. They used their predictive tools to investigate supplementation of the rotational molding process with internal heating and cooling in an effort to shorten the processing time.

Other parametric analyses were also conducted, which showed that LLDPE requires a shorter furnace time than HDPE due to its lower melting point and latent heat of fusion.

Xu and Crawford (1994) modeled the entire molding cycle using a transient, non-linear heat transfer model that incorporates the biaxial motion of a hollow mold containing a powder mass. In modeling the various stages of the molding process, they assumed the powder inside the mold as static and treated the rotational molding process as one-dimensional. Numerical results from their simulations were in very good agreement with experimental data for Enichem RP246H resin for various product thicknesses. Nugent *et al.* (1992) also predicted heating/cooling rates and overall cycle times for rotational molding, and demonstrated good agreement with experimental results (Nugent 1990; Crawford and Nugent 1992) for a variety of plastics. They found that increasing the furnace temperature during the molding process does not yield commensurate decreases in cycle times, and that furnace time increases linearly with wall thickness of the product being molded.

Attaran *et al.* (1998) reviewed research on rotational molding to develop a comprehensive model for the heat transfer mechanism. They assumed that the bulk of the plastic powder is statically contacting the mold at all times. In their work, they used an Alternating Direction Implicit Method to discretize the heat transfer equation, and compared the temperature predictions across the mold with results from full-scale rotational molding equipment. The melting rate was found to decrease with time as a result of the decrease in the temperature difference between the layers of powder closer to the mold surface and other layers adjacent to the powder-air interface.

Bellehumeur and Tiang (2002) focused on the non-isothermal melt densification during the rotational molding of polyethylene assuming the temperature profile in the melted polymer to be linear. Their simulation simultaneously addressed heat transfer, polymer sintering, and bubble dissolution. They found that particle size and packing density are most significant in determining the densification. High viscosity resins were found to contain large bubbles, resulting in lower density parts, but this effect was found to decrease as the particle size decreased. They also found that reductions in cycle time could come at the expense of the densification process.

2.3: Alternative Heating and Cooling Mechanisms

According to Farrell *et al.* (1996), heating models for rotational and injection molding processes using hot oil have been looked into by Frados (1976) as early as 1976. However, "until recently, such systems have restricted operation to temperatures near 150^{o}C and have not considered energy storage and recovery." Initially, Farrell *et al.* considered both hot air and oil as potential thermal energy sources. Air flowing through channels in the mold provided higher safety over that for oil. However, air is a poor heat transfer medium and has a lower heat transfer rate. The development of newer heat transfer fluids, which perform at significantly elevated temperatures close to 315^{o}C and also result in very high heat transfer coefficients of up to 3400 W/m^{2}-^{o}C, have prompted a closer look at these fluids. Farrell *et al.* considered the preliminary design of an energy storage and recovery setup which was linked with the molding unit. The setup consists of multiple tanks storing the heat transfer fluid at various temperatures. These are arranged sequentially on the basis of the temperature of the fluid. The heating and cooling processes are continued by switching sequentially to hotter and cooler tanks respectively. The authors state that the success of this system lies in the fact that it couples energy savings and lower cost along with a reduction in the overall size of the system. In addition, they discuss design obstacles related to fluid flow, heat transfer and other safety issues including possible leakage problems of the heat transfer fluid under pressure. This design intends to "result in the fabrication of a system prototype." The proposed design configuration for the prototype allows for up to a $0.62 \times 0.62 \times 0.62$ m^{3} mold with a mold weight not to exceed 90 kg. The authors also predict that the proposed unit is capable of recovering close to 65% of the process energy associated with conventional molding units and subsequently reuse the energy to heat the mold.

In another study, Krott (1995) presents a comparison between hot oil and the conventional furnace heating. In the hot oil heating, the fluid flows through passages either attached or integral to the mold. Considering a two-dimensional thermal model, the commercial ANSYS software package was used to model the transient heat transfer equations. Similar to Farrell *et al.* (1996), Krott contends that one of the major advantages of the hot oil system is that a portion of the thermal energy input can be

recovered. This study predicts that at least 50% of the energy used to heat the mold can be recovered for use in the subsequent cycle.

Merrill (1979) confirms the effectiveness of energy conservation in a small, scaled-down version of a conventional rotational molding unit. As compared to conventional furnaces of ratings 2.34 MW (8.0×10^6 BTU/hr), the rating of the furnace used in the experiments was only 0.293 MW (1.0×10^6 BTU/hr). In this study, the hot air exhaust is redirected to pass through a heat exchanger and is capable of heating 4.16E-2 m^3 (11 gallons) of water per minute from 32.22^{o}C (90^{o}F) to 60^{o}C (140^{o}F). Considering an exhaust air temperature from this rotational molding furnace of 276.67^{o}C (530^{o}F), this setup was capable of recovering close to 50.12 kW (171,000 BTU/hr) by heating water. Assuming that the hot water is used 24 hours per day for a 200 day heating season, an annual saving of almost $2700 was predicted over normal heating using a gas-fired boiler that is 60% efficient. The paper recognizes that for maximum energy savings, the recovered heat should be used to pre-heat the combustion air in the furnace.

2.4: Need for Further Research

It can be seen from the above discussion of the mathematical modeling of the conventional rotational molding process that the issue of thermal energy transfer during the various stages of the overall cycle has not received adequate attention. Some studies have ignored the latent heat of fusion during the melting process, while most have not addressed the solidification and cooling stages. Numerical studies give some indication of the important parameters that govern the molding process; however, essential information about the cycle times and energy flows during each phase is still missing. These issues are particularly important from the viewpoint of achieving high production rates while minimizing energy consumption. Therefore, the present work conducts a comprehensive analysis of the thermal processes for the entire cycle. In particular, the phase-change processes (melting and subsequent solidification) and the corresponding latent heats are accounted for, unlike some of the prior work that ignore this aspect. Data from a commercial molding plant are used to corroborate assumptions and predictions. The movement of the melt and the solid “fronts” during the melting and solidification processes are analyzed, which provides a clearer understanding of the process, and more

accurate estimates of the transient temperature profiles and thermal energy transfer rates. In addition, cycle times for each of the individual stages of the process are better estimated due to these detailed simulations.

It is also expected that in the conventional rotational molding process, a significant fraction of the aggregate thermal energy is consumed in heating up the auxiliary mass required for the rotation along with the batch of molds. However, there have only been a few studies of alternate heating schemes even though the energy recovery from these processes has been predicted to be high. In the present study, therefore, a heating and cooling scheme that uses a heat transfer fluid flowing through small channels integral to the mold is investigated as an alternative to the conventional process. A detailed description of the analytical models and results is presented in the subsequent chapters.

CHAPTER 3

MATHEMATICAL ANALYSIS – BASE LINE CASE

A description of a model for a baseline rotational molding cycle is provided in this chapter.

3.1: Mold Geometry and Plastic Properties

A photograph of a plastic part molded in large volumes by a commercial rotational molding company is shown in Figure 3.1, along with an approximation of the corresponding mold as a hollow rectangular aluminum object for the development of the present model.

Finely mixed LLDPE powder is placed in the mold. According to Xu and Crawford (1994), the density of solid Enichem RP246H, which is a medium density polyethylene (MDPE), is 937 kg/m^3, whereas the density of the corresponding powder (i.e., after accounting for the void fraction) is 336 kg/m^3. In the absence of detailed information about the LLDPE considered here, and in view of the similarities between these two powders, these values were used to compute the volume occupied by the powder in this study. It should be noted that the melting point of LLDPE (126.5^{o}C) (Liu *et al.* 1998) is almost the same as that of the MDPE (126.4^{o}C) (Xu and Crawford 1994) for which the properties are available in greater detail.

Dimensional specifications of the mold and property information for the plastic are listed in Table 3.1. Based on this geometry, the dimensions of the inner surface of the mold (denoted by l_i, w_i and h_i) can be determined. Thus, the internal volume of the mold (vol_i) is calculated to be 4.0×10^{-3} m^3. At the beginning of the molding process, the plastic powder and the mold are at the room temperature. For an initial charge of 1.361 kg of LLDPE, the volume occupied by the powder at a density of 336 kg/m^3 (Xu and Crawford 1994), is approximately 4.0×10^{-3} m^3, essentially filling the entire volume of the mold.

The mass of the aluminum mold (m_{mold}) is obtained as the product of its volume (2.116E-03 m^3) and density (2702 kg/m^3), to be 5.718 kg (Appendix A).

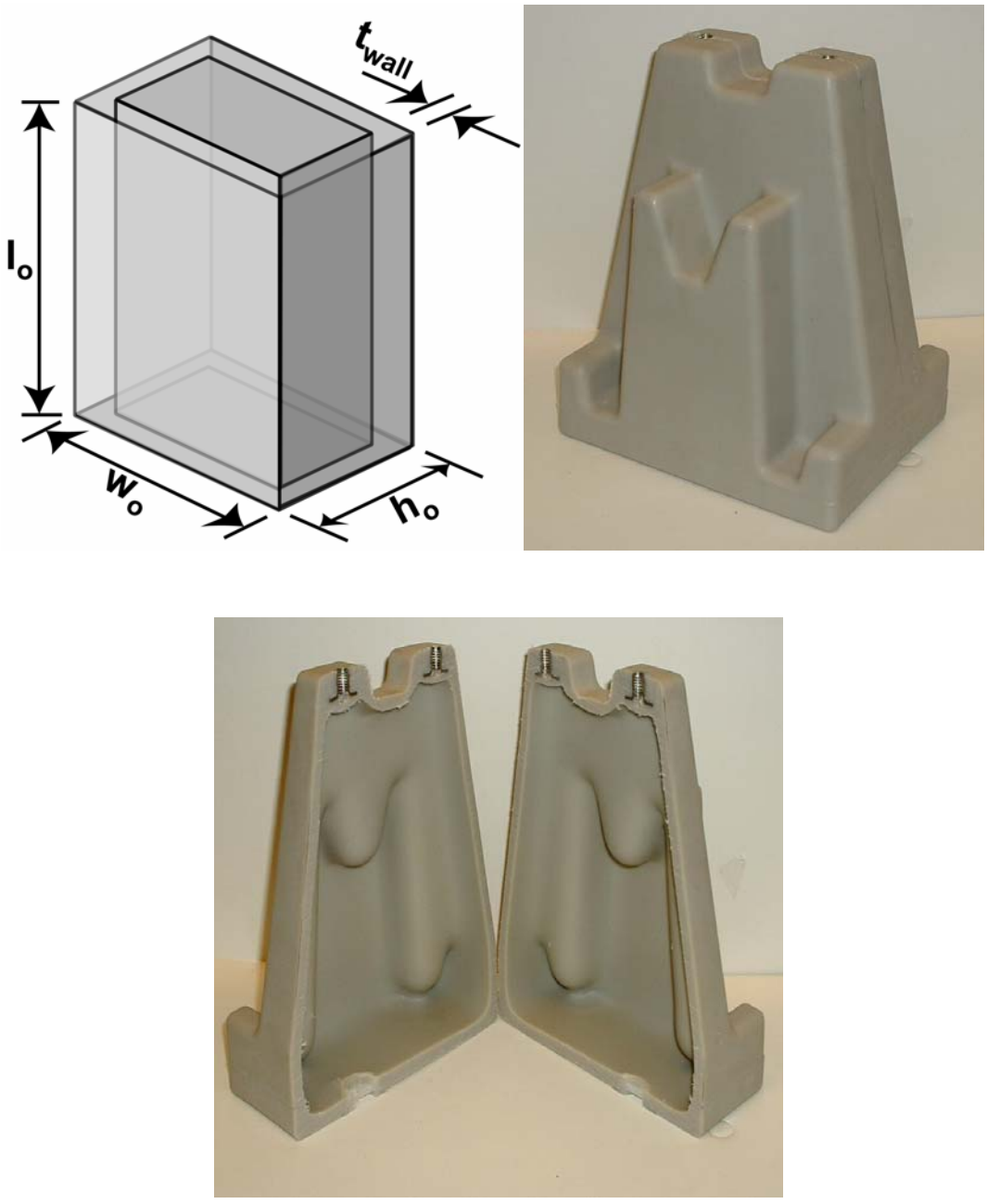

Figure 3.1: Mold Geometry under Consideration

Table 3.1: Dimensional Inputs and Property Information

Mold Information	
Material	Aluminum
Outer Height (h_o)	0.10 m
Outer Width (w_o)	0.19 m
Outer Length (l_o)	0.31 m
Wall thickness (t_{wall})	11 mm
Plastic Information	
Material	LLDPE
Mass of Plastic Powder (m_p)	1.361 kg
Density of Plastic Powder (ρ_p)	Varies with temperature (Xu and Crawford 1994)
Specific Heat of Plastic ($C_{p,p}$)	Varies with temperature (Xu and Crawford 1994)
Conductivity of Plastic (k_p)	Varies with temperature (Xu and Crawford 1994)
Heat of Fusion (h_{fusion})	133200 J/kg (Liu and Tsai 1999)
Melting Point (T_{Melt})	126.5^{o}C (Liu *et al.* 1998)

The areas of the outer ($A_{o,mold}$) and inner ($A_{i,mold}$) surfaces of the mold are estimated for calculating the average area for heat transfer across the mold thickness. Using the dimensions in Table 3.1, these areas are 0.218, 0.168 and 0.193 m^2, respectively. (Appendix A, Table A.1).

3.2: Molding Conditions

The molding process starts with the mold and the powder initially at room temperature (27^{o}C). The furnace is maintained at a constant temperature $T_{furnace}$ = 343°C during the heating phase (Stage 1), which nominally lasts 17 minutes. This is followed by an initial, natural convection cooling phase (Stage 2) for 23 minutes, and a subsequent forced convection cooling phase (Stage 3) for another 23 minutes, as summarized in Table 3.2. Models for these individual stages are described below.

3.3: Thermal Model for the Rotational Molding Process

Previous investigators (Throne 1976; Sun and Crawford 1993) have stated that the rotational molding process can be modeled using "static" models, because the experimental results of Crawford and Scott (1985) and Scott (1986) show that the speed of rotation in the molding process has a negligible effect on the temperature profiles.

Table 3.2: Molding Conditions

Molding process divided into 3 stages	
Heating (Stage 1)	Free-convection and radiation heating of mold in furnace (Duration = 17 minutes)
Pre-Cooling (Stage 2)	Free-convection and radiation cooling of mold by ambient air (Duration = 23 minutes)
Post-Cooling (Stage 3)	Forced-convection and radiation cooling of mold by ambient air (velocity of air assumed to be 5 m/sec) Duration = 23 minutes

This assumption was also made in the present study, along with the assumption that in the powder form, the entire charge of plastic (LLDPE) in the mold is well-mixed due to the rotation, and therefore at a uniform temperature. Similar assumptions have been made by Gogos *et al.* (1998) and Olson *et al.* (1998). It should be noted that the thermal properties of the plastic undergo sharp changes during the heating and cooling stages due to the phase change and also due to the densification as the plastic changes from a loose powder to a dense solid. These variations have been documented by Xu and Crawford (1994), and were accounted for in the present study. Temperature-based variations of the properties (specific heat, conductivity and density) (Xu and Crawford 1994) of the plastic are shown in Figures 3.2, 3.3 and 3.4 respectively. It can be seen that the specific heat of the plastic changes from a value of around 1860 J/kg-K at room temperature to a steep spike (~ 17,090 J/kg-K) at the melting point, followed by a stable value of about 2490 J/kg-K for $T > 134^{o}C$. Similarly, as the plastic undergoes the transformation from powder to liquid form, its thermal conductivity changes sharply near the melting point from about 0.10 W/m-K to 0.277 W/m-K. The variation in density is in fact dependent on whether the plastic is being heated or cooled, presumably because of

the powder form as the initial stage in heating, and the densified solid form at the end of the process. Thus the density of the powder is 336 kg/m^3 until about 100^{o}C, at which point it starts rising steeply to a value of 860 kg/m^3 over the temperature range 120^{o}C to 135^{o}C. Beyond this temperature, the density remains relatively constant. As the liquid is cooled and solidified, the density rises further to a value of about 932 kg/m^3.

Figure 3.5 shows a schematic of the model at a representative time step in the process that includes the mold wall, the solidified plastic, and a melt layer. Each of these zones is discretized into multiple segments to capture the temporal and spatial variations throughout the process. Due to the large thermal conductivity of the mold, it is discretized into only three segments, while the solid and melt regions of the plastic are divided into five segments each, for a total of 13 segments. The plastic powder is modeled as a convective resistance of coefficient $h_{coeff,p}$ = 5 W/m^2-K (Gogos *et al.* 1998). Iterative computations over constant time steps are conducted throughout the domain over the entire heating and cooling process.

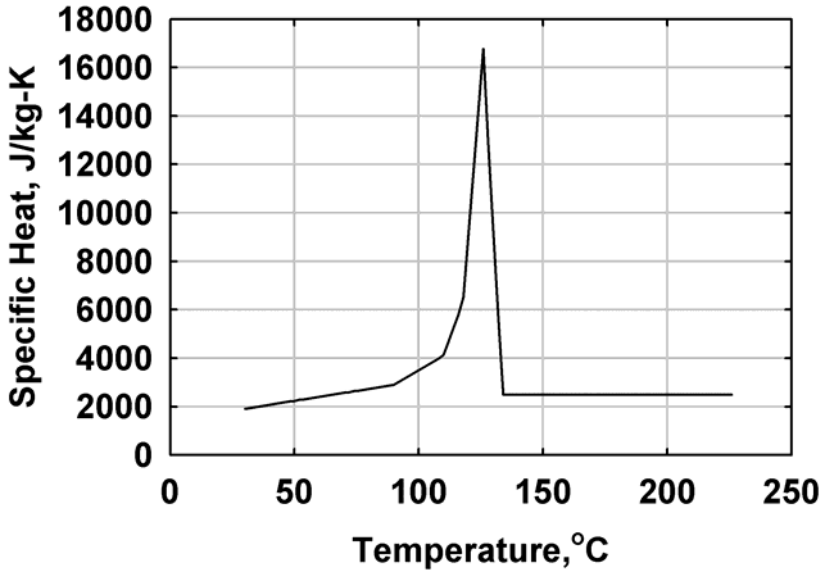

Figure 3.2: Variation of Specific Heat of Plastic (Enichem RP246H) with Temperature

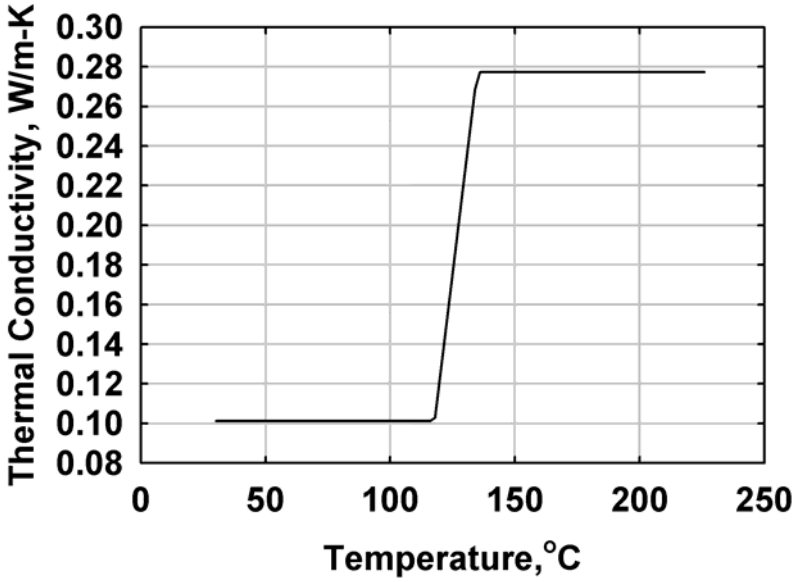

Figure 3.3: Variation of Conductivity of Plastic (Enichem RP246H) with Temperature

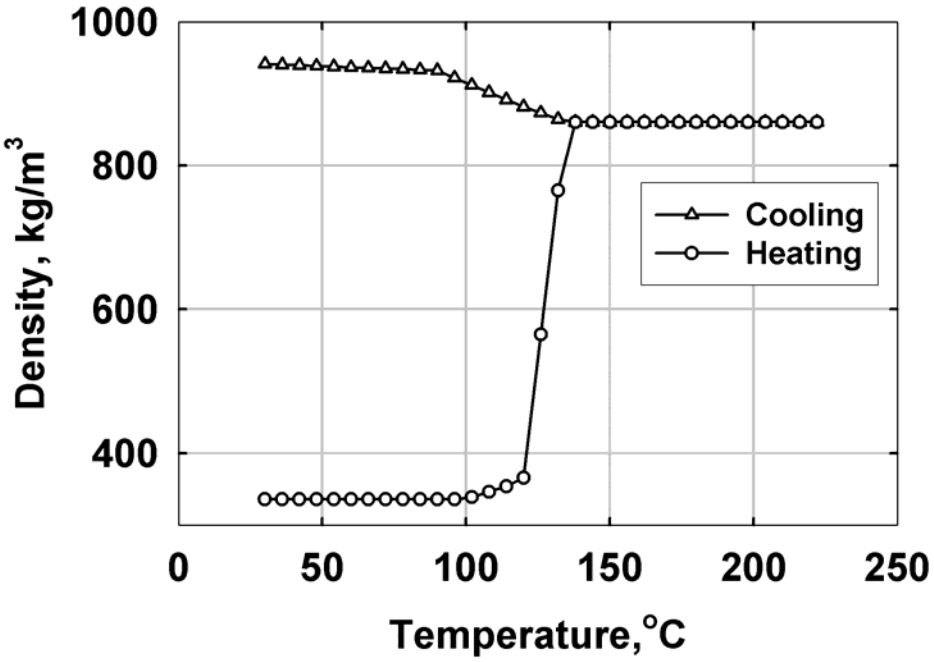

Figure 3.4 Variation of Density of Plastic (Enichem RP246H) with Temperature

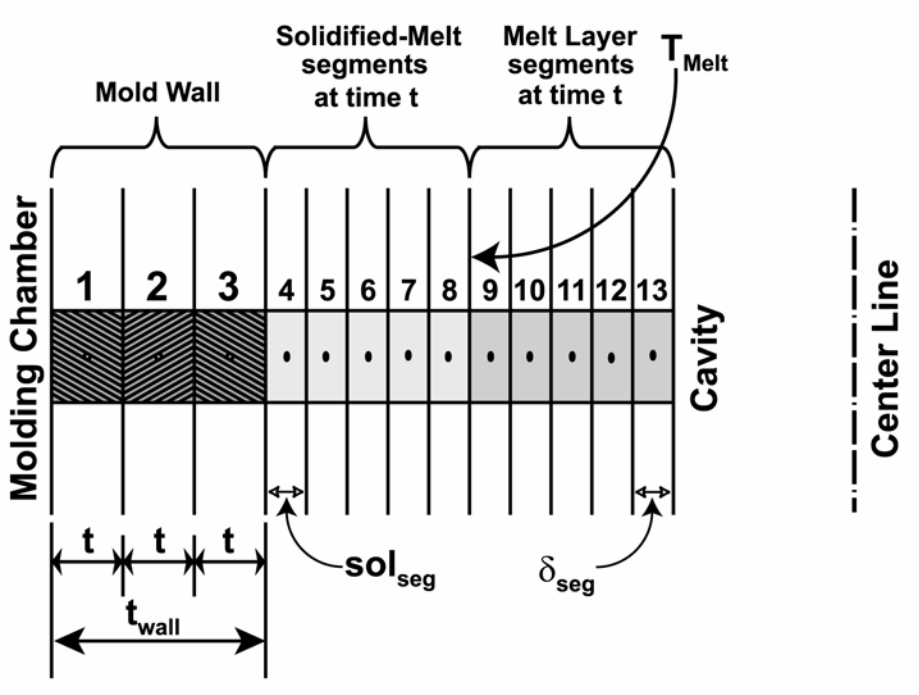

Figure 3.5: Representative Segments during Melt Solidification

3.3.1: Stage 1 – Free Convection Heating in Furnace

Stage 1 constitutes the heating cycle of the rotational molding process. It begins with the transient heating of the mold with the plastic powder in the cavity. As the inner surface of the mold reaches the melting point temperature of the plastic (T_{Melt}), the latter, which is in contact with the mold inner wall, melts and sticks to the surface. Hence, the heat transfer model for Stage 1 can be divided into two phases. During Phase 1, the transient heat conduction problem is analyzed until the mold inner wall reaches the melting point of the plastic. At this point, a second phase (Phase 2) is initiated, in which the plastic in contact with the inner wall begins to melt and sticks to the wall surface. This phase continues until the end of the heating process (17 minutes in total). A detailed description of the thermal analysis for each individual phase follows.

3.3.1.1: Phase 1 – Single Phase Heating

Due to the biaxial rotation of the mold, the heat transfer from the furnace to the mold outer wall is assumed to be uniform over the outer surface of the mold. The mold wall is divided into three segments of equal thicknesses ($t = t_{wall}/3$) as shown in Figure 3.6 and it is assumed that the temperature of each segment is spatially uniform at any specified time. Also, in this phase, the mold cavity is entirely filled up with the plastic powder as shown in Figure 3.7.

Time-averaged temperatures for the mold wall (nodes 1, 2, and 3) are obtained as:

$$T_j = \left(\frac{T_{j,s} + T_{j,f}}{2} \right) \tag{3.1}$$

where $T_{j,s}$ and $T_{j,f}$ denote temperatures at the start and finish for the j^{th} node, where j = 1, 2, and 3 respectively. Similarly, for the plastic powder:

$$T_p = \left(\frac{T_{p,s} + T_{p,f}}{2} \right) \tag{3.2}$$

The conductivity (k_{mold}) and specific heat ($C_{p,mold}$) of the aluminum mold are calculated at time-averaged temperature of the middle node (T_2). These properties are assumed to be constant for each segment of the mold for a particular time step.

The natural convection heat transfer coefficient on the outside of the mold is calculated using the Churchill and Chu (1975) correlation. Thus, the Nusselt number is given by:

$$Nu_L = \left\{ 0.825 + \frac{0.387 Ra_L^{1/6}}{\left[1 + (0.492/Pr)^{9/16} \right]^{8/27}} \right\}^2 \tag{3.3}$$

where an average of the width (w_o) and depth (h_o) of the mold is used as the characteristic length (L) for this correlation to account for the biaxial rotation. The convective coefficient ($h_{coeff,o}$) is calculated from this Nusselt number as follows:

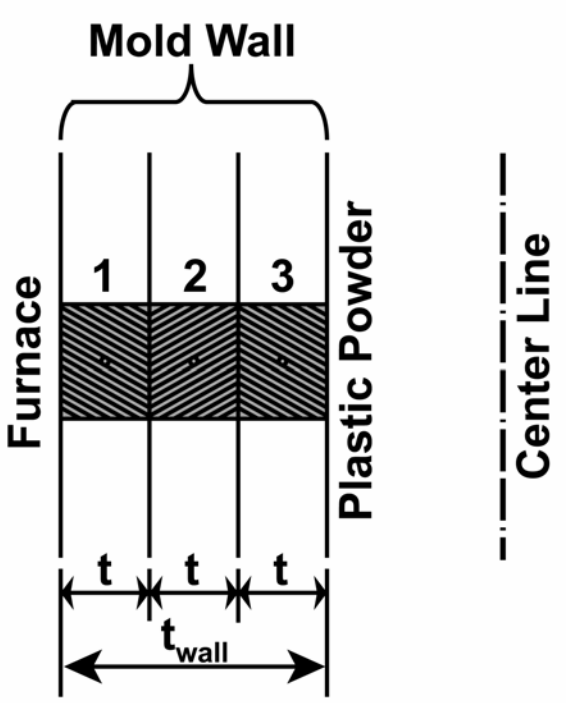

Figure 3.6: Segmental Divisions of Mold Wall during Phase 1 of Stage 1

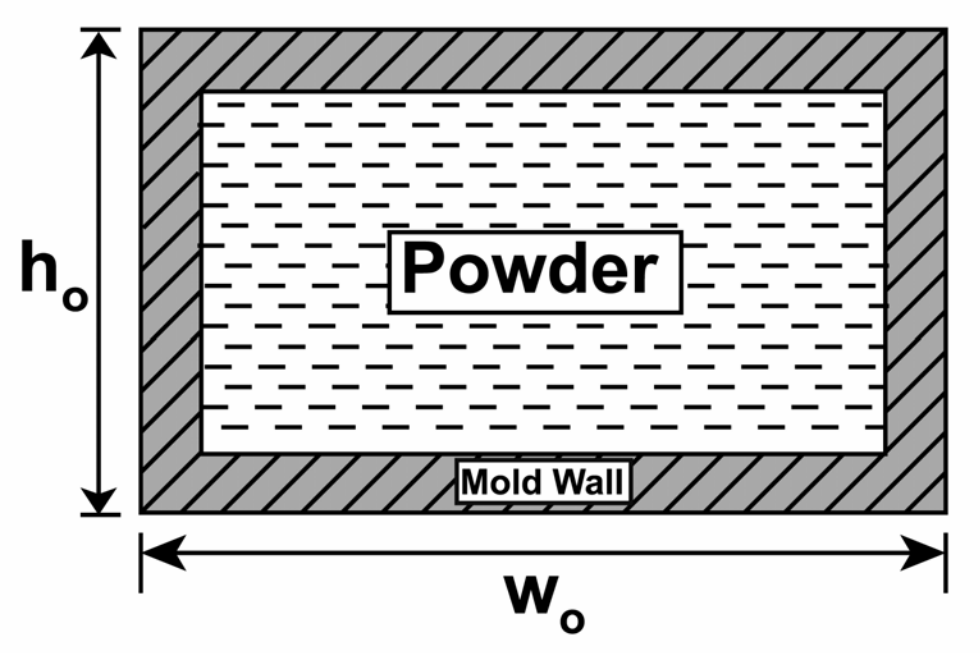

Figure 3.7: Cross-sectional View of Mold during Phase 1 of Stage 1

$$h_{coeff,o} = \frac{Nu_L k_{air}}{L} \tag{3.4}$$

The convective heat transfer coefficient on the outer wall ranges from 6.0-8.6 W/m^2-K during this stage. Thus, the radiative and convective heat transfer terms to the outer wall of the mold from the furnace are represented as:

$$Q_{rad} = \varepsilon\sigma \cdot A_{o,mold} \cdot \left(T_{furnace}{}^4 - T_1{}^4\right) \tag{3.5}$$

and:

$$Q_{conv} = h_{coeff,o} \cdot A_{o,mold} \cdot \left(T_{furnace} - T_1\right) \tag{3.6}$$

respectively, where the emissivity ε of the mold surface is assumed to be 0.9. The sum of these two gives the total heat input to the outer node (node 1) from the furnace, denoted by Q_0 ($Q_0 = Q_{rad}+Q_{conv}$). The general expression for the heat conducted through the segments of the mold is:

$$Q_j = \left[\frac{T_j - T_{j+1}}{t/\left(k_{mold} A_{mold}\right)}\right] \tag{3.7}$$

where j = 1, 2. Also, the thermal energy stored in each of the nodes is equal to:

$$Q_{St,j} = \left(\frac{m_{mold}}{3}\right) \cdot C_{p,mold} \cdot \left(\frac{T_{j,f} - T_{j,s}}{\Delta t}\right) \tag{3.8}$$

where, j = 1, 2, 3 and Δt is the duration of the time step.

In these expressions, Q_j and $Q_{St,j}$ denote the thermal energy leaving node j and stored in node j respectively. This notation is uniform throughout the entire analysis. The heat transfer processes for Phase 1 are illustrated in Figure 3.8. Hence, an energy balance for the 1st, 2nd, and 3rd nodes yield:

$$Q_0 = Q_{St,1} + Q_1 \tag{3.9}$$

$$Q_1 = Q_{St,2} + Q_2 \tag{3.10}$$

and:

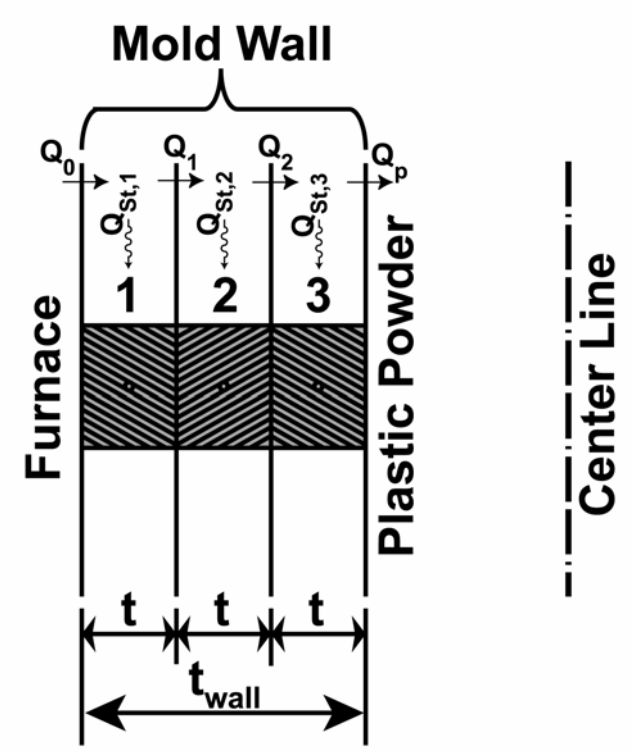

Figure 3.8: Energy Transfer during Phase 1 of Stage 1

$$Q_2 = Q_{St,3} + Q_p \tag{3.11}$$

respectively, where, Q_p is the heat convected to the mass of plastic powder inside the cavity. This convected heat can also be represented as:

$$Q_p = h_{coeff,p} \cdot A_{i,mold} \cdot \left(T_3 - T_p\right) \tag{3.12}$$

where $h_{coeff,p}$ = 5 W/m^2-K is the convective coefficient for a well-mixed powder (Gogos *et al.* 1998). This thermal energy transferred from the mold wall is also the energy stored in the powder as follows:

$$Q_p = m_p \cdot C_{p,p} \cdot \left(\frac{T_{p,f} - T_{p,s}}{\Delta t} \right) \tag{3.13}$$

The above equations are solved simultaneously to obtain the temperatures ($T_{1,f}$, $T_{2,f}$, $T_{3,f}$, $T_{p,f}$) at the end of each time-step, which in turn serve as the initial conditions for the subsequent time step. Phase 1 concludes once the inner surface of the mold

reaches the melting point of the plastic, at which point, the plastic starts adhering to the mold as melt.

3.3.1.2: Phase 2 – Phase-Change Melting

As melting progresses, the plastic powder continues to be deposited as melt on the inner surface of the mold, layer by layer, until the entire inventory of the powder melts, leaving a cavity at the center.

As stated above, to enable greater accuracy in tracking the temperature variation in the melt, it is divided into five segments of equal thickness. It should be noted that due to the transient nature of the melting process, the thickness of the melt, and therefore, the individual segments, increase as the melting proceeds. Similarly, the surface area for the heat transfer across the melt changes as the inner perimeter of the melt decreases due to its continuous build up, and is updated in each time step. Masses of each melt segment are calculated based on its thickness and the corresponding melt volume, and its density at the time-averaged temperature for the time increment under consideration. The segmental division and the cross-sectional view of the mold for Phase 2, Stage 1 are shown in Figures 3.9 and 3.10 respectively.

As before, the time-averaged temperatures T_j, j = 1,…,8 of the mold and the melt, and T_p for the powder are computed. Radiative and convective heat transfers from the furnace to the outer mold surface, conductive heat transfer through the mold, and heat storage terms within the mold are similar to Phase 1 (similar to Equations 3.5 - 3.11 respectively). It should be noted that for node 3, instead of heat transfer to the powder (Equation 3.11 in Phase 1), in this case, the heat is transferred to the melt.

Melting Calculations

With thicknesses of $\delta_{pl,s}$ and $\delta_{pl,f}$ at the start and finish of the designated time step, the time-averaged melt thickness (δ_{pl}) is the mean of these two quantities as shown in Figure 3.10. The thickness of each segment in the melt layer (δ_{seg}) (a total of five segments) is equal to $\delta_{pl}/5$. The area of the inner surface of the melt (node 8 in Figure 3.9), is given by:

$$A_{pl,innersurface} = 2 \cdot \left[\left(l_i - 2\delta_{pl} \right) \cdot \left(h_i - 2\delta_{pl} \right) + \left(h_i - 2\delta_{pl} \right) \cdot \left(w_i - 2\delta_{pl} \right) + \left(w_i - 2\delta_{pl} \right) \cdot \left(l_i - 2\delta_{pl} \right) \right] \quad (3.14)$$

Hence, the average melt surface area is:

$$A_{avg} = \left(A_{i,mold} + A_{pl,innersurface} \right) / 2 \quad (3.15)$$

where $A_{i,mold}$ is the area of the inner surface of the mold, as calculated in Table A.1. It is also assumed that each of the melt nodes (nodes 4 to 8) has the same surface area, which is denoted by A_{avg}. Masses of each melt segment are calculated based on their thickness. A representative calculation for node 4 is shown below.

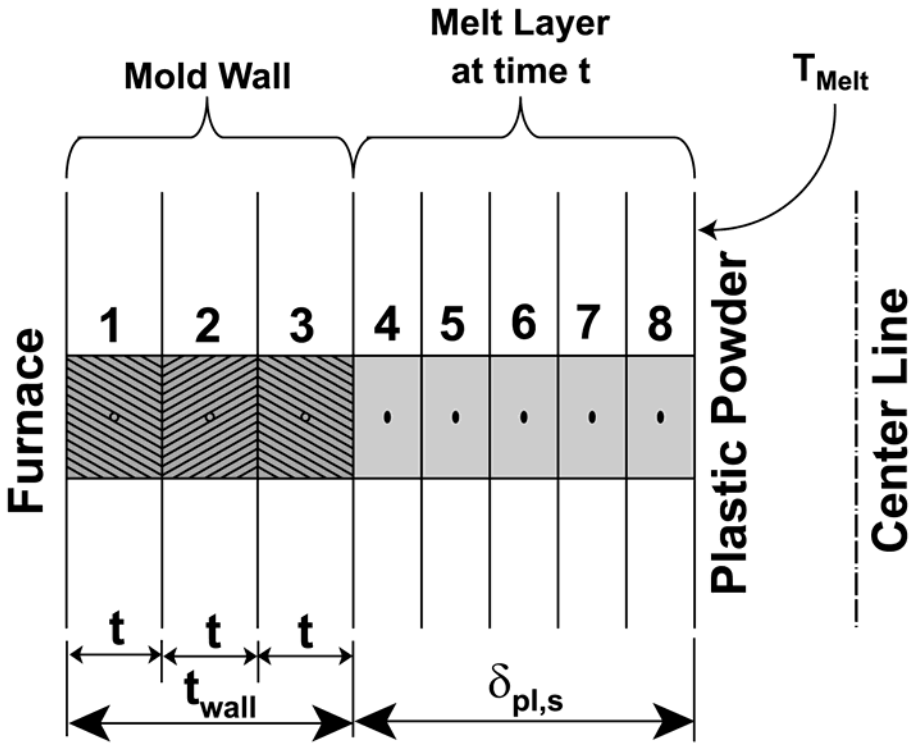

Figure 3.9: Segmental Divisions of Mold Wall and Plastic Melt during Phase 2 of Stage 1

The volume of the internal cavity (of dimensions l_i, w_i and h_i) is given by vol_i. (This is estimated in Table A.1). With δ_{seg} as the thickness of node 4, the volume inwards from node 4 is calculated as:

$$\mathrm{vol}_{i,4} = \left[\left(l_i - 2\delta_{seg}\right)\cdot\left(w_i - 2\delta_{seg}\right)\cdot\left(h_i - 2\delta_{seg}\right)\right] \tag{3.16}$$

Accordingly, the net volume of node 4 is the difference between these two individual volumes. Thus, with the density of node 4 (which is calculated at the time-averaged temperature T_4), the mass of node 4 is given by:

$$\mathrm{mass}_4 = \left(\mathrm{vol}_i - \mathrm{vol}_{i,4}\right)\cdot \rho_{pl,4} \tag{3.17}$$

The thermal energy conducted through the mold/melt interface, i.e., from the inner node (node 3) of mold to node 4 (melt-node), is given by:

$$Q_3 = \left[\frac{T_3 - T_4}{(t/2)/\left(k_{mold}A_{mold}\right) + \left(\delta_{seg}/2\right)/\left(k_{pl,4}A_{avg}\right)}\right] \tag{3.18}$$

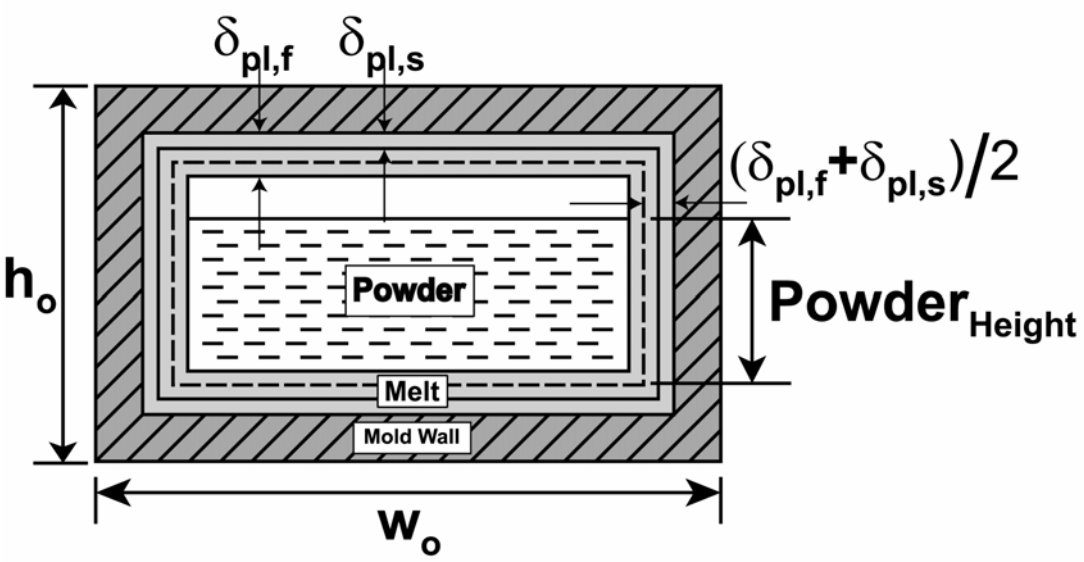

Figure 3.10: Cross-Sectional View of Mold during Phase 2 of Stage 1

The above equation accounts for the different thicknesses and conductivities of the two different half nodes belonging to the mold and the melt. With masses of each of the melt segments calculated as shown earlier, the thermal energies stored in nodes 4 to 8 are given by:

$$Q_{St,j} = mass_j \cdot C_{p,pl,j} \cdot \left(\frac{T_{j,f} - T_{j,s}}{\Delta t} \right) \tag{3.19}$$

for j = 4,…, 8. Also, the energy conducted through each melt segment is:

$$Q_j = \left[A_{avg} \cdot \frac{T_j - T_{j+1}}{\left(\delta_{seg} / \left(2 \cdot k_{pl,j}\right)\right) + \left(\delta_{seg} / \left(2 \cdot k_{pl,j+1}\right)\right)} \right] \tag{3.20}$$

for j = 4,…, 7. It should be noted that the thermal conductivities of the different nodes are calculated at their respective time-averaged temperatures. The energy balance for each melt segment is as follows:

$$Q_{j-1} = Q_{St,j} + Q_j \tag{3.21}$$

for j = 4,…, 7. An energy balance on the 8th node yields Q_{front},, the energy transferred to the melting front:

$$Q_7 = Q_{St,8} + Q_{front} \tag{3.22}$$

At the melt/powder interface Q_{front} is used to a) melt the powder, $Q_{phasechange}$, and b) heat the residual powder and air at the core, Q_p. Thus:

$$Q_{front} = Q_{phasechange} + Q_p \tag{3.23}$$

During the melting phase, the temperature at the front is equal the melting point of the powder, T_{Melt}, which yields the following expression for heat transfer to the interface, Q_{front}:

$$Q_{front} = \frac{k_{pl,8} \cdot A_{avg} \cdot \left(T_8 - T_{Melt}\right)}{\left(\delta_{seg} / 2\right)} \tag{3.24}$$

Here, $\delta_{seg}/2$ appears in the denominator because the heat flow in the melt phase at this edge node is only through half the node thickness. The portion of this incoming heat flow required for the phase-change process is given by:

$$Q_{phasechange} = \left[h_{fusion} + C_{p,p} \cdot \left(T_{Melt} - T_p\right)\right] \cdot \frac{\Delta mass}{\Delta t} \tag{3.25}$$

where, $\Delta mass/\Delta t$ is the rate of formation of the melt and h_{fusion} is the latent heat of fusion of LLDPE (45.4% crystallinity). This accounts for phase-change as well as the energy required to raise the powder temperature from T_p to the melting point. With the

instantaneous melting rate (Δmass/Δt) thus calculated, the remaining powder inventory can be computed, which in turn is used to estimate the height of the powder at the core of the melt, as shown in Figure 3.10. Thus, the mass of the plastic remaining in the powder state ($mass_p$) is:

$$mass_p = \left[m_p - \sum_{j=4}^{8} mass_j \right] \tag{3.26}$$

Here, $mass_j$ represents the mass of each segment averaged from the start to the finish of the time step. The height of the residual powder at an instant when the width is along the horizontal is given by:

$$Powder_{Height} = vol_p / \left[\left(l_i - 2\delta_{pl} \right) \cdot \left(w_i - 2\delta_{pl} \right) \right] \tag{3.27}$$

where, vol_p is the volume of plastic remaining in the powder form. Thus the area of the powder in contact with the melt is given by (Figure 3.10):

$$A_{melt/powder} = 2 \cdot Powder_{Height} \cdot \left(w_i - 2\delta_{pl} \right) + 2 \cdot Powder_{Height} \cdot \left(l_i - 2\delta_{pl} \right) + \left(w_i - 2\delta_{pl} \right) \cdot \left(l_i - 2\delta_{pl} \right) \tag{3.28}$$

Therefore, the heat convected to the residual mass of powder is:

$$Q_p = h_{coeff,p} \cdot A_{melt/powder} \cdot \left(T_{Melt} - T_p \right) \tag{3.29}$$

It should be noted that the heat transfer to the portion of the inner cavity filled by air is neglected in comparison to the heat absorbed by the powder. Finally, this heat flow into the powder heats up the powder as given by:

$$Q_p = mass_p \cdot C_{p,p} \cdot \left(\frac{T_{p,f} - T_{p,s}}{\Delta t} \right) \tag{3.30}$$

The simultaneous solution of these equations yields the temperatures at the end of the time step at each node ($T_{1,f}$ to $T_{8,f}$) as well as that of the remaining powder ($T_{p,f}$). Integral to the calculation is the computation of the mass of the melt formed and its varying thickness. These computations continue until the end of the heating process in the furnace (nominally 17 minutes). The heat transfer process and the growth of the melt front are shown schematically in Figure 3.11.

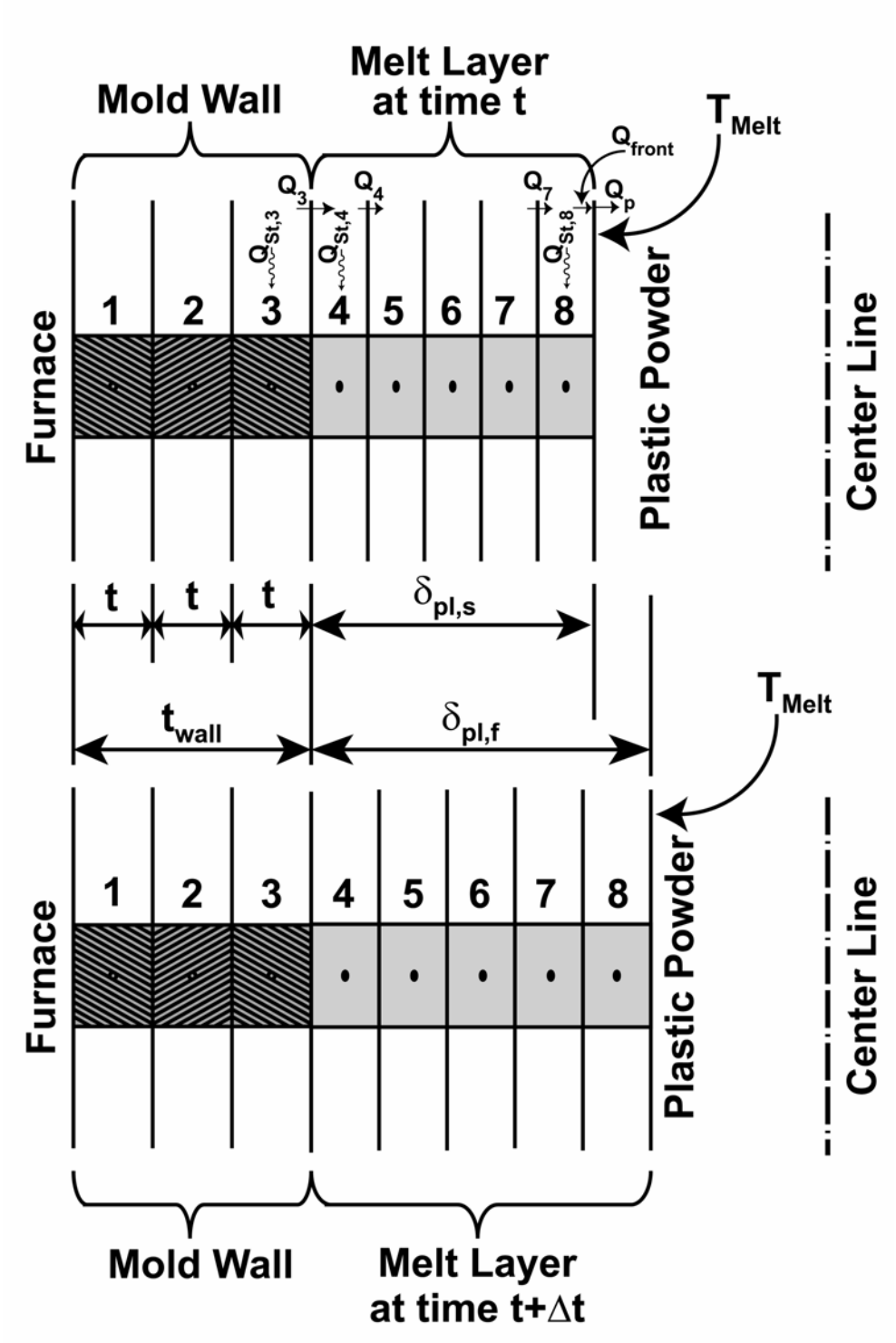

Figure 3.11: Growth of Melt Front during Phase 2 of Stage 1

3.3.2: Stage 2 – Free Convection Cooling in Ambient

At the end of the heating phase, the mold assembly is moved out of the furnace and is cooled by natural convection and radiation in ambient air. Depending on the length of the heating phase, it is possible that the plastic has not melted entirely at the end of the heating stage. However, because the mold is at a higher temperature than the plastic at the end of the heating process, the melt and the powder continue to receive heat from the mold and melting continues for a portion of the natural convection cooling stage.

Based on the simulation results, the pre-cooling process is divided into three phases. Thus, the first phase (Phase 1) of this stage consists of a continued melting phase until all of the powder has been deposited as melt on the inner surface of the mold. (It should be noted that in cases where an insufficient heating duration is chosen, the entire powder inventory may not melt before the cooling begins.) Following this, the melt cools in the liquid phase, until the temperature of the inner wall of the mold decreases to the melting point of the plastic (Phase 2). Beyond this point, the melt in contact with the inner wall begins to solidify, with the solidification front progressing toward the core of the mold (Phase 3).

3.3.2.1: Phase 1 – Phase-Change Melting

The analysis is identical to the phase-change heating process, but for the furnace being replaced by the ambient environment, and the convective and radiative terms being computed based on the ambient temperature rather than the furnace temperature. With the furnace being replaced by the ambient environment, the radiative and convective terms are modified accordingly:

$$Q_{rad} = \varepsilon\sigma \cdot A_{o,mold} \cdot \left(T_{amb}{}^4 - T_1{}^4\right) \tag{3.31}$$

and:

$$Q_{conv} = h_{coeff,o} \cdot A_{o,mold} \cdot \left(T_{amb} - T_1\right) \tag{3.32}$$

where, T_{amb} is the ambient temperature. Heat transfer within the segments is similar to Phase 2 of Stage 1.

The changing directions of the heat flows within the mold are automatically accounted for: a positive heat flow term for denotes heat absorption, while a negative sign denotes heat rejection.

3.3.2.2: Phase 2 – Single Phase Cooling

After the melting phase is complete, the inner cavity of the mold does not contain any powder. The melt forms a concentric layer of thickness δ_{pl} on the inner surface of the mold. The mass of melt sticks to the inner surface of the mold during rotation. This phase lasts until the inner wall of the mold cools down to the melting point of the plastic and the melt it is in contact with starts to solidify. The cross-sectional view of the mold in this phase is shown in Figure 3.12. In absence of plastic in powder form and the melt-front, the governing energy equations associated with these, as in Phase 1 of Stage 2 (Equations 3.23 to 3.30) are not required. Assuming negligible air capacitance, the heat transferred to node 7 is simply the heat released due to cooling of node 8 as follows:

$$Q_7 = Q_{St,8} \tag{3.33}$$

Other equations are identical to those developed for the previous phase. At the end of this phase, the melt in contact with the inner wall of the mold starts solidifying.

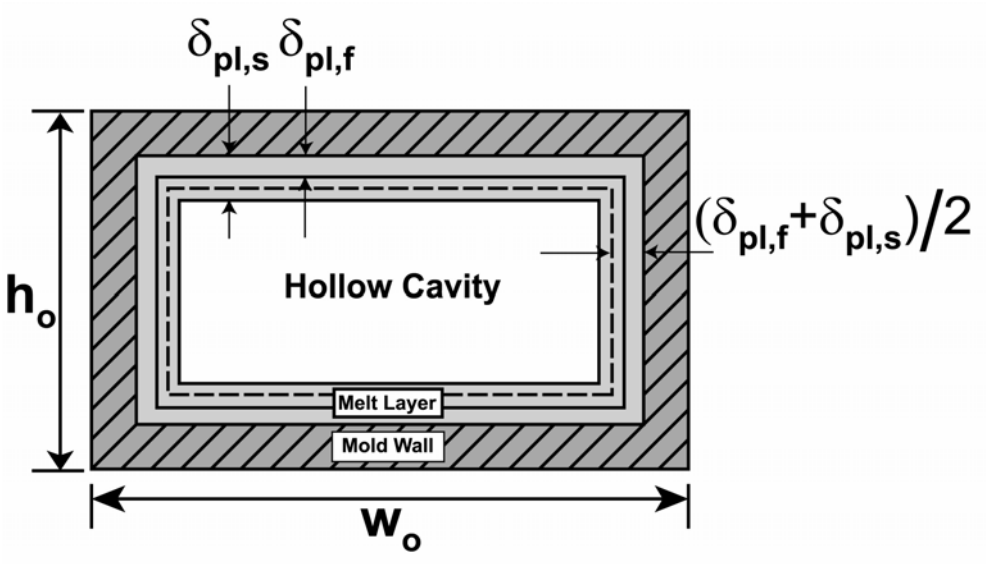

Figure 3.12: Cross-Sectional View of Mold during Phase 2 of Stage 2

3.3.2.3: Phase 3 – Solidification

This phase models the solidification of the plastic melt. It continues until the end of the pre-cooling process (free convection cooling). The total duration of the three individual phases in Stage 2 is equal to the duration of the pre-cooling process (nominally 23 minutes).

Solidification begins at the inner wall of the mold and gradually propagates inwards as cooling progresses (Figure 3.13). The solidified plastic and the melt are divided into five segments each. Hence, five new nodes (of the solidified melt) are introduced to the simulation process, in between the mold wall and the plastic melt, and the melt nodes shift from 4-8 (in Figure 3.11) to 9-13 (in Figure 3.13). The cross-sectional view of the mold is shown in Figure 3.14.

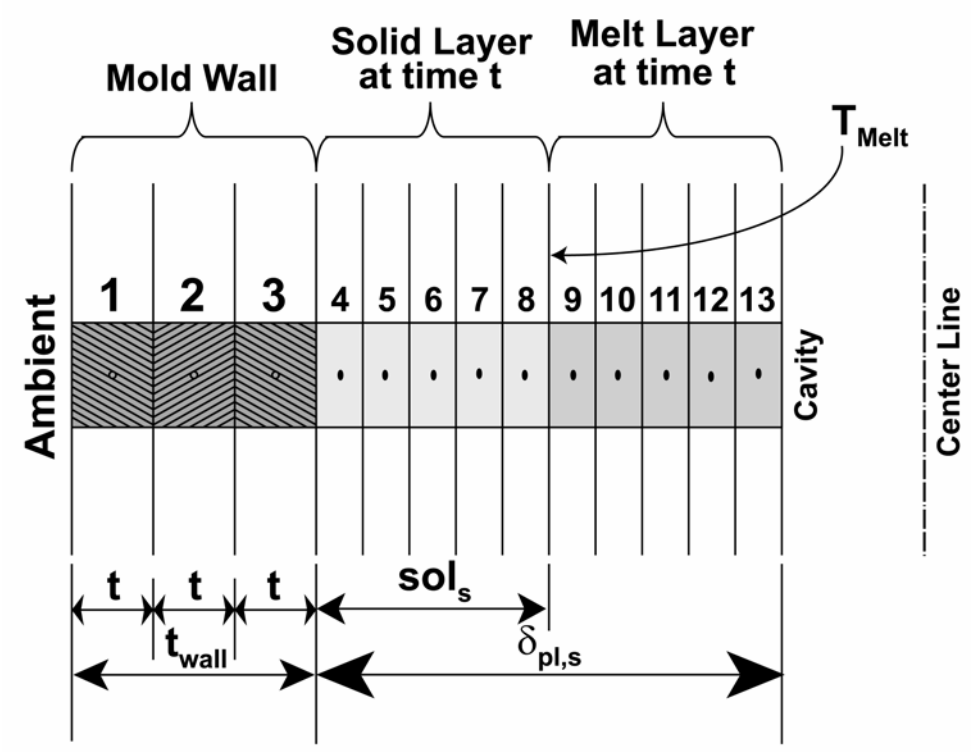

Figure 3.13: Segmental Divisions for Phase 3 of Stage 2

As before, the sign of the thermal energy determines the direction of the energy flow. Within these solid and liquid phases, the conduction and heat storage terms are computed as before. Also, computations similar to those described before for melting are

conducted at the solid-liquid interface (at the fusion temperature) for the solidification process. Thus, these calculations simultaneously account for (a) cooling of the melt, (b) solidification, and (c) cooling of the solidified segments. This process is carried out for the entire natural convection cooling period (nominally 23 minutes), with the computations at each time step yielding the temperatures for each of the 13 nodes in the system, along with the variation of the solid and liquid fractions. Thus, the energy equations for nodes 1, 2, and 3 (mold) are identical to the previous case. The solidification process is explained below.

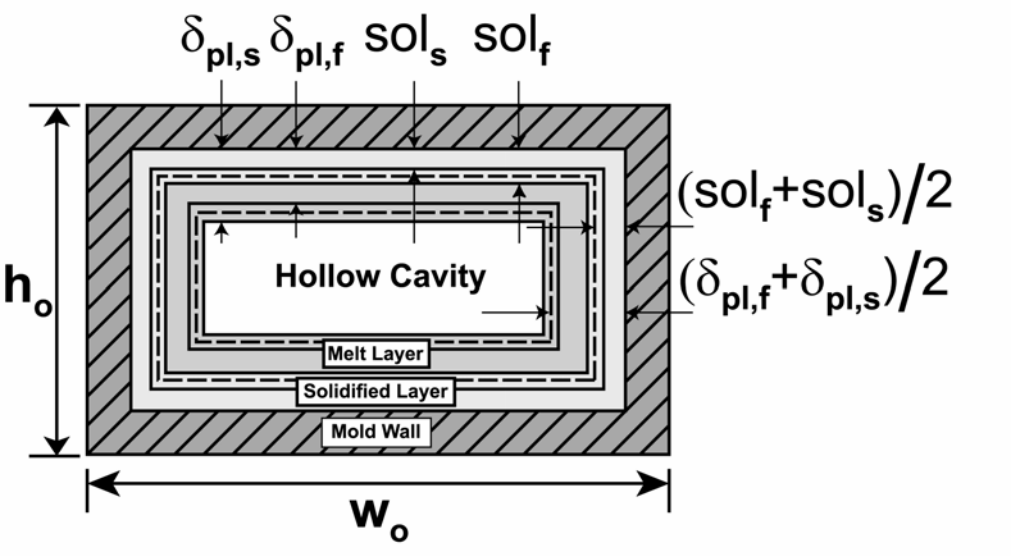

Figure 3.14: Cross-Sectional View of Mold during Phase 3 of Stage 2

Solidification Calculations

At the mold inner wall/solidification interface, the heat conducted from node 3 (node in mold) to node 4 (node in solidified-melt) is given by:

$$Q_3 = \left[\frac{T_3 - T_4}{(t/2)/(k_{mold}A_{mold}) + (sol_{seg}/2)/(k_{pl,4}A_{avg,sol})} \right] \tag{3.34}$$

where the segmental thickness of the solidified-melt (sol_{seg}) and the average cross-section for heat transfer across the solidified layer ($A_{avg,sol}$), are calculated as follows. With sol_s and sol_f as the start and finish solidified thicknesses during a time step, the time-averaged

solidified thickness is calculated as $\delta_{sol} = (sol_f+sol_s)/2$ and the thickness of each solidified-melt segment (sol_{seg}) is $sol_{seg} = \delta_{sol}/5$. Subsequently, the area of the inner surface of the solidified-melt (node 8 in Figure 3.13) is calculated based on the time-averaged solidified thickness (δ_{sol}).

$$A_{sol,\,innersurface} = 2\cdot\left[\left(l_i - 2\cdot\delta_{sol}\right)\cdot\left(h_i - 2\cdot\delta_{sol}\right) + \left(h_i - 2\cdot\delta_{sol}\right)\cdot\left(w_i - 2\cdot\delta_{sol}\right) + \left(w_i - 2\cdot\delta_{sol}\right)\cdot\left(l_i - 2\cdot\delta_{sol}\right)\right] \tag{3.35}$$

It is assumed that each of the solidified nodes has the same area ($A_{avg,sol}$), calculated from the inner surface of the mold, and that of the solidified melt. This area is the cross-section across which the thermal energy is conducted through the solidified melt layer.

Thus, the energy balance for the solidified melt (j = 4 to 7) and melt (j = 9 to 12) segments yields:

$$Q_{j-1} = Q_{St,j} + Q_j \tag{3.36}$$

where the energy conducted through the solidified melt (j = 4 to 7) and melt (j = 9 to 12) segments are as follows:

$$Q_j = \left[A_{avg,sol}\cdot\frac{T_j - T_{j+1}}{\left(sol_{seg}/\left(2\cdot k_{pl,j}\right)\right) + \left(sol_{seg}/\left(2\cdot k_{pl,j+1}\right)\right)}\right] \tag{3.37}$$

and

$$Q_j = \left[A_{avg}\cdot\frac{T_j - T_{j+1}}{\left(\delta_{seg}/\left(2\cdot k_{pl,j}\right)\right) + \left(\delta_{seg}/\left(2\cdot k_{pl,j+1}\right)\right)}\right] \tag{3.38}$$

respectively, where A_{avg} is the average melt surface area, calculated from the inner surface of the melt, and that of the solidified melt. At the solidifying front, an energy balance yields Q_{front}, the residual heat entering the front interface. Here, as stated above, it is assumed that the heat flow is from the solid to the liquid phase. A negative value of this term indicates heat flow in the opposite direction. Thus:

$$Q_7 = Q_{St,8} + Q_{front} \tag{3.39}$$

The heat transfer from node 8 (solidified-melt) to the solid/melt interface, Q_{front} can also be written as:

$$Q_{front} = \left[\frac{T_8 - T_{Melt}}{(sol_{seg}/2)/(k_{pl,8} A_{avg,sol})} \right] \tag{3.40}$$

The temperature at the solidification/melt interface is the fusion temperature of the plastic (T_{Melt}) for solidification to proceed continuously ($sol_{seg}/2$ appears in the denominator of Equation 3.40 because the heat flow in the solidifying phase at this edge node is only through half the node thickness). The total mass of the solidified melt is equal to the average of the start and final values (within a time-step). This yields $mass_{sol,f}$ from the calculated masses $mass_4$ to $mass_8$ and $mass_{sol,s}$ available from the previous step as:

$$\sum_{j=4}^{8} mass_j = \left(\frac{mass_{sol,s} + mass_{sol,f}}{2} \right) \tag{3.41}$$

Melt Calculations

At the solidification/melt interface, the thermal energy (Q_{front}), is used to a) solidify ($Q_{phasechange}$), and b) cool the residual melt (Q_8). Mathematically:

$$Q_{front} = Q_{phasechange} + Q_8 \tag{3.42}$$

The thermal energy rejected in the phase-change solidification process is as follows:

$$Q_{phasechange} = -h_{fusion} \cdot \left(\frac{mass_{sol,f} - mass_{sol,s}}{\Delta t} \right) \tag{3.43}$$

Here, it is assumed that the heat of fusion during solidification is the same as the heat of fusion during melting. Heat transfer from the solidification front to the first melt node (node 9), is as follows:

$$Q_8 = \left[\frac{T_{Melt} - T_9}{(\delta_{seg}/2)/(k_{pl,9} A_{avg})} \right] \tag{3.44}$$

Thicknesses and surface areas of each melt segment are calculated as described in the previous sections. Finally, the energy balance for the 13th node yields:

$$Q_{12} = Q_{St,13} \tag{3.45}$$

This is because, in this phase, there is no heat transfer inward from the melt surface. (There is no plastic powder left and the thermal capacity of any air in the cavity is ignored.)

From the conservation of mass of the plastic, the summation of masses of all the thirteen nodes is equal to the total mass of the powder originally filled into the mold (m_p). Thus,

$$\sum_{j=4}^{13} mass_j = m_p \tag{3.46}$$

The simultaneous solution of these equations yields the temperatures at the end of the time-step at each node, $T_{1,f}$ to $T_{13,f}$, the mass of solidified melt formed, and its thickness. The total duration of the three individual phases in this stage is equal to 23 minutes.

These heat transfer processes and the variation in the solid and melt layers are illustrated in Figure 3.15.

3.3.3: Stage 3 – Forced-Convection Cooling in Ambient

The last stage in the process is forced-convective cooling in ambient air (nominally 23 minutes). The only difference between this stage and the natural convection phase preceding it is the heat transfer mechanism outside the mold. Thus, in this case, the Churchill and Chu (1975) natural convection correlation is replaced by the Hilpert (1933) correlation for crossflow over a cylinder:

$$Nu_L = C\,Re_L^m \cdot Pr^{1/3} \tag{3.47}$$

the characteristic length (L), being same as before. Hence, the convective coefficient ($h_{coeff,o}$) is as follows:

$$h_{coeff,o} = \frac{Nu_L k_{air}}{L} \tag{3.48}$$

To compute this heat transfer coefficient, the convective air flow over the molds was assumed to occur at a velocity of 5 m/sec. The value of the heat transfer coefficient ranges from 21.65 to 22.28 W/m^2-K during this stage.

With the governing energy equations remaining unchanged, the mathematical analysis of this stage is identical to the previous phase (Phase 3 of Stage 2). The inputs for this stage are obtained from the results at the end of the previous stage. From the simulation results, it is inferred that this stage consists of a single solidification phase.

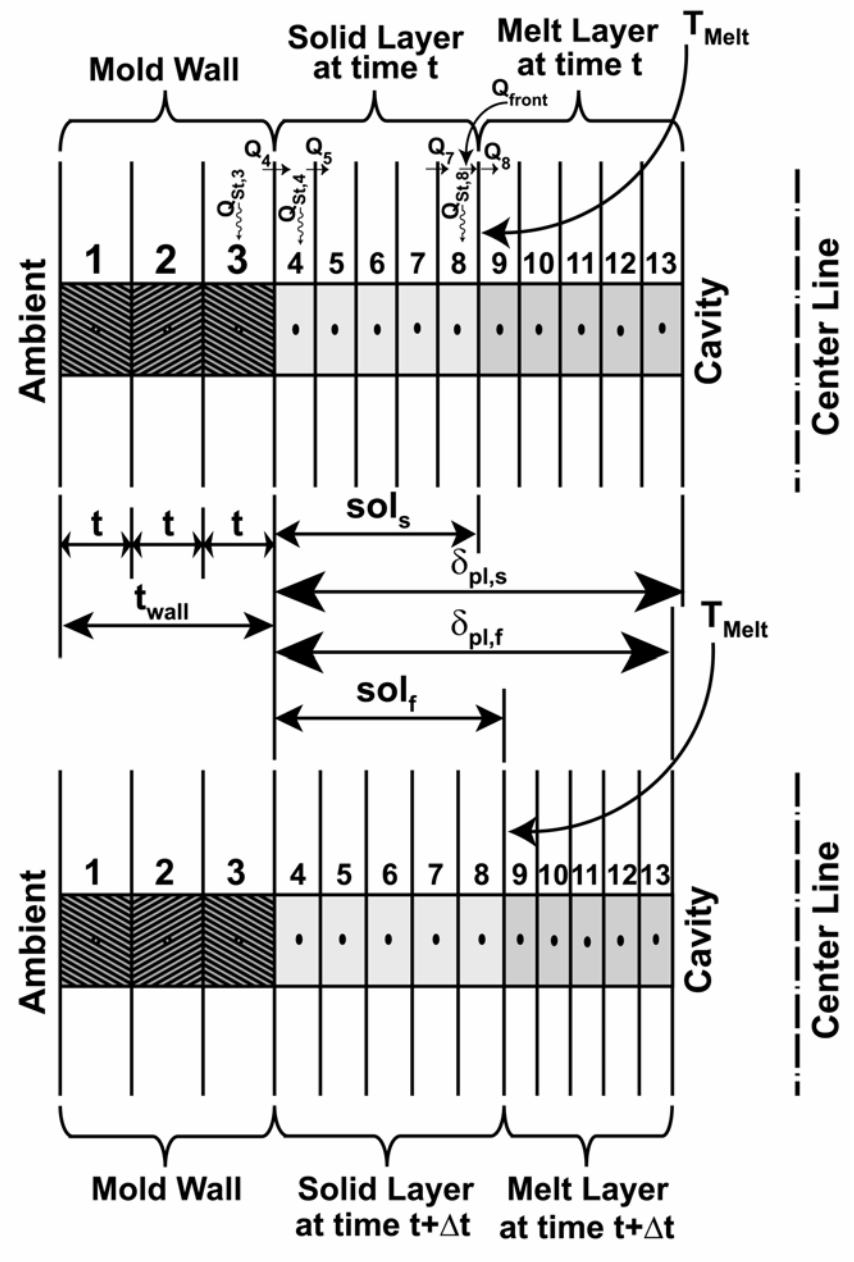

Figure 3.15: Variation in Solid and Melt Layers during Phase 3 of Stage 2

3.4: Results and Discussion

The computations described above were conducted using the Engineering Equation Solver Software (EES) platform (Klein 2003). An overview of the durations of the respective stages of the molding process predicted by the calculations described above is shown in Table 3.3 and Figure 3.16.

3.4.1: Temperatures and Heat Transfer Coefficients

Temperatures at the end of each phase predicted by the simulations are tabulated in Tables 3.4 to 3.9. A summary of the heat transfer calculations for each of these phases, including the corresponding values at the end of a representative run in EES, are shown in Appendix A (Tables A.2 to A.7).

Table 3.3: Predicted Duration of Individual Phases of the Rotational molding Process

Stage No	Description of phase	Duration
Stage 1	Phase 1 (Single-phase transient heating)	4 minutes 50 seconds
	Phase 2 (Phase-change melting)	12 minutes 10 seconds
Stage 2	Phase 1 (Phase-change melting)	3 minutes 10 seconds
	Phase 2 (Single-phase melt cooling)	15 minutes 45 seconds
	Phase 3 (Phase-change solidification)	4 minutes 5 seconds
Stage 3	Phase 1 (Phase-change solidification)	23 minutes

Table 3.4: Results at end of Phase 1 of Stage 1 (Transient Heating of Powder in Furnace)

Node Number	Temperature (^{o}C)
Outer node (node 1)	127.84
Middle node (node 2)	127.75
Inner node (node 3)	127.70
Plastic powder	31.83

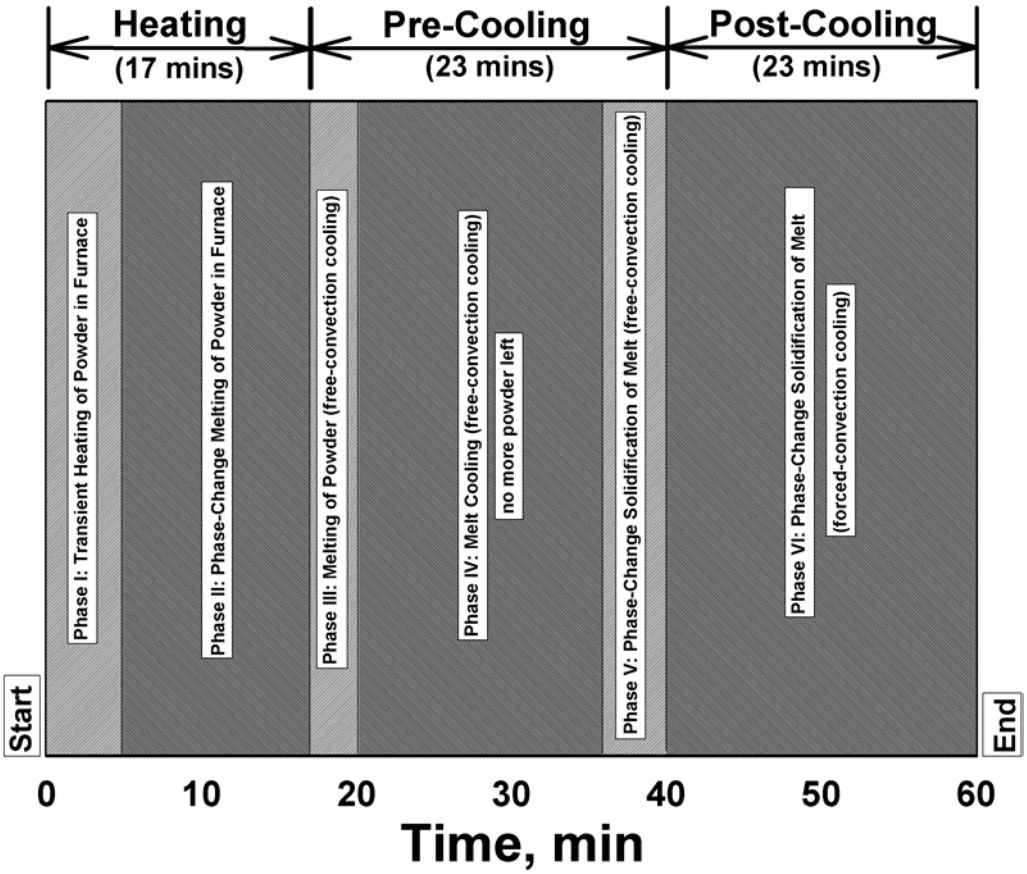

Figure 3.16: Duration of Individual Phases for the Entire Cycle

Table 3.5: Results at end of Phase 2 of Stage 1 (Phase-Change Melting of Powder in Furnace)

Node Number	Temperature (^{o}C)
Outer node (Node 1)	225
Middle node (Node 2)	225
Inner node (Node 3)	225
Node 4	213
Node 5	192
Node 6	173
Node 7	154
Node 8	136
Plastic powder	51
Parameter	**Value**
Thickness of melt layer	8.8 mm
Mass of melt formed	1.13 kg
Mass of powder left	0.23 kg

Table 3.6: Results at end of Phase 1 of Stage 2 (Phase-Change Melting of Powder in Free-Convection Cooling)

Node Number	Temperature (^{o}C)
Outer node (Node 1)	191
Middle node (Node 2)	191
Inner node (Node 3)	191
Node 4	189
Node 5	179
Node 6	166
Node 7	151
Node 8	135
Parameter	**Value**
Thickness of melt layer	10.9 mm
Mass of melt formed	1.36 kg
Mass of powder left	0.0 kg

Table 3.7: Results at end of Phase 2 of Stage 2 (Single-Phase Melt Cooling in Free Convection)

Node Number	Temperature (^{o}C)
Outer node (Node 1)	126
Middle node (Node 2)	126
Inner node (Node 3)	126
Node 4	131
Node 5	137
Node 6	141
Node 7	143
Node 8	145
Parameter	**Value**
Thickness of melt layer	10.8 mm
Mass of melt formed	1.36 kg

Table 3.8: Results at end of Phase 3 of Stage 2 (Solidification of Melt in Free-Convection)

Node Number	**Temperature (^{o}C)**
Outer node (Node 1)	120
Middle node (Node 2)	120
Inner node (Node 3)	120
Node 4	121
Node 5	123
Node 6	124
Node 7	125
Node 8	126
Node 9	129
Node 10	132
Node 11	134
Node 12	135
Node 13	136
Parameter	**Value**
Mass of solidified-melt formed	0.15 kg
Thickness of solidified-melt formed	1.02 mm

Table 3.9: Results at end of Phase 1 of Stage 3 (Solidification of Melt in Forced-Convection)

Node Number	**Temperature (^{o}C)**
Outer node (Node 1)	66
Middle node (Node 2)	66
Inner node (Node 3)	66
Node 4	74
Node 5	88
Node 6	101
Node 7	113
Node 8	123
Node 9	127
Node 10	127
Node 11	127
Node 12	127
Node 13	127
Parameter	**Value**
Mass of solidified-melt formed	1.19 kg
Thickness of solidified-melt formed	8.74 mm
Mass remaining as a liquid	0.17 kg

From Table 3.4, it is evident that at the end of Phase 1 of Stage 1, the inner wall temperature of the mold (node 3) is slightly higher than the melting point of the plastic (T_{Melt}) to signify the commencement of melting. Phase 2 of Stage 1 lasts until the end of the heating mode (Table 3.5). Table 3.6 provides the temperatures obtained at the end of the melting process (Phase 1 of Stage 2), when the entire plastic has melted. At the end of the subsequent phase (Phase 2 of Stage 2), the inner wall temperature of the mold (node 3) drops just below the melting point of the plastic (Table 3.7). Hence, solidification sets in and leads to the development of a solidified plastic layer (nodes 4 to 8 in Figure 3.13) between the inner wall of the mold (node 3) and the melt layer (nodes 9 to 13). At the end of Phase 3 of Stage 2, the solidification process is still in progress with some plastic remaining in the melt form (Table 3.8). The three individual phases in Stage 2 add up to the duration of the pre-cooling (free convection) stage (23 minutes) (Table 3.2). Table 3.9 tabulates the temperatures of each node and the mass of the solidified melt obtained at the end of the post-cooling (forced convection) step, which marks the completion of the rotational molding process. From the simulation, it is inferred that at the end of the process, this mass equals 1.19 kg, and indicates that at the completion of the molding process, the entire melt is not solidified if the duty cycle chosen here is used.

The variation in the convection coefficients ($h_{coeff,o}$), which is coupled with the change in the molding chamber (furnace or ambient) and the outer surface of the mold, is tabulated in Table 3.10.

Table 3.10: Variation in Convective Coefficients for Rotational Molding Process

Stage	Description of phase	$h_{coeff,o}$ (W/m^2-K)	
		Start	**Finish**
1	Phase 1 (Single-phase transient heating)	8.59	7.38
	Phase 2 (Phase-change melting)	7.38	6.03
2	Phase 1 (Phase-change melting)	8.01	7.75
	Phase 2 (Single-phase melt cooling)	7.75	6.99
	Phase 3 (Phase-change solidification)	6.99	6.89
3	Phase 1 (Phase-change solidification)	21.65	22.28

As mentioned before, the heat transfer coefficients for Stages 1 and 2 are predicted by correlations due to Churchill (1975). This coefficient varies with the Rayleigh Number, which is directly proportional to the temperature difference between the mold and the molding chamber (furnace/ambient). During the course of these molding stages, this temperature difference decreases progressively, resulting in a decrease in the heat transfer coefficient. In Stage 3, the heat transfer coefficient is calculated from the correlation due to Hilpert (1933). In this case, the coefficient varies with the Reynolds number. As the temperature difference between the mold and the chamber reduces, the Reynolds number (which varies inversely as the viscosity of the medium) increases, leading to an increase in the heat transfer coefficient.

3.4.2: Discussion

The temperatures of the key nodes predicted by the simulation for the entire rotational molding process are shown in Figure 3.17. This figure shows, as expected, that there is almost no temperature gradient within the mold wall, due to the high thermal conductivity of the mold. During the heating process, the powder/melt located close to the wall tracks the wall temperature closely, and the melt near the wall ("outer melt node" in the figure) becomes superheated due to the incoming heat from the mold as the melting continues.

The powder temperature (within the cavity of the mold) rises more slowly, and exhibits a large temperature difference from the melt due to the higher thermal resistance. The inner melt node temperatures stay close to the melting point during the heating process, signifying the progress of the melting front. This explains the departure of the inner melt temperature (which follows the relatively constant phase change temperature) from the outer melt temperature (which continues to rise due to superheating) at 4 minutes 50 seconds from the onset of the molding process. The maximum temperature attained by the mold throughout the process is 225^{o}C (outer mold wall surface) at a time of 17 minutes. At this instant, when the heating is stopped, the mold temperatures and the temperatures of the melt close to the wall start dropping immediately. However, the interior portion of the melt continues to be heated due to the residual stored heat in the outer nodes flowing toward the interior.

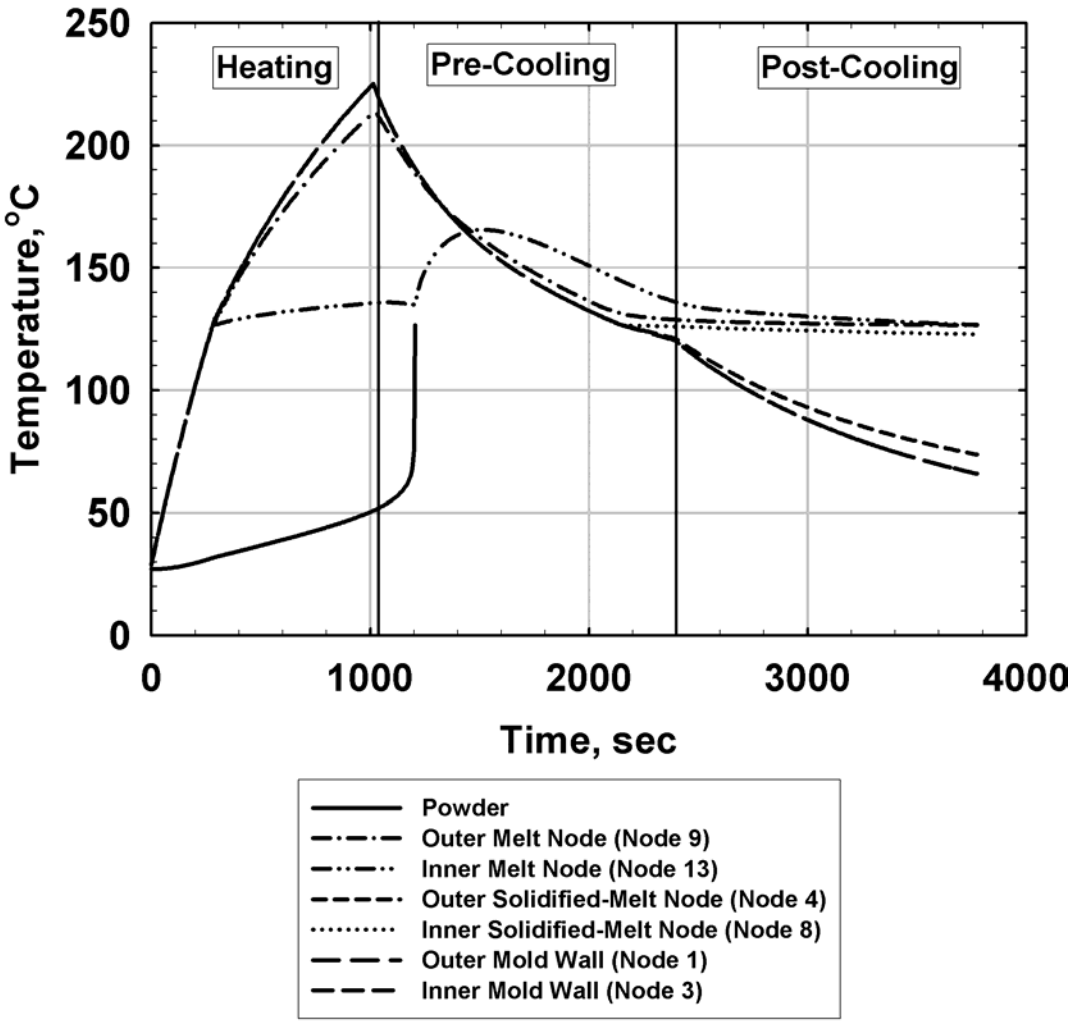

Figure 3.17: Temperature Profiles during the Molding Process

At the instant that the entire inventory of the powder melts (i.e., where the figure shows the end of the powder temperature profile, 20 minutes 10 seconds), the inner melt node temperature rises steeply.

This is because all of the residual heat is now used to raise the temperature of the melt, with essentially no further heat flow required into the interior cavity. This temperature rise continues during the pre-cooling process until a time of 25 minutes 20 seconds, at which point, the mold wall and the outer melt regions have cooled sufficiently, to below the temperature of the interior melt. This initiates the cooling of the innermost melt, as seen in the figure. The peak temperature reached by the inner melt is 165^{o}C. While the melt layers close to the mold wall must necessarily attain temperatures above the melting point for the inner layers to experience phase change, this rise of the inner melt layer temperatures in the peak region above the melting point is unnecessary for successful molding, and offers some opportunities for optimization of the cycle, as discussed in a subsequent chapter. As the cooling progresses beyond this point, the melt temperatures approach the phase-change temperature once again, and stay relatively constant during the subsequent solidification stage. During this latter stage, coinciding with the initiation of forced-convection cooling, the mold wall temperatures show a much steeper decrease due to the higher heat transfer coefficients. The general trends predicted here are in good agreement with those obtained in other studies (Nugent *et al.* 1992; Sun and Crawford 1993; Xu and Crawford 1994; Gogos *et al.* 1998).

The progress of the melting and solidification fronts during the molding process is shown in Figure 3.18, which tracks the distances of the inner melt and the solidified plastic surfaces from the inner wall of the mold. Thus, the melt thickness starts from zero at the instant (t = 4 minutes 50 seconds) the mold wall temperature exceeds the melting point (1) and rises to a thickness of 10.9 mm at the instant during the pre-cooling stage (t = 20 minutes 10 seconds) when the entire plastic has melted. Beyond this point (2), the melt layer shrinks to a thickness of 10.8 mm (3) due to the variation in plastic density with temperature. This figure also shows the steeper change in melt thickness from (3) to (4) during the forced convective cooling stage.

Solidification is initiated at point (3), 35 minutes 55 seconds, and the solid layer thickness continues to rise to point (4) as the cooling proceeds. It should be noted that for a completely solidified melt at the end of the process, the melt and solidified plastic lines must coincide at point (4). However, it can be seen from this figure that with the heating and cooling durations chosen, the entire melt layer is not solidified at the end of the molding process.

The variations in the melt and solidified mass fractions corresponding to the thickness variations shown in Figure 3.18 are presented in Figure 3.19. One interesting insight that can be gained from this figure is the relatively flat region in the melt mass line (1.361 kg) from (2) to (3), a duration of 15 minutes 45 seconds. This is the region where simple sensible heating of the melt occurs, and does not usefully contribute to the molding process. An ideal duty cycle would result in an infinitesimal flat region between (2) and (3). The increase in the solidified mass and the corresponding decrease in the melt mass beyond point (3) is also evident. At the end of the process (4), of the total plastic mass (1.361 kg), 1.19 kg has solidified, while 0.171 kg remains in melt form.

The temperature gradient in the mold and the plastic at several times during the baseline molding process is shown in Figure 3.20. Initially, the mold and the plastic are at ambient temperature. As heating proceeds, the temperature of the mold increases, and a temperature gradient sets in between the mold and the plastic. This is shown at a representative time 0.5 minutes into the heating cycle. As the heating proceeds, melting takes place and the temperature gradient becomes more pronounced. This is shown at 10 minutes from the beginning of the molding process. Due to thermal mass and the resulting lag between the mold and the plastic, the temperature of the plastic rises even during the initial phase of the pre-cooling stage (18.5 minutes from the start of the molding process). During single-phase melt cooling (30 minutes into the molding process), the temperature gradient reverses, and the mold is at a lower temperature than the plastic. With progressive cooling of the mold, the slope of this temperature profile across the cross-section increases (50 minutes into the molding process). Thus, this figure clearly depicts the steep spatial and temporal variations in temperature during the molding process.

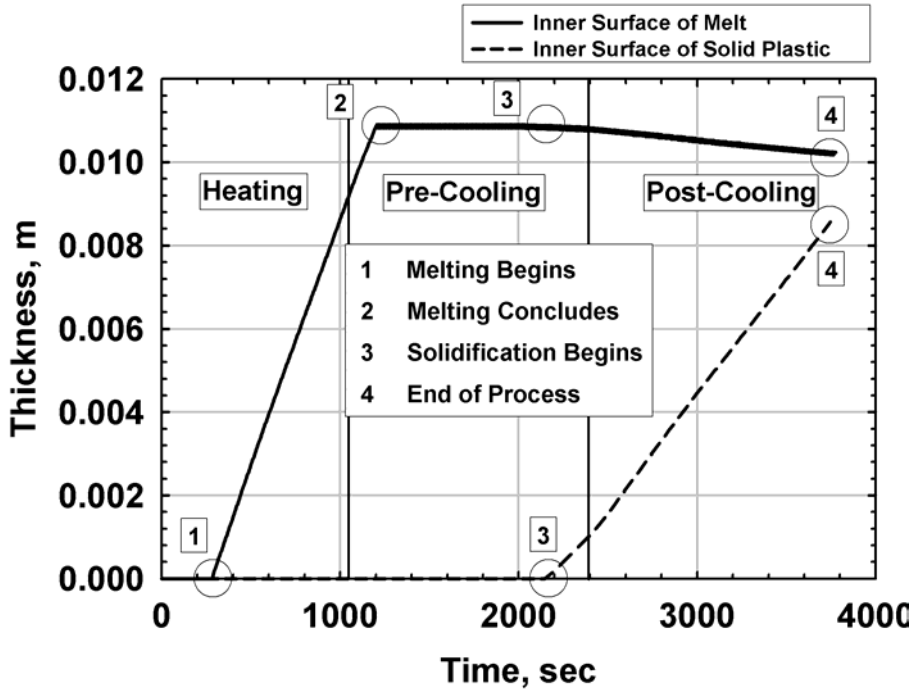

Figure 3.18: Locations of the Melting and Solidification Fronts

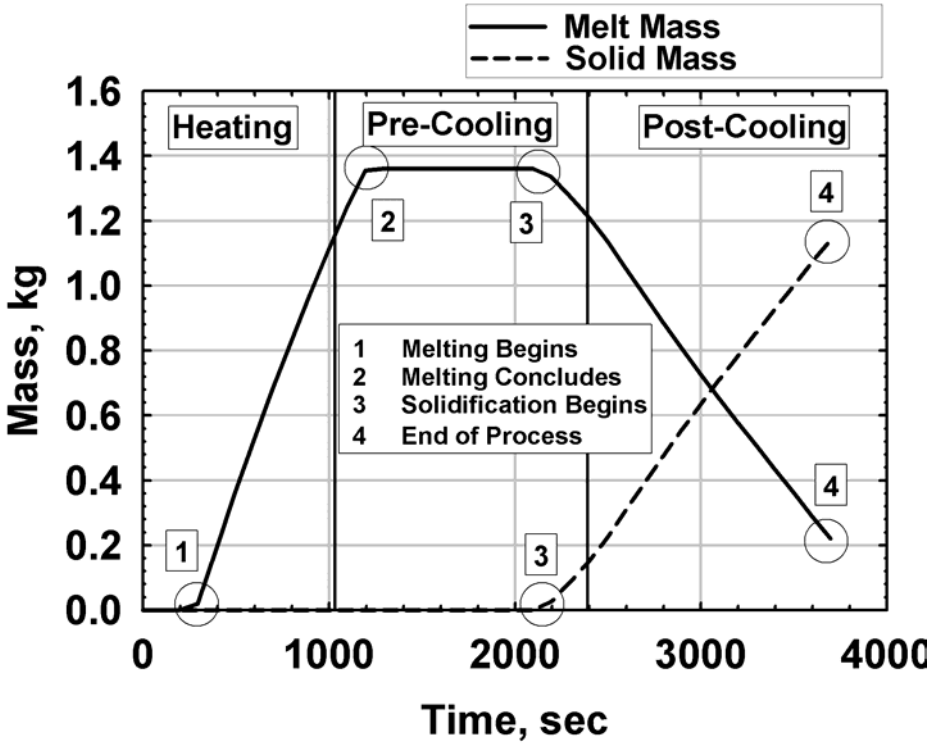

Figure 3.19: Variations of Masses of Molten and Solid Phases

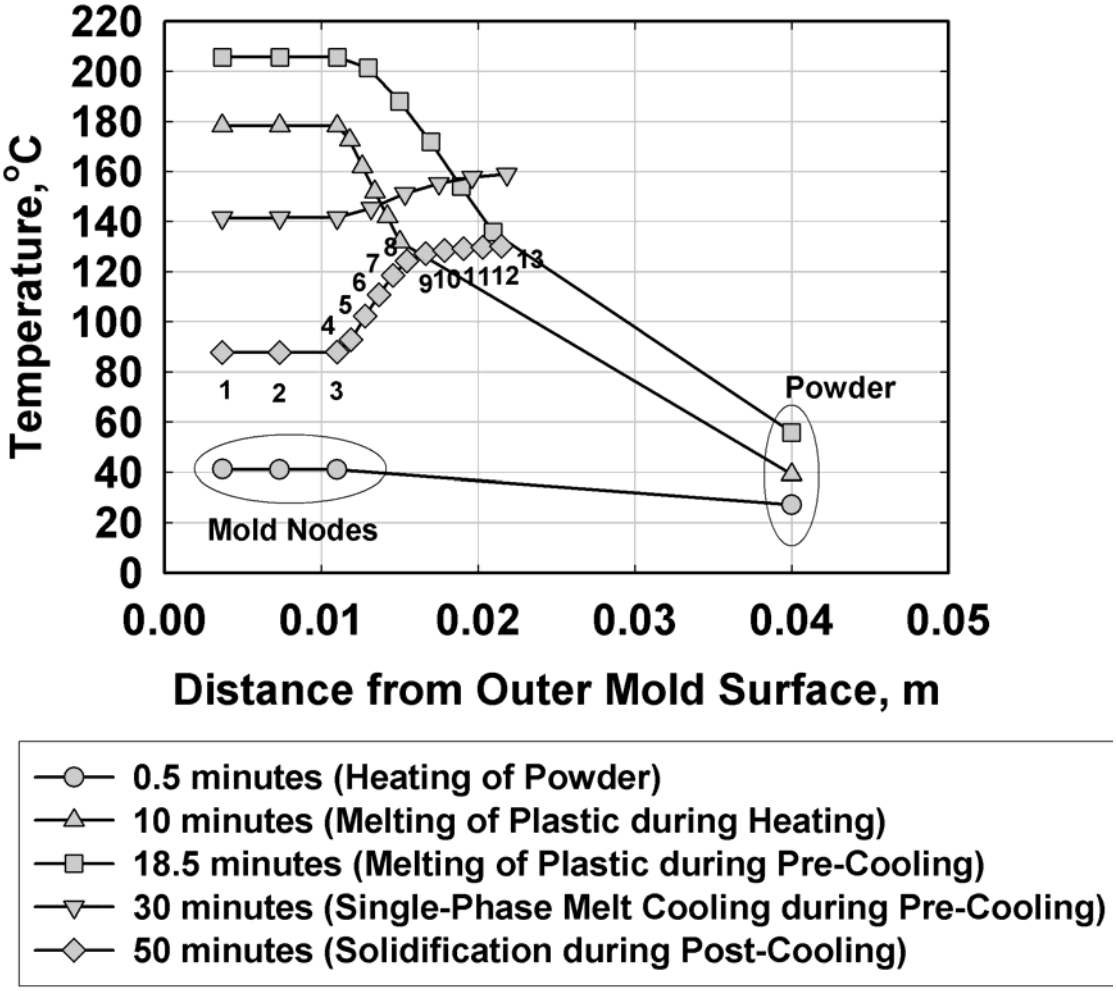

Figure 3.20: Temperature Gradient Across the Mold at Representative Times During Molding

An analysis of the effect of the number of segments in the liquid and solid phases was conducted to determine the accuracy of the model discussed above. The temperature profiles predicted using 5 segments each in the liquid and solid regions, and 7 segments each in these regions are shown in Figure 3.21. The results show that the predictions are almost exactly the same for both cases, which validates the choice of the 5 segments used in this study. The total energy consumption also remains invariant at 1.53 MJ per mold (1.53325 MJ for five segments versus 1.53302 MJ for seven segments, i.e., a difference of 0.015%) for the two cases. For both cases, the mass of plastic which remains in the melt form at the end of baseline molding process is approximately 0.2 kg.

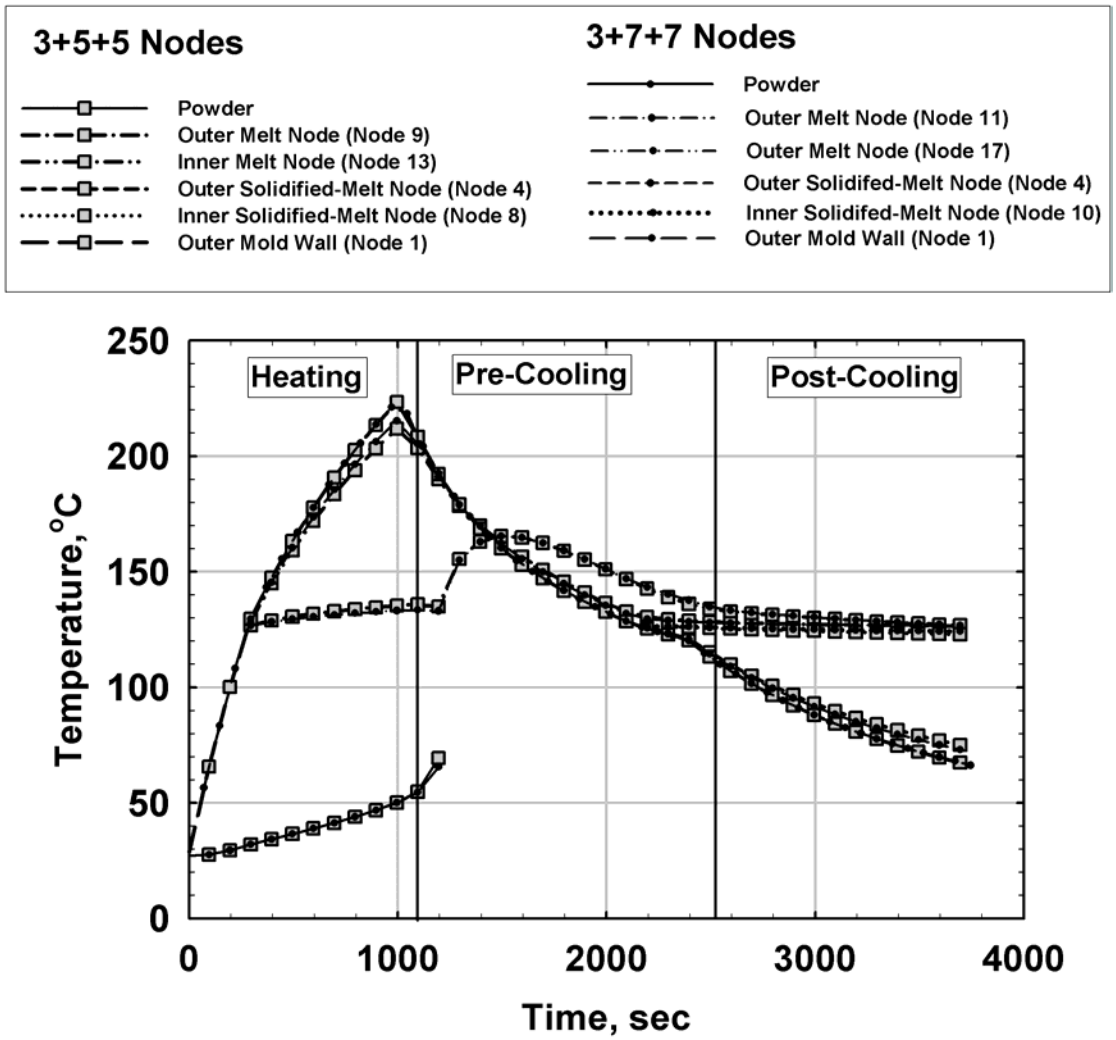

Figure 3.21: Effect of Segment Size on Temperature Predictions

CHAPTER 4

PROCESS OPTIMIZATION

4.1: Effect of Heating Duration

The model described above was used to investigate the effect of modifications in the duty cycle on the transient temperature profiles as well as the total energy consumption in the process. The goal of the investigation was to find the combination of heating and cooling durations that consumes minimum energy, while achieving complete melting and solidification of the plastic powder. Representative modifications to the baseline cycle, and their impact on the molding process are discussed below.

In the first set of variations from the baseline case, the heating duration was varied from 13 to 20 minutes, while maintaining constant pre- and post- cooling durations (at 23 minutes each). These analyses revealed the minimum furnace time required for the plastic powder to melt completely. Thus, heating times less than 14 minutes were found to be unacceptable because they result in incomplete melting of the powder. The corresponding variation in energy consumption is shown in Figure 4.1.

$Energy_{in}$ and $Energy_{out}$ represent the total energy consumed during the heating stage, and the energy released during the cooling stages, respectively. The residual energy (in the mold and the plastic) at the end of the process is $Energy_{net}$. As expected, with an increasing heating duration, the energy input is larger, increasing from 1.25 MJ at 13 minutes to 1.72 MJ at 20 minutes. The energy released during the cooling stages also rises even though the cooling durations stay constant. This is because of the larger temperature differences between the mold and the ambient for the longer heating durations. The net effect, however, is that the residual energy in the mold increases from 0.27 MJ at 14 minutes to 0.35 MJ at 20 minutes. Temporal variations in the heat transfer rates and masses of the plastic with time are shown in Figures 4.2 and 4.3, respectively.

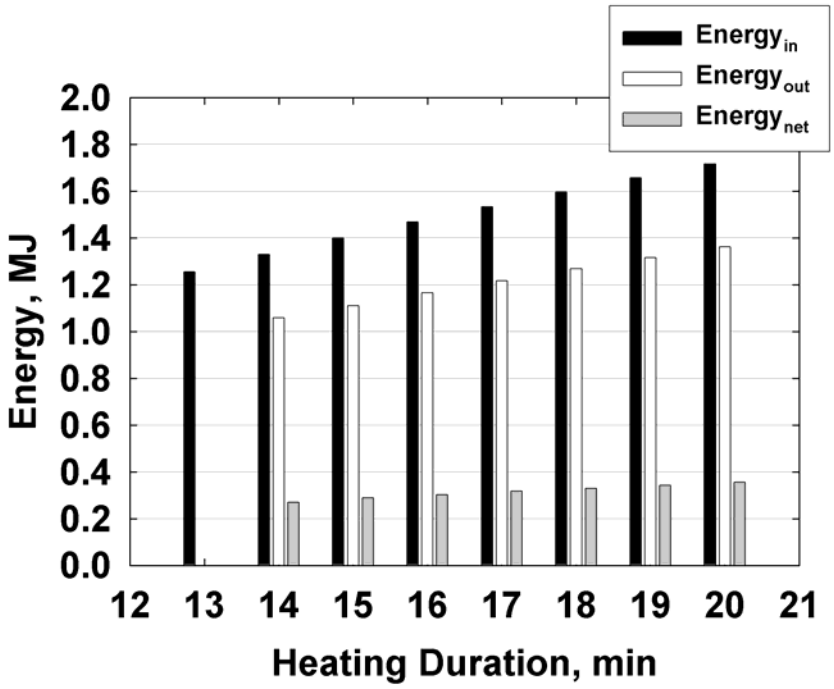

Figure 4.1: Energy Flows as a Function of Heating Duration

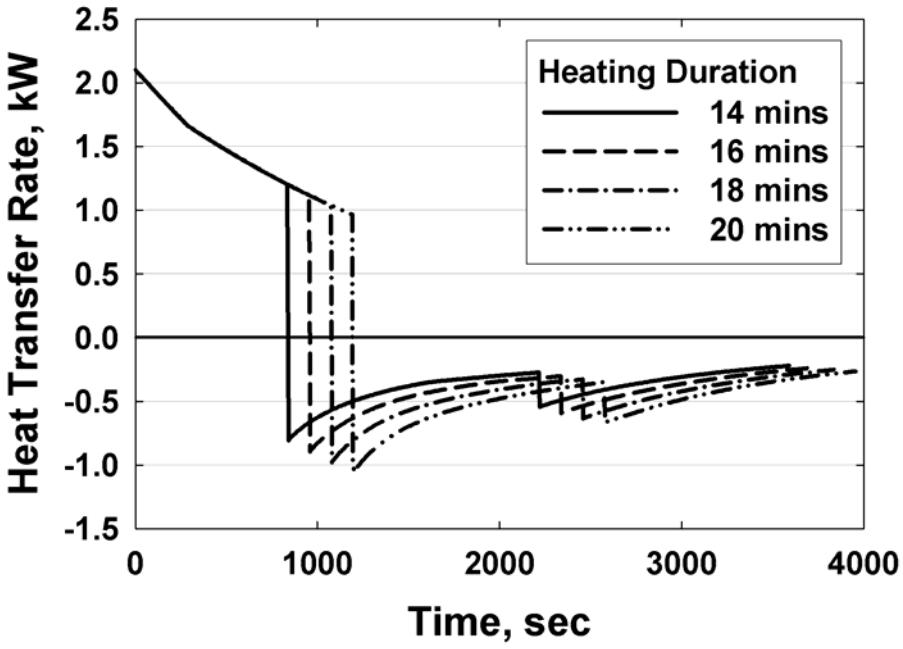

Figure 4.2: Heat Transfer Rates for Various Heating Durations

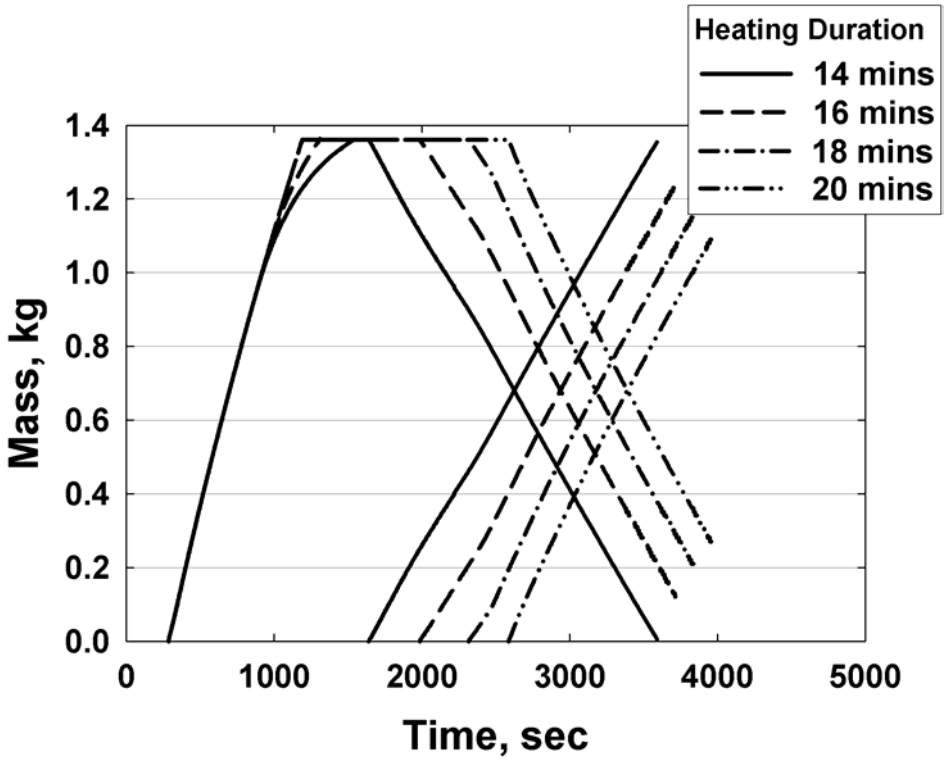

Figure 4.3: Variations in Masses with Different Heating Durations

The heat transfer rate between the surroundings (furnace or ambient) and the mold is directly proportional to the absolute value of the temperature difference between them. Thus, at the beginning of the molding process, this temperature difference is at a maximum, because the surroundings are at the furnace temperature, while the mold is at room temperature. As the heating progresses, this difference decreases, resulting in progressively lower heat transfer rates. Similarly, at the onset of the cooling cycle, the absolute temperature difference is again a maximum, and gradually decreases as the cooling proceeds, resulting in the heat transfer rate asymptotically approaching zero as the mold and the plastic cool toward the ambient temperature as shown in Figure 4.2. The discontinuities in the cooling curve occur when the cooling mechanism changes from natural to forced convection. Figure 4.3 shows that as the heating duration is increased, the time spent in the molten (superheated) phase increases. In addition, the fraction of the plastic remaining in the molten state at the end of the entire process increases from

0.007 kg at 14 minutes to 0.271 kg at 20 minutes. As stated in a previous section, in an optimized process, this "dwell" time, which only contributes to energy consumption, and not to molding, should be minimized.

4.2: Effect of Pre-Cooling Duration (Post-Cooling Fixed at 23 minutes)

Analyses were conducted to determine the optimal cooling times. In this case, the heating duration was kept fixed at 14 minutes, and the pre-cooling duration was varied from 18 to 28 minutes, while keeping the post-cooling (forced-convection) fixed at 23 minutes. The goal here is to determine the duration for which the entire melt is just solidified at the end of the molding process, without any appreciable subcooling, so as to avoid excess time in the pre-cooling chamber. These results are summarized in Figures 4.4-4.6. The analyses show this optimal duration to be 24 minutes: for durations less than this, the plastic melt is not completely solidified, whereas longer durations result in avoidable cooling of an already fully solidified melt as indicated by the flat profiles of the solidified mass curve in Figure 4.6 for the 26 minute case.

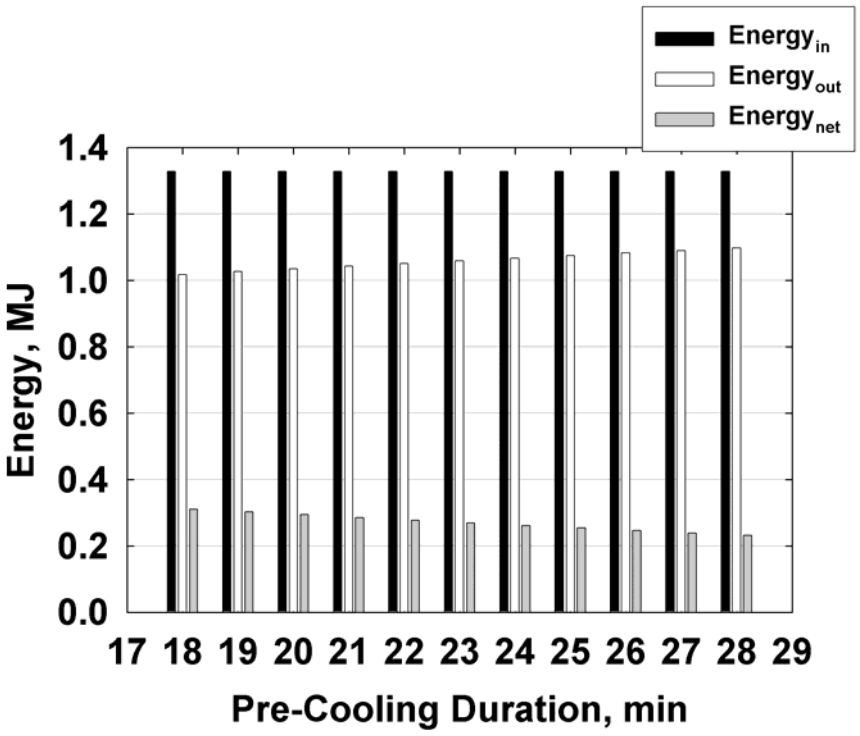

Figure 4.4: Energy Flows as a Function of Pre-Cooling Duration

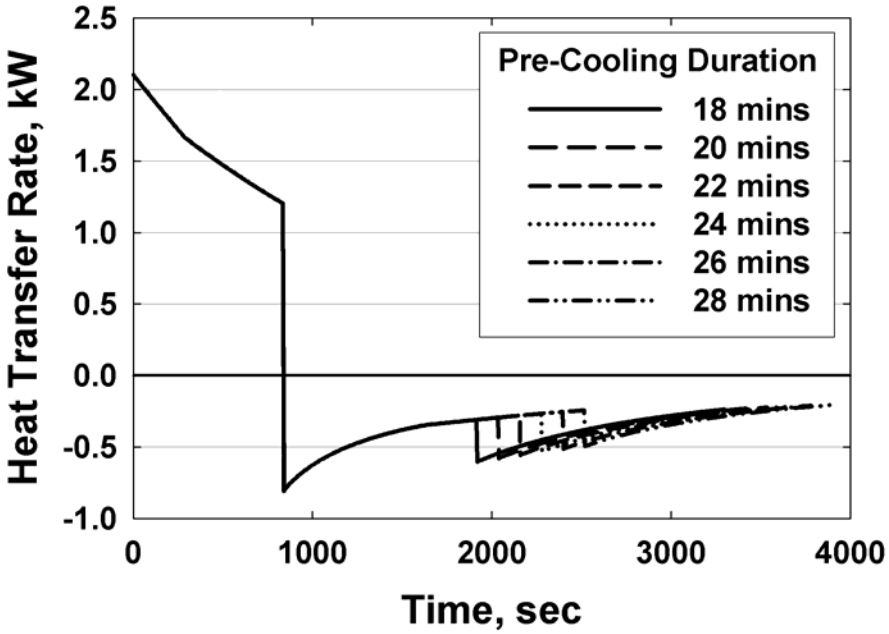

Figure 4.5: Heat Transfer Rates as a Function of Pre-Cooling Duration

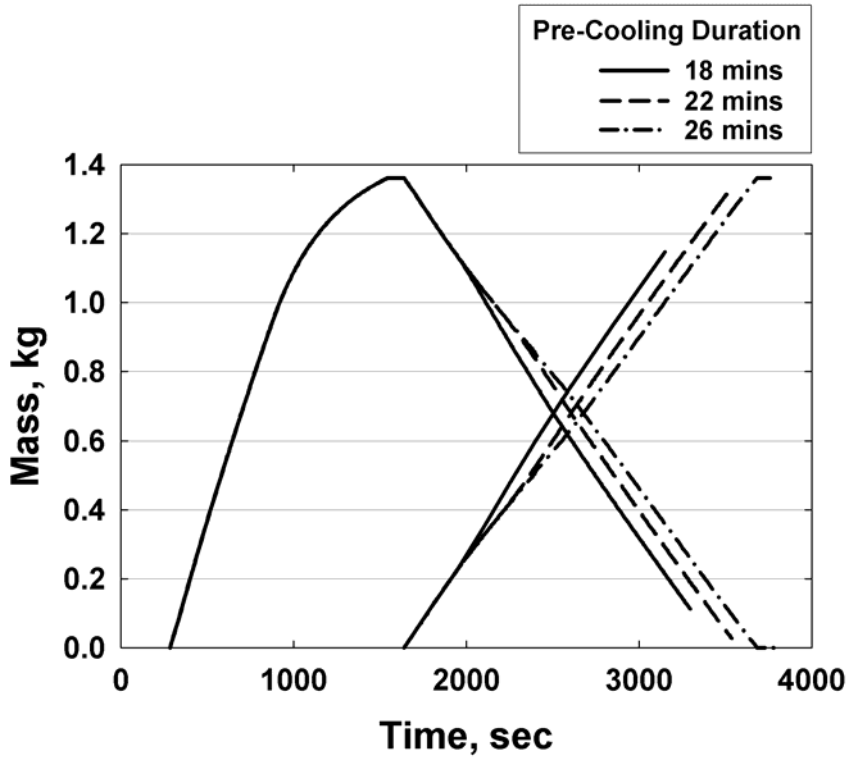

Figure 4.6: Variations in Masses with Different Pre-Cooling Durations

In this case, because the heating duration is unchanged, the energy input remains essentially constant, regardless of the cooling cycle. However, the energy released during the cooling process exhibits a gradual rise with an increase in the pre-cooling duration. The residual energy in the mold and plastic, $Energy_{net}$, shows a corresponding decrease. Thus, the energy released from the mold (Figure 4.4) during the cooling stages increases from 1.02 MJ for a pre-cooling duration of 18 minutes to 1.09 MJ at 28 minutes. The heat transfer rate profiles (Figure 4.5) are invariant during the heating stages as expected, while the lower heat transfer rates characteristic of natural convection persist at longer times as the pre-cooling duration increases. Figure 4.6 shows that the longer the pre-cooling duration is, the longer is the delay in solidification of the plastic melt. This is because the longer pre-cooling period simply delays the initiation of the higher heat transfer rates possible with forced convection in the post-cooling stages. However, in this case, as the pre-cooling duration is increased from 18 to 28 minutes, the overall cooling duration increases from 41 to 51 minutes (because the post-cooling phase duration is kept fixed). This additional cooling time causes solidification of the entire plastic at the end of the process in spite of the lower heat transfer rates characteristic of natural convection being maintained for a longer time. For a pre-cooling duration of 18 minutes, therefore, 0.113 kg of the plastic remains molten at the end of the process, but for a pre-cooling duration of 28 minutes, the entire plastic solidifies by the end of the process.

4.3: Effect of Pre-Cooling and Post-Cooling Durations (Total Cooling Constant at 46 minutes)

Finally, the distribution of the total cooling time of 46 minutes between natural and forced convection was investigated. Thus, the pre-cooling stage duration was increased from 18 to 24 minutes while simultaneously decreasing the post-cooling stage from 28 to 22 minutes. The heating duration was once again maintained at 14 minutes. The energy input and output graphs shown in Figure 4.7 clearly demonstrate that the post-cooling (forced convection) phase is where the major portion of the energy is released from the mold and plastic. Therefore, as the pre-cooling duration increases, which also decreases the post-cooling duration due to the constant total cooling time, the

total energy removed decreases from 1.08 MJ at a pre-cooling duration of 18 minutes to 1.05 MJ at 24 minutes.

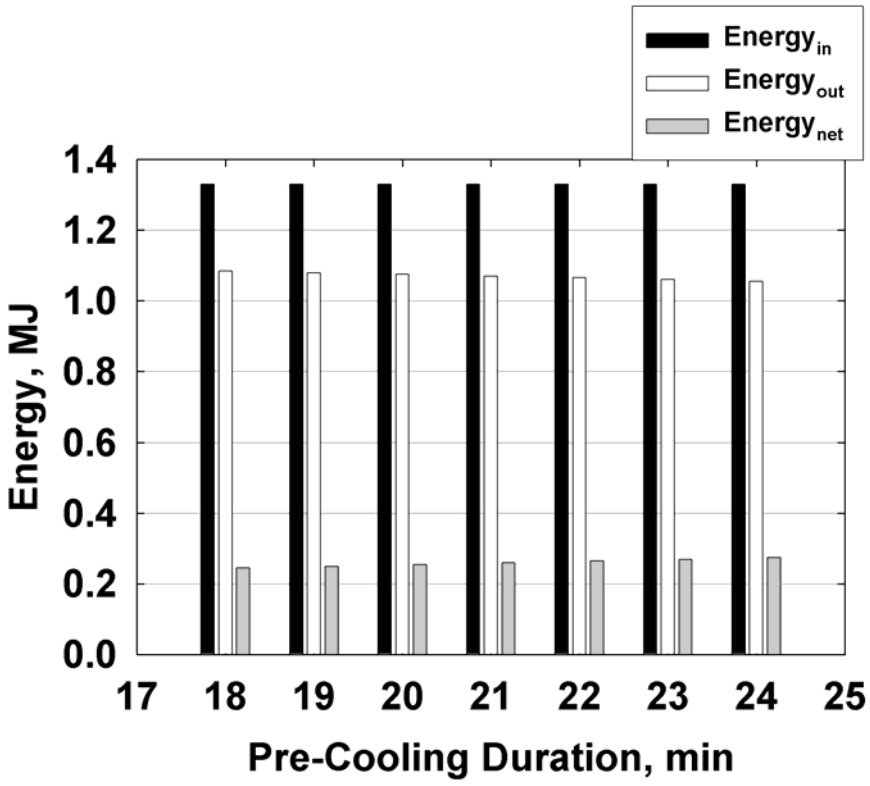

Figure 4.7: Energy Flows as a Function of Pre-Cooling Duration (Fixed Total Cooling Duration)

The corresponding profiles of the heat transfer rates are shown in Figure 4.8, while the melt and solid fractions are shown in Figure 4.9. In this case, the longer pre-cooling phase not only delays the solidification process, but because the post-cooling phase is simultaneously shorter, the fraction solidified at the end of the process decreases from 1.361 kg for a pre-cooling duration of 18 minutes to 1.335 kg at 24 minutes. The most favorable combination of cooling cycles is a pre-cooling duration of 22 minutes and a post-cooling duration of 24 minutes. For this combination, the plastic melt is just completely solidified at the end of the molding process, without any appreciable undercooling. For a pre-cooling time greater than 22 minutes, some of the plastic mass remains in melt form, while for durations less than 22 minutes, there is unnecessary undercooling of the solidified plastic.

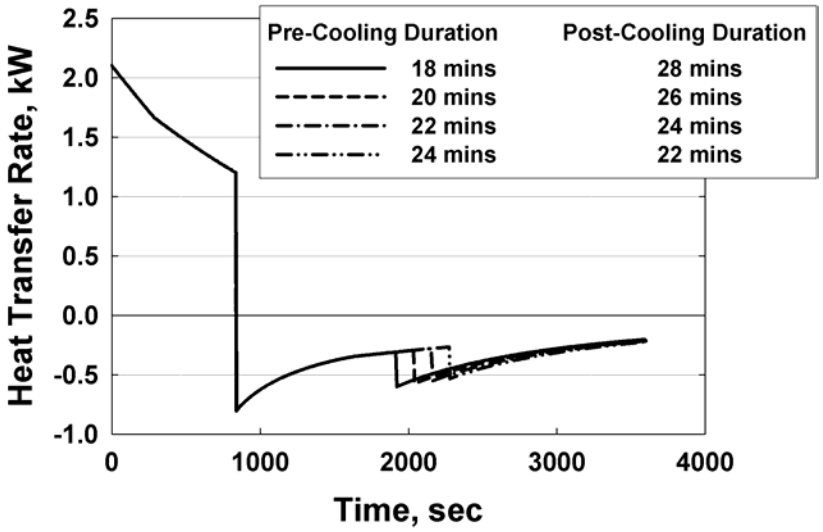

Figure 4.8: Heat Transfer Rates for Different Pre- and Post-Cooling Durations (Fixed Total Cooling Duration)

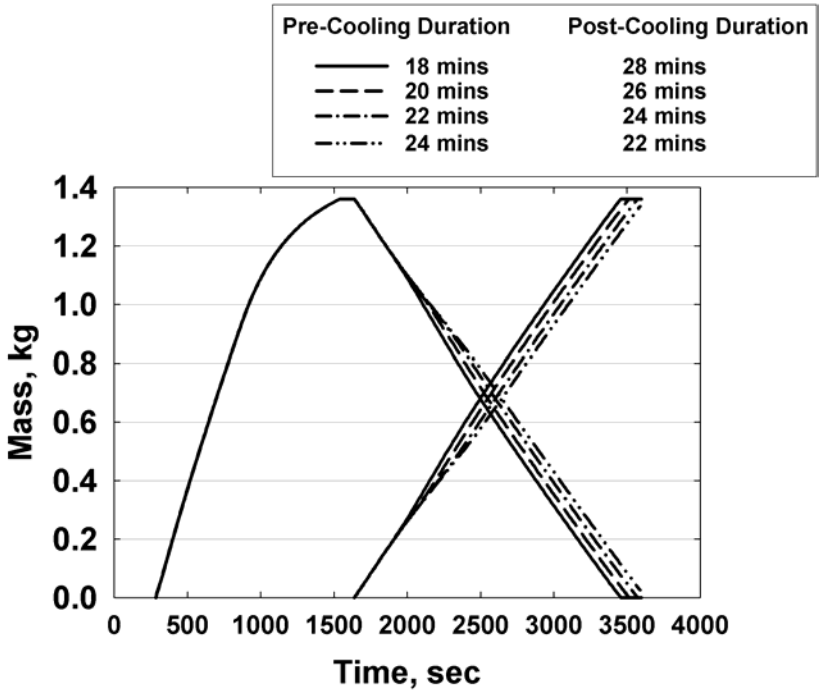

Figure 4.9: Variations in Masses for Different Pre- and Post- Cooling Durations (Fixed Total Cooling Duration)

4.4: Optimal Duty Cycle

From the analyses presented in the previous sections, the optimal heating duration is 14 minutes (Section 4.1). For this duration, the residual energy in a single mold at the end of cooling is equal to 0.261 MJ, when the post-cooling duration is kept constant (Section 4.2). This is lower than the case when the individual cooling schedules are varied (Section 4.3), which is equal to 0.264 MJ. Based on these analyses, the duty cycle can be modified to the optimal values shown in Table 4.1. The optimal heating duration is combined with subsequent cooling durations of 24 (pre-cooling) and 23 (post-cooling) minutes. This combination results in the minimum residual energy in the mold (0.261 MJ) at the end of the molding process. It should be noted that other combinations of pre- and post-cooling times may be deemed optimal, based on the incremental cost for forced-convective cooling over natural convection, as well as the implementation of recuperative waste heat recovery schemes discussed in a subsequent chapter.

The above results demonstrate the potential to achieve the objectives of the rotational molding process and also to decrease overall energy consumption from 1.53 MJ to 1.33 MJ per mold. Given that each molding operation involves batches of multiple molds and also considerable heating and cooling of the auxiliary support structures (discussed in the next chapter), the savings per molding cycle in a commercial plant could be appreciable. Furthermore, the energy released during the cooling stages changes from 1.22 MJ to 1.07 MJ. Depending on the specific flow rates of the cooling medium, this released energy could be used recuperatively in the rest of the plant for pre-heating and other waste-heat recovery applications. This is explored further in subsequent chapters.

Table 4.1: Cycle Times and Other Parameters for Baseline and Optimized Processes

	Baseline	**Optimized**
Heating	17	14
Pre-Cooling	23	24
Post-Cooling	23	23
Energy In	1.53 MJ	1.33 MJ
Energy Out	1.22 MJ	1.07 MJ
All powder Melted?	Yes	Yes
Superheating at Melt Front (T_{front}–126.5^{o}C)	38.9^{o}C	4.3^{o}C
Solidified Fraction at Process Termination	0.874	1

CHAPTER 5

MODELING OF AUXILIARY MASS AND OVERALL ENERGY CONSUMPTION

5.1: Introduction

The auxiliary structure housing the mold accounts for substantial energy consumption during the furnace heating process, which should be taken into consideration when investigating techniques for reducing the energy consumption. The following analysis estimates the energy transfer between the assembly and the surroundings during the heating and cooling stages of the molding process.

As shown in Figure 5.1, the assembly consists of 14 molds arranged symmetrically on the housing structure. To facilitate the estimation of the auxiliary mass, a close approximation to the actual housing (top and bottom structures) is shown in Figure 5.2. Structural details obtained from the manufacturer are tabulated in Table 5.1. Volumes and surface areas of the individual elements of the housing are calculated based on these dimensions. The housing material is made of carbon steel (assumed to be AISI 1010) with the following properties: @ 27^{o}C density = 7832 kg/m^{3}, specific heat capacity = 0.434 kJ/kg-K, conductivity = 63.89 W/m-K (Touloukian and Ho 1972; Incropera and DeWitt 1996).

Figure 5.1: Assembly of Molds in the Actual Manufacturing Process (Top and Bottom Views)

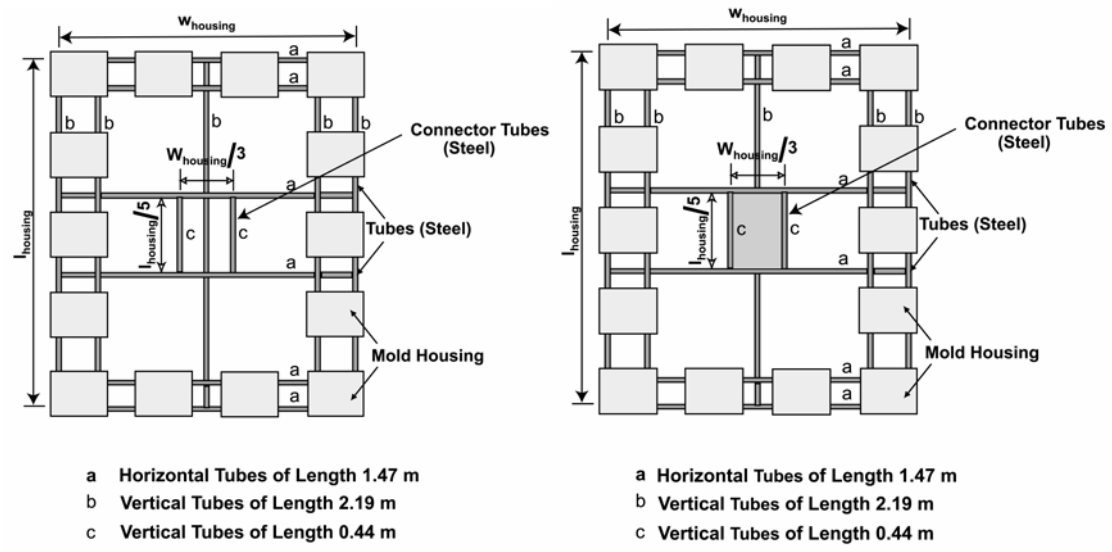

Figure 5.2: Approximated Model of the Housing (Top and Bottom Views)

Table 5.1: Dimensional and Structural Details of the Auxiliary Mass

Dimension	SI units	British Units
Length of housing ($l_{housing}$)	2.197 m	86.5 in
Width of housing ($w_{housing}$)	1.473 m	58.0 in
Height of housing ($h_{housing}$)	0.521 m	20.5 in
Cross section of square tubes forming the housing ($cross_{sec} \times cross_{sec}$)	0.038×0.038 m	1.5×1.5 in
Tube thickness (thk)	0.004 m	0.188 in
Mass of housing ($mass_{housing}$)	417.76 kg	921 lbm
Element	**Number of Units**	
Tubes along the length	10	
Tubes along the width	12	
Connector tubes	4	
Bottom plate	1	
Plates placed at the top and bottom of mold	28	
Various fittings (bolts)	40	

The calculation of volumes and surface areas of the auxiliary housing is shown in detail in Tables A.8 and A.9 respectively, in Appendix A. The resulting quantities are tabulated in Table 5.2.

Table 5.2: Volumes, Surface Areas and Masses of Auxiliary Mass

Element	Quantity	Volume	Surface Area	Mass
Tubes along the length	10	1.4E-02 m^3	3.35 m^2	110 kg
Tubes along the width	12	1.1E-02 m^3	2.69 m^2	88 kg
Connector tubes	4	1.0E-03 m^3	0.27 m^2	9 kg
Bottom plate	1	4E-03 m^3	0.22 m^2 (neglected)	32 kg
Plates placed at the top and bottom of mold	28	1.8E-02 m^3	4.27 m^2	140 kg
Various fittings (bolts)	40	1E-03 m^3	0.13 m^2 (neglected)	5 kg
Sum Total		4.9E-02 m^3	10.58 m^2	384 kg

This estimated mass of the housing (384 kg) is in excellent agreement (within 8%) with the approximate mass provided by the manufacturer (418 kg). The total mass of the 14 molds (excluding plastic) is 80.05 kg. Therefore, the auxiliary mass accounts for nearly 84% of the total thermal mass. Similarly, the total surface area of the auxiliary mass exposed to the molding chamber is 10.6 m^2, whereas for the set of 14 molds, this is 3.05 m^2. Therefore, the auxiliary mass accounts for approximately 78% of the total exposed surface area.

5.2: Thermal Analysis

The heat transfer calculations on the auxiliary mass are described here. Initially the entire system is at ambient temperature (27^{o}C). As before, the furnace is maintained at the constant temperature of 343^{o}C (650^{o}F) throughout the heating process. In addition, the emissivity of the housing surface is assumed to be 0.9, similar to the assumption for the mold surface.

During heating, the energy absorbed by the housing due to radiation and convection is given as:

$$Q_{rad} = \varepsilon\sigma \cdot A_{s,total} \cdot \left(T_{furnace}{}^4 - T_{housing}{}^4\right) \tag{5.1}$$

and

$$Q_{conv} = h_{coeff,housing} \cdot A_{s,total} \cdot \left(T_{furnace} - T_{housing}\right) \tag{5.2}$$

where, $T_{housing}$ is the time-dependent temperature of the housing (assumed to be uniform at any given instant). The natural convective heat transfer coefficient ($h_{coeff,housing}$) on the exposed outer side of the housing (for the heating and pre-cooling process) is calculated using the Churchill and Chu (1975) correlation provided in Chapter 3 (Equation 3.3), where the mean value of the width and depth of the tubes is used as the characteristic length to account for the biaxial rotation. The convective heat transfer coefficient on the surface ranges from 11.54-7.14 W/m^2-K during the heating stage for the *optimized cycle*. During the pre and post-cooling stages, $8.38 \leq h_{conv,natural\ convection} \leq 11.24$ W/m^2-K, and $33.03 \leq h_{conv,forced\ convection} \leq 35.06$ W/m^2-K, respectively. For this cycle, the radiative heat transfer coefficient on the surface ranges from 22.13-41.93 W/m^2-K during heating. During the pre and post-cooling stages, $7.39 \leq h_{rad,natural\ convection} \leq 17.84$ W/m^2-K, and $5.58 \leq h_{rad,forced\ convection} \leq 7.37$ W/m^2-K, respectively. Similarly, the thermal energy stored in the housing during time step Δt is given by the following:

$$Q_{St,housing} = mass_{housing} \cdot C_{p,housing} \cdot \left(\frac{T_{housing,f} - T_{housing,s}}{\Delta t}\right) \tag{5.3}$$

This is equated to the total heat input, which is the sum total of the radiative and convective thermal energies. Thus, the simultaneous solution to these three equations yields the temperature of the steel housing at the end of each time step. Similarly, for each of the cooling stages (free convection followed by forced convection), the basic equations for the heat transfer processes are identical to these equations, except that a negative heat transfer rate denotes thermal energy being rejected from the housing to the surroundings. To model the forced convective cooling process in ambient air, the Churchill and Chu (1975) natural convection correlation is replaced by the Hilpert (1933) correlation for crossflow provided in Chapter 3 (Equation 3.47).

5.3: Gas Consumption Calculations

In this section, the consumption of natural gas required for the furnace used in the rotational molding process is estimated. Natural gas is modeled as methane (CH_4), burned completely with 150% theoretical (50% excess) air. The excess air combustion equation is given by:

$$CH_4 + 3\cdot(O_2 + 3.76N_2) \rightarrow CO_2 + 2H_2O + 11.28N_2 + O_2 \qquad (5.4)$$

It is assumed that at the burner inlet, the natural gas is at room temperature. On a molar basis, the enthalpy of the reactants (methane (CH_4), oxygen (O_2) and (N_2)) is calculated as follows:

$$E_r = \left(E_{CH_4} + 3E_{O_2} + 11.28E_{N_2}\right) \qquad (5.5)$$

This equation yields the reactant enthalpy per kmol of methane (CH_4). In the absence of other detailed information, it was assumed that the products of combustion leave the chamber at the furnace temperature (343.33°C). The product enthalpy is the summation of the individual enthalpies.

$$E_P = E_{CO_2} + 2E_{H_20} + 11.28E_{N_2} + E_{O_2} \qquad (5.6)$$

Thus, the heat released by the fuel is calculated as follows:

$$\Delta_h = \left(\frac{E_r - E_p}{MMASS(CH_4)}\right) \qquad (5.7)$$

Here, the molar mass of methane, MMASS(CH_4) is used to obtain the combustion energy released per unit mass of methane. Assuming a 15% heat loss to the surroundings, the useful heat available from the combustion process is given by the following:

$$Q_{furnace} = 0.85\cdot\dot{m}_{fuel}\cdot\Delta_h\cdot time \qquad (5.8)$$

where time is the duration of the heating process. Equating this combustion energy to the energy requirements of the molds and the auxiliary mass yields an estimate of the fuel flow rate ($\dot{m}_{fuel}$). This mass flow rate is converted to a volumetric flow rate (m^3/s) using the density of methane at the reactant temperature as follows:

$$\text{fuel}_{\text{m}^3/\text{s}} = \left(\frac{\dot{\text{m}}_{\text{fuel}}}{\rho_{\text{CH}_4}} \right) \tag{5.9}$$

Thus, the air consumption is calculated as follows:

$$\text{air}_{\text{m}^3/\text{s}} = \frac{\left(\frac{\dot{\text{m}}_{\text{fuel}} \cdot 3 \cdot \text{MMASS}(\text{O}_2)}{0.233 \cdot \text{MMASS}(\text{CH}_4)} \right)}{\rho_{\text{air}}} \tag{5.10}$$

where the factor 0.233 in the denominator is the fraction of oxygen by mass ($\text{mass}_{\text{fraction},\text{O}_2}$) in atmospheric air. This is calculated from the following equation:

$$\text{mass}_{\text{fraction},\text{O}_2} = \left(\frac{\text{MMASS}(\text{O}_2)}{\text{MMASS}(\text{O}_2) + 3.76 \cdot \text{MMASS}(\text{N}_2)} \right) \tag{5.11}$$

5.4: Results

The following discussion is based on the results for the optimal cycle. The variation of the temperature of the auxiliary mass is shown in Figure 5.3. The general trend of the plot is similar to the temperature variation of the aluminum mold wall for similar molding conditions. It increases sharply from 27^{o}C at the start and reaches a peak of 291^{o}C at the end of the heating cycle. Subsequently, at the completion of pre-cooling, it falls to 86^{o}C. During post-cooling, a higher heat transfer coefficient between the assembly and the ambient results in a steeper gradient in the housing temperature. The rate of this thermal energy transfer between the assembly and the surroundings is shown in Figure 5.4. As this rate is proportional to the temperature difference between the two, it is a maximum at the beginning when the difference is the maximum. The heat transfer rate decreases asymptotically, as the corresponding temperature difference gradually subsides. At the beginning of the pre-cooling process, this rate is again a negative maximum, as the temperature difference initially is the highest. As this stage progresses, the heat transfer rate decreases. The change in the heat transfer coefficient with the onset of the post-cooling process introduces a discontinuity in this variation due to the larger heat removal capability of forced convection. At the end of the post-cooling stage, the temperature difference between the housing and the surroundings (29.4^{o}C - 27^{o}C) is

minimal so that the rate of this heat transfer is essentially negligible. Corresponding results for the baseline cycle are presented in Figures 5.5 and 5.6 respectively.

The total energy consumed for heating the auxiliary mass in the heating process is 58 MJ for the baseline molding process (heating duration = 17 minutes) and 54 MJ for the *optimized molding* process (heating duration = 14 minutes). For the *optimized* process, the comparison of energy transfer rates to/from the housing and those for the 14 molds is shown in Figure 5.4. It is evident that the auxiliary mass absorbs a significant fraction of the energy input, i.e., approximately 73% of the total energy consumption, during the heating stage. Similarly, for the baseline process, the energy transfer rate is shown in Figure 5.6 and the auxiliary mass consumes 74.3% of the total energy input during heating.

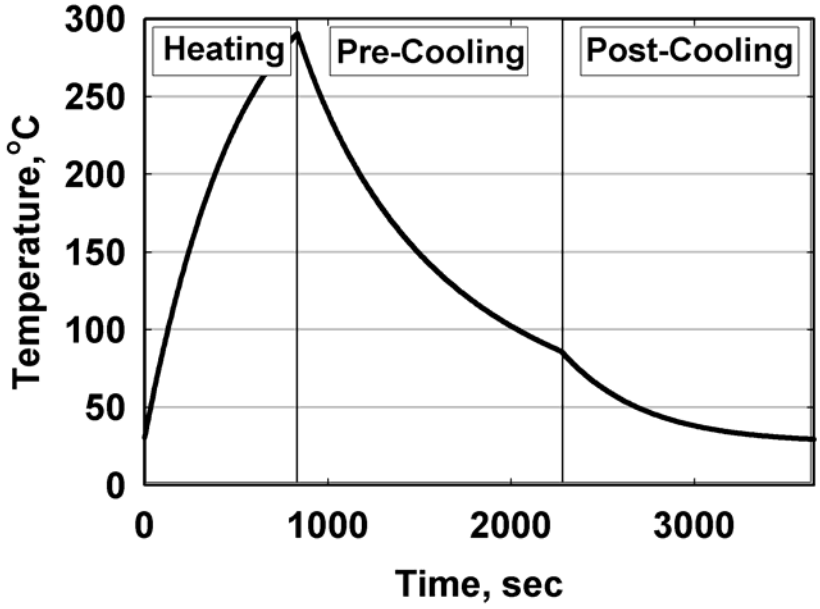

Figure 5.3: Variation in Temperature of Auxiliary Mass (*Optimized Cycle*)

From the analysis presented in Section 5.3, the air and fuel flow rates are found to be 4.76E-2 (101 cfm) and 3.35E-3 (7.1 cfm) m^3/sec respectively for the 17 min heating cycle (baseline process), including the energy required for the extra mass of the housing. Similarly for the optimized cycle with a heating duration of 14 minutes, the air and fuel flow rates are 5.27E-2 (112 cfm) and 3.71E-3 (7.9 cfm) m^3/sec respectively. The fuel flow rates are higher for the optimal case than for the baseline case; however, it should be

noted that the baseline heating duration is longer, the net effect being greater energy consumption (by 9.6%) in the baseline case.

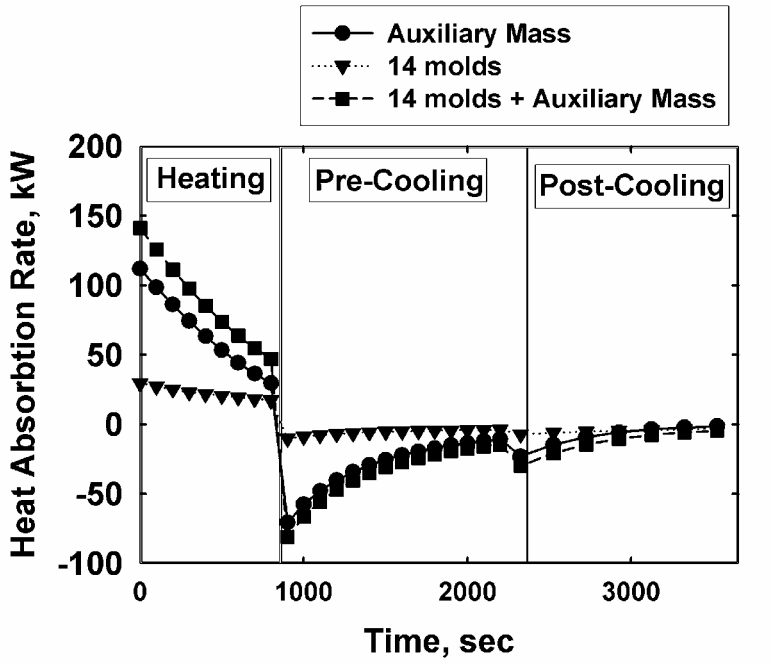

Figure 5.4: Variation in Heat Transfer Rate with Time (*Optimized Cycle*)

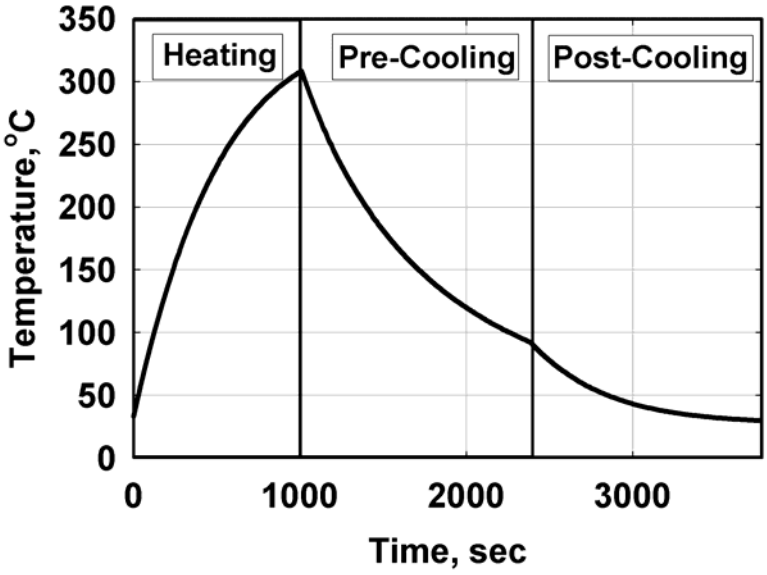

Figure 5.5: Variation in Temperature of Auxiliary Mass (*Baseline Cycle*)

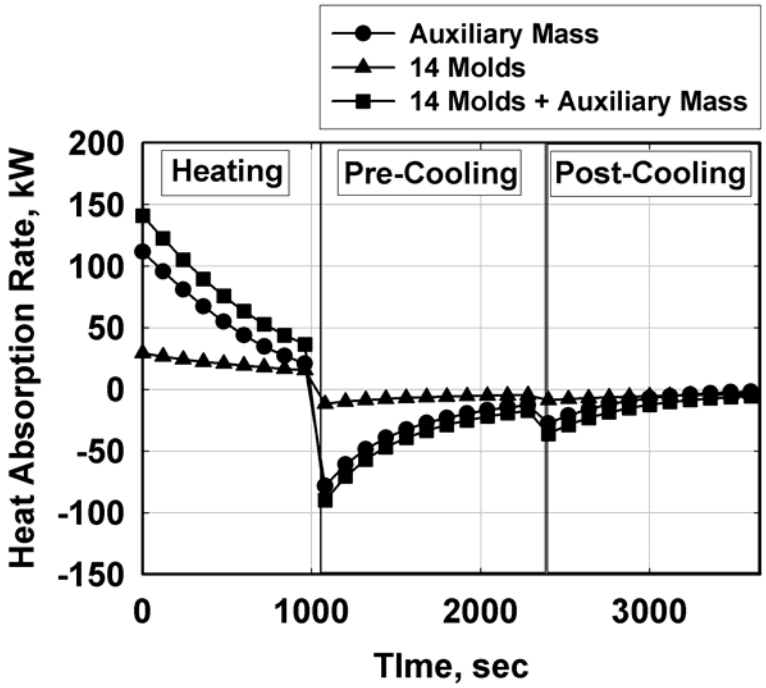

Figure 5.6: Variation in Heat Transfer Rate with Time (*Baseline Cycle*)

Table 5.3 summarizes the impact of the auxiliary housing on the energy and fuel consumption in the rotational molding process (baseline and optimized processes). The total energy consumption for the 14 molds (80 kg Aluminum; 19 kg plastic) is equal to 21.5 MJ for the baseline process (17 minutes heating). For the same heating duration, the energy consumption for the steel frame (418 kg) is 58 MJ. For the *optimized* process, these values are 18 and 54 MJ respectively. The energy and fuel consumption for the molds and the auxiliary housing is also shown schematically in Figure 5.7 for the baseline and optimized processes. It can be seen that although the modification of duty cycles results in some reduction in the energy consumption for the molds, the total energy consumption is not affected significantly.

As the heat input to the housing constitutes nearly 73% of the total energy input, it is appears that considerable energy savings can be realized by utilizing a different heating mechanism, in which the energy expended to heat the housing structure may be avoided or minimized. The auxiliary mass energy consumption may also be reduced using a material with a lower specific heat to reduce the thermal mass of the auxiliary structure; however, there are no readily available, relatively inexpensive materials that can be used

for the fabrication of such housing with a specific heat lower than that of carbon steel (0.434 kJ/kg-K).

Table 5.3: Impact of Auxiliary Housing on Energy and Fuel Consumption in Rotational Molding (Baseline and Optimized Processes)

		Molds	Auxiliary Mass	Percentage Contribution of Auxiliary Mass
Mass (kg)	14 Molds (Aluminum only) = 80 Note: Powder Mass = 19		Auxiliary Housing = 418	83.9%
Energy (MJ)	Baseline	Molds + Plastic = 21.46	Auxiliary Housing = 58	73.0%
	Optimized	Molds + Plastic = 18.60	Auxiliary Housing = 54	74.3%
Fuel (m^3)	Baseline	Molds + Plastic = 0.921	Auxiliary Housing = 2.49	73.0%
	Optimized	Molds + Plastic = 0.798	Auxiliary Housing = 2.32	74.3%

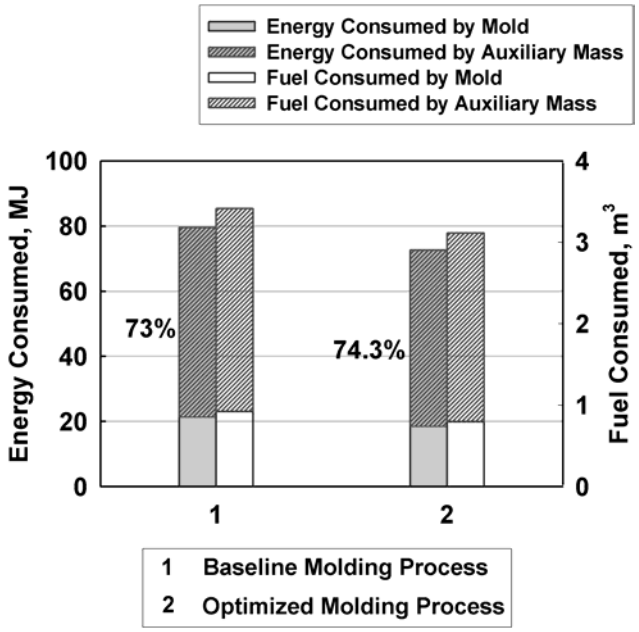

Figure 5.7: Energy and Fuel Consumption for the Original and Optimized Processes

CHAPTER 6

ALTERNATE HEATING AND COOLING MECHANISM

6.1: Proposed System Description

From the analyses and results presented in the previous chapters, it is evident that a significant fraction of the aggregate thermal energy for the rotational molding process is consumed in heating the auxiliary mass along with the batch of molds. Therefore, an alternative heating and cooling system is proposed and analyzed here in an attempt to reduce the overall energy consumption.

A heating and cooling scheme that uses heat transfer fluid flowing through small channels integral to the mold is investigated here as an alternative to the conventional process. Sixty-two rectangular tubes of dimension 5×2 mm ($w_{tube} \times h_{tube}$), which are integral to the mold wall, provide heat transfer flow paths for the heat transfer fluid (HTF) as shown in Figure 6.1. The small channels provide a higher heat transfer area for a lower HTF inventory. The heat transfer fluid circulation path around a single mold (during heating) is shown in Figure 6.2. During heating and cooling, the circulating HTF releases and absorbs heat to and from the mold respectively. The fluid enters the individual molds in parallel, and then splits into the 62 channels in each mold.

6.2: Selection of Heat Transfer Fluid

The heat transfer fluid (HTF) for jacket heating is selected from a list of commercially available DOW synthetic organic fluids (DOW 2004). Initially four fluids - 1) Dowtherm A; 2) Syltherm 800; 3) Dowtherm G; and 4) Dowtherm RP - were considered as they have an allowable operating temperature that is higher than the furnace temperature of 343^{o}C (650^{o}F), as shown in Table 6.1. Of these four candidate fluids, Dowtherm RP and Dowtherm G were selected due to their large specific heat in the allowable operating temperature range 0-350^{o}C (DOW 2004) as shown in Table 6.2 and Figure 6.3.

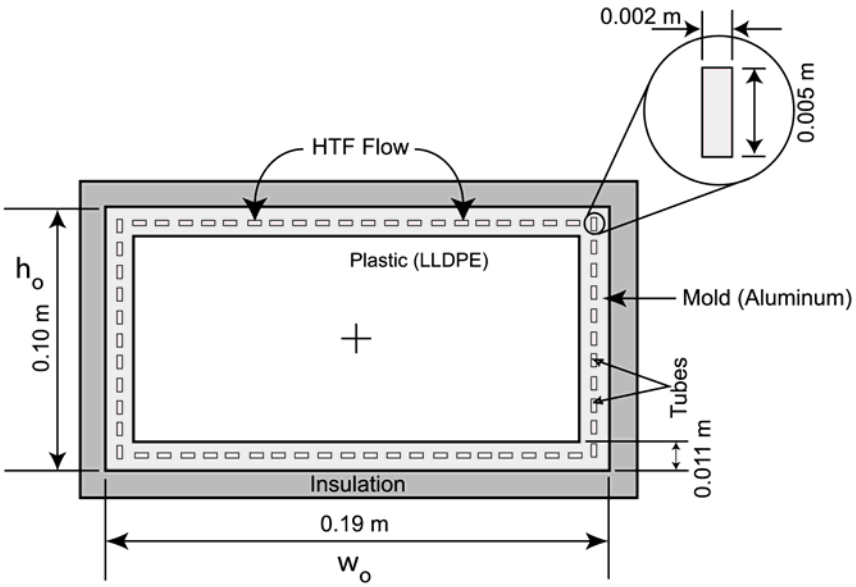

Figure 6.1: Mold Cross-Section with Integral Heating/Cooling Fluid Channels

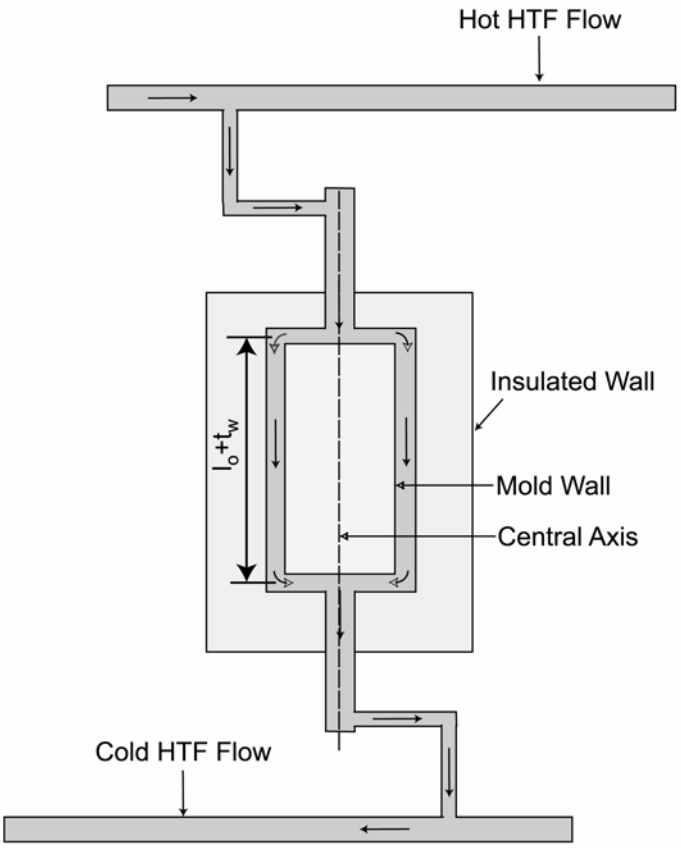

Figure 6.2: HTF Flow Circulation around the Mold during Heating

This table also lists the values of the densities, thermal conductivities and viscosities of these fluids at four temperatures within this range. It can be seen that at a particular temperature, the values of the densities and the thermal conductivities of these fluids do not vary much. Similarly, at higher temperatures, the viscosities of these fluids at a particular temperature are comparable. Among these two fluids (Dowtherm RP and Dowtherm G), Dowtherm RP is selected, because it has a higher thermal capacity in the temperature range 50 ~ 190°C (Figure 6.3) which is the operating range for a significant portion of the cycle. Above 190°C, although the thermal capacity of Dowtherm RP is lower than that of Dowtherm G, the penalty is not expected to be very large (e.g., at 350°C, C_p for Dowtherm RP is 2.60 and for Dowtherm G is 2.70 kJ/kg-K).

Table 6.1: Operating Temperature Ranges for Dow Fluids (Dow 2004)

Fluid	**Operating Temperature (°C)**	
	Low	**High**
Dowtherm A (liquid)	15	400
Syltherm 800	-40	400
Dowtherm G	-7	360
Dowtherm RP	0	350

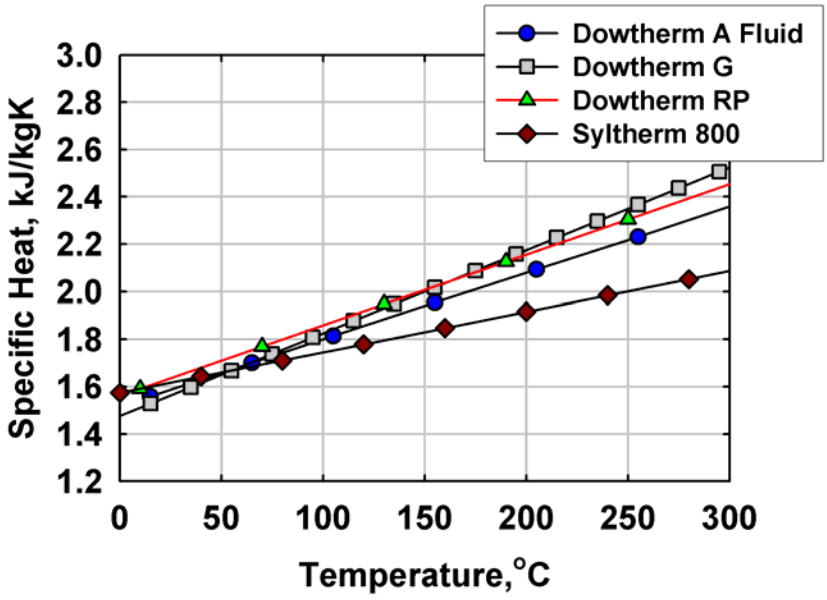

Figure 6.3: Variation of Specific Heat of the Dow Fluids

Table 6.2:Thermo-physical Properties of Dow Fluids at Temperatures in the Operating Range (0-350^{o}C) (Dow 2004)

Fluid	Temperature (^{o}C)	Density (kg/m^{3})	Specific Heat (kJ/kg-K)	Thermal Conductivity (W/m-K)	Viscosity (mPa.s)
Dowtherm A (liquid)	50	1035.83	1.66	0.13	2.07
	150	952.20	1.94	0.12	0.58
	250	859.06	2.22	0.10	0.28
	350	748.59	2.51	0.08	0.16
Syltherm 800	50	908.18	1.66	0.13	5.95
	150	819.51	1.83	0.11	1.70
	250	724.24	2.00	0.09	0.68
	350	612.33	2.17	0.07	0.33
Dowtherm G	50	1023.63	1.65	0.12	4.62
	150	946.15	2.00	0.11	0.95
	250	868.67	2.35	0.09	0.40
	350	791.19	2.70	0.08	0.22
Dowtherm RP	50	1008.26	1.17	0.13	10.05
	150	937.34	2.00	0.11	1.32
	250	863.81	2.31	0.10	0.54
	350	784.96	2.60	0.08	0.31

6.3: Thermal Models

In the analysis of the proposed system, the aluminum mold is assumed to be at a uniform temperature because from the previous analysis, it is inferred that the temperature variation in the mold wall is negligible. The basic model for the heat transfer through the mold wall and inside the molds (which includes the plastic) remains the same as the previous baseline thermal analysis. The primary difference is the use of a single mold wall segment instead of the three segments used in the baseline analysis due to the uniformity of wall temperature. With the major portion of the thermal analysis being similar to that for the baseline system, internal details of the thermal models for the mold and plastic are not repeated here. Only the calculations pertinent to the heat transfer fluid are emphasized.

The thermal properties of the HTF are calculated at the inlet temperature of the HTF. The hydraulic diameter (D_{hyd}) of the tubes is calculated as follows:

$$D_{Hyd} = \left(\frac{2 \cdot w_{tube} \cdot h_{tube}}{w_{tube} + h_{tube}} \right) \tag{6.1}$$

where the width and the height of the tubes are 5 and 2 mm respectively (as shown in Figure 6.3). For this geometry, the hydraulic diameter is 2.86 mm.

A flow velocity (vel_{HTF}) of 0.2 m/sec was chosen for these analyses to keep fluid pressure drop within an acceptable value of 34.47 kPa (5 psi). For this combination of hydraulic diameter and velocity, the Reynolds Number (Re_{HTF}) is less than 2300. Hence, the flow is laminar. The friction factor and Nusselt number for the fluid flowing through these channels were calculated using correlations by Churchill (1977b; 1977a), which are applicable for laminar, transition and turbulent flow. The heat transfer coefficient is calculated from the Nusselt number as follows:

$$h_{coeff,HTF} = Nu_{HTF} \cdot \left(\frac{k_{HTF}}{D_{Hyd}} \right) \tag{6.2}$$

From the geometry of the jackets (Figure 6.2), the length of a fluid channel is as follows:

$$L_{jacket} = \left(l_o + t_w \right) \tag{6.3}$$

Therefore, the total surface area of the channels in contact with the HTF is as follows:

$$A_{channel} = \left[2 \cdot \left(w_{tube} + h_{tube} \right) \cdot L_{jacket} \right] \times N_{channel} \tag{6.4}$$

where $N_{channel}$ is the number of channels per mold (62). It should be noted that in this calculation of heat transfer surface area, it is assumed that the four surfaces of the channels are equally effective in transferring heat from the fluid to the mold and the plastic, even though only one surface of the channel wall is in direct contact with the plastic. This is a reasonable assumption due to the high thermal conductivity of Aluminum (239 W/m-K @ 150^{o}C).

Hence, the heat convected from the HTF is as follows:

$$Q_o = h_{coeff,HTF} \cdot A_{channel} \cdot \left(\frac{T_{HTF,in} + T_{HTF,out}}{2} - T_l \right) \quad (6.5)$$

This heat transfer is reflected in a drop in temperature of the HTF (from $T_{HTF,in}$ at the inlet to $T_{HTF,out}$ at the outlet) as follows:

$$Q_o = \dot{m}_{HTF,} C_{p,HTF} \left(T_{HTF,in} - T_{HTF,out} \right) \quad (6.6)$$

where the mass flow rate of the HTF ($\dot{m}_{HTF,}$) for a single mold is estimated as follows:

$$\dot{m}_{HTF} = vel_{HTF} \cdot w_{tube} \cdot h_{tube} \cdot \rho_{HTF} \cdot N_{channel} \quad (6.7)$$

During the heating process, the aluminum enclosure absorbs part of the thermal energy input. This is equal to the following:

$$Q_{aux} = m_{aux} \cdot C_{p,Al} \cdot \left(\frac{T_{1,f} - T_{1,s}}{\Delta t} \right) \quad (6.8)$$

where m_{aux} is the mass of this enclosure, calculated from the volume, which is as follows:

$$vol_{aux} = w_o h_o l_o - (w_o - 2t_w)(h_o - 2t_w)(l_o - 2t_w) - (w_{tube} h_{tube} L_{jacket} \times N_{channel}) \quad (6.9)$$

The energy, transferred to the plastic, is therefore as follows:

$$Q_{input} = Q_o - Q_{aux} \quad (6.10)$$

This is equivalent to Q_p, which is the heat convected and stored in the plastic powder in the mold cavity, as in the baseline model. As stated above, details internal to the mold wall remain the same as for the baseline model.

As before, a simultaneous solution of these energy equations yields the temperature at the end of each time step, which serves as the input for the next step. The iterations progress with time until the end of the phase, which marks the beginning of the melting phase. The heat transfer process is illustrated in Figure 6.4. This is similar to the baseline process except for the single mold segment as mentioned before. This model is extended to the subsequent stages of the molding process, as was the case for the baseline model.

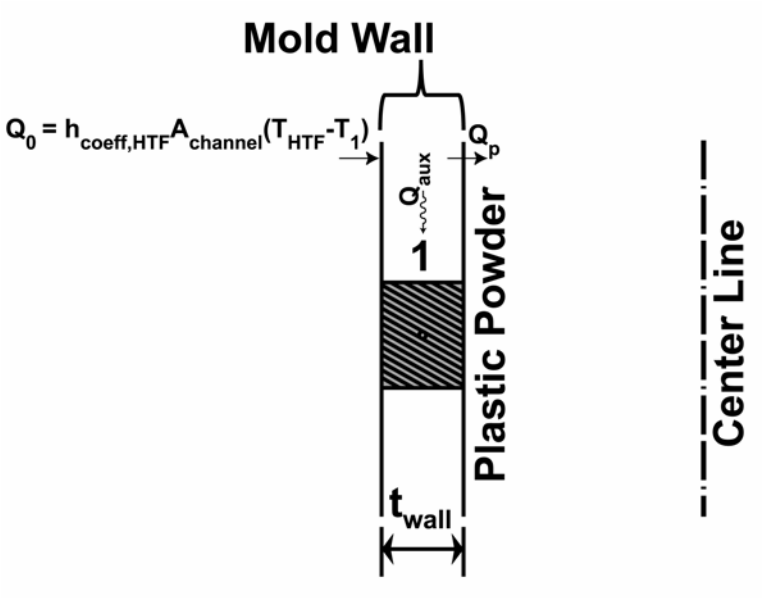

Figure 6.4: Energy Transfer during Transient Heating of Plastic Powder

6.4: Heat Transfer Fluid (HTF) Circulation Options

In the present study, **four** heat transfer fluid circulation options are considered as follows:

A. Direct Jacket Heating
   a. Coupled to Open-Loop Cooling Water
   b. Coupled to Closed-Loop Cooling and Storage Tank

B. Jacket Heating with Pre-Heat/Recuperation
   a. Coupled to Open-Loop Cooling Water
   b. Coupled to Closed-Loop Cooling Water and Storage Tank

6.4.1: Heating Option A – Direct Jacket Heating

The circulation of the HTF during the heating cycle is shown in Figure 6.5. The HTF absorbs heat from the furnace and delivers it to a storage tank. The function of this storage tank in the model is to simulate an expansion tank that would be required for the real system to account for density changes in the fluid as its temperature changes during the cycle. Although a 5 kg tank was chosen somewhat arbitrarily, the actual volume or mass of this fluid inventory will be determined by the layout of the actual system in the plant. This storage tank is coupled to the set of molds to accomplish heating. After

heating the molds, the HTF from the outlet is routed back to the furnace heat exchanger and once again receives heat from the flue gas. The volumetric flow rate of the HTF ($flow_{rate}$) through the channels is calculated as follows:

$$flow_{rate} = vel_{HTF} \cdot w_{tube} \cdot h_{tube} \cdot N_{channel} \cdot 14 \qquad (6.11)$$

for the batch of 14 molds. For the chosen dimensions of these channels (w_{tube} = 5 mm; h_{tube} = 2 mm) the fluid loop has a flow rate of 1.736E-3 m^3/sec (27.5 gpm). The total mass flow rate of the HTF ($m_{HTF,rate}$) is obtained from the volumetric flow rate, or alternatively, from Equation 6.7.

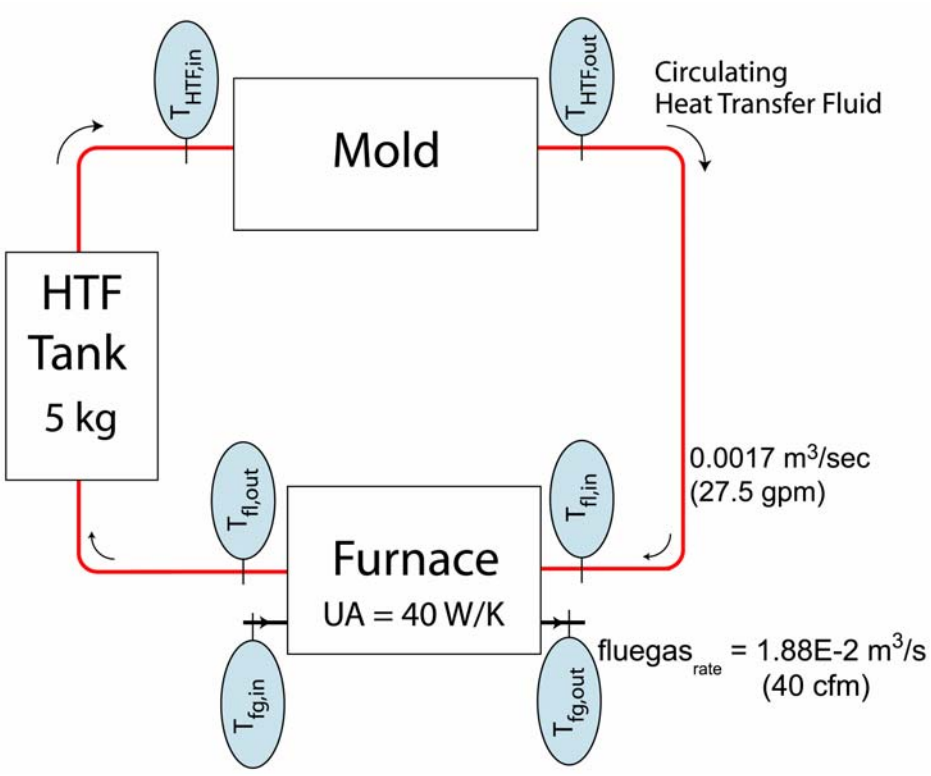

Figure 6.5: Circulation of HTF during Heating (Option A)

A preliminary design of a natural gas combustion crossflow heat exchanger with an overall thermal conductance UA of 40 W/K that heats the HTF was conducted. The resulting heat exchanger has dimensions (L×H×W) of 127 mm (5 in) × 125 mm (4.9 in) × 23 mm (0.9 in). Hot flue gas from the furnace flows through the multi-louvered fins and the HTF flows through the bank of ten tubes of the heat exchanger in parallel. The design of this combustion heat exchanger, which is made of steel, is summarized in

Appendix B. The required gas flow rates for this heat exchanger were estimated using a simple thermodynamic analysis of the combustion of CH_4 in 50% excess air, as was described in Chapter 5. Based on this analysis, a natural gas flow rate of 1.21E-3 m^3/sec (2.5 cfm) is used, which results in a flow rate of the combustion products ($fluegas_{rate}$) of 1.88E-2 m^3/sec (40 cfm). The air flow rate is calculated to be 1.70E-2 m^3/sec (36 cfm).

Transient heat transfer calculations for the heating phase are described below, using these flow rates for the gas and the HTF. For these calculations, the flue gas inlet at the furnace-to-HTF heat exchanger is assumed to be at the adiabatic flame temperature. The thermophysical properties of the flue gas and the HTF are calculated at the mean temperatures of the respective fluids in this heat exchanger.

For a particular time step Δt, the temperatures at the outlet of the furnace heat exchanger are calculated using the ε-NTU method for cross flow (single pass) with both fluids unmixed. The effectiveness, ε_f, for this configuration is given as follows (Kays and London 1984):

$$\varepsilon_f = 1 - \exp\left(\frac{1}{C_r} \cdot NTU^{0.22} \cdot \left(\exp\left(-C_r \cdot NTU^{0.78}\right) - 1\right)\right) \tag{6.12}$$

where C_r is the ratio of the minimum (C_{min}) and maximum (C_{max}) heat capacity rates of the two fluids (C_{fg} for flue gas; C_{HTF} for HTF) and NTU, the number of transfer units. Therefore, the heat transfer rate in this heat exchanger is given as follows:

$$\dot{Q} = \varepsilon_f \cdot C_{min} \cdot \left(T_{fg,in} - T_{fl,in}\right) \tag{6.13}$$

The outlet temperatures of the HTF and flue gas are calculated from the heat duty as follows:

$$T_{fl,out} = T_{fl,in} + \frac{\dot{Q}}{C_{HTF}} \tag{6.14}$$

and

$$T_{fg,out} = T_{fg,in} - \frac{\dot{Q}}{C_{fg}} \tag{6.15}$$

respectively.

This hot HTF from the furnace heat exchanger outlet ($T_{fl,out}$) is delivered to the storage tank as shown in Figure 6.5. At the beginning of the time step, the temperature of the HTF in this tank is equal to $T_{HTF,in}$ (which is delivered to the molds). The total energy absorbed by the circulating HTF from the flue gas during this time step, which is equal to $\dot{Q} \cdot \Delta t$, is divided between heating the HTF in this storage tank and the batch of molds. This energy balance is represented as follows:

$$Q_{tank} = \dot{Q} \cdot \Delta t - Q_{mold} \tag{6.16}$$

The temperature of the HTF in the tank increases to $T_{HTF,next}$ from $T_{HTF,in}$ at the end of the time step Δt. The energy absorbed by the mass of HTF in the tank ($mass_{HTF,total}$ = 5 kg) is as follows:

$$Q_{tank} = mass_{HTF,total} \cdot C_{p,HTF} \cdot \left(T_{HTF,next} - T_{HTF,in}\right) \tag{6.17}$$

where $C_{p,HTF}$ is the specific heat capacity of the HTF. Similarly, the energy transferred to the molds is as follows:

$$Q_{mold} = C_{HTF} \cdot \left(T_{HTF,in} - T_{HTF,out}\right) \cdot \Delta t \tag{6.18}$$

where C_{HTF} is the heat capacity rate of the HTF as mentioned before and $T_{HTF,in}$ and $T_{HTF,out}$ are temperatures of the HTF at the inlet and the outlet of the molds respectively at the beginning of the time step (In formulating these energy equations, the variation of the specific heat capacity of the HTF over the loop for a particular time step is neglected). It should be noted that $T_{HTF,out}$ is calculated by solving the set of simultaneous equations governing the energy transfer in the mold and the plastic (Chapter 3) coupled to the temperature at the inlet ($T_{HTF,in}$) To complete the loop, the HTF from the mold outlet is delivered to the furnace heat exchanger ($T_{HTF,out} = T_{fl,in}$) (Figure 6.5). It should be noted that heat losses in the plumbing connecting the various components in the loops under discussion in this chapter are neglected for this preliminary analysis.

Combining Equations 6.16-6.18 yields the following:

$$mass_{HTF,total} \cdot \left(T_{HTF,next} - T_{HTF,in}\right) = \left(\left(T_{fl,out} - T_{fl,in}\right) - \left(T_{HTF,in} - T_{HTF,out}\right)\right) \cdot \left(m_{HTF,rate} \cdot \Delta t\right) \tag{6.19}$$

The solution of the above equation yields the temperature of the HTF in the storage tank at the end of the time step ($T_{HTF,next}$), which is used as the inlet temperature at the molds for the subsequent time step ($T_{HTF,in}$). For a representative instant 5 minutes

into the heating stage, the HTF enters the flue gas heat exchanger at 162.8°C, and is heated to a temperature of 171°C. The storage tank temperature changes from 170.2°C to 170.4°C in a time step of 1 second at this time. At the beginning of the time step, the fluid enters the molds at 170.2°C and exits at 162.8°C to return to the flue gas heat exchanger. During this process, 27.29 kJ are transferred from the flue gas to the fluid, while 2.94 kJ are stored in the tank and 24.35 kJ are supplied to the molds.

These calculations proceed for subsequent time intervals until the end of the heating cycle, which concludes when the entire plastic inventory in the mold melts.

6.4.2: Corresponding Cooling Options

6.4.2.1: Open-Loop Cooling Water (Option 1)

At the completion of the heating cycle, the furnace is replaced by an open-loop cooling water stream, which cools the circulating HTF as shown in Figure 6.6. For this analysis, the mass flow rate of the open loop cooling water ($m_{wtr,rate}$) is assumed to be 4 kg/sec (64 gpm). The mass flow rate of the HTF is not changed between the heating and the cooling modes. Heat exchange between the HTF and the water is accomplished in a shell-and-tube heat exchanger with a UA of 1000 W/K. It has an internal shell diameter of 5.08 cm (2 in) and a length of 1.00 m (3.28 ft). The hot HTF flows through 14 tubes of 6.35 mm (0.25 in) OD, 5.84 mm (0.23 in) ID for a heat transfer area of 0.2793 m^2. Cooling water flows through the shell side across 10 baffles. The pressure drops on the shell side and tube side are 1.68 kPa (0.24 psi) and 32.16 kPa (4.66 psi), respectively. The design of this heat exchanger is summarized in Appendix C.

Heat transfer calculations in the cooling mode are similar to those described above for the heating mode. In this case, the energy ($\dot{Q} \cdot \Delta t$) rejected to the water sink during time Δt is partially used to cool the HTF in the tank and the remaining energy is used to cool the batch of molds. During a representative time step 5 minutes into the start of the cooling cycle, the HTF enters the water-to-HTF heat exchanger at 60.1°C, and is cooled to a temperature of 50.9°C. The storage tank temperature changes from 51.2°C to 50.7°C during a 5-second time step at this time. At the beginning of the time step, the fluid enters the molds at 51.2°C and exits at 60.1°C to return to the water-to-HTF heat

exchanger. During this process, 137.4 kJ are transferred from the HTF to the open-loop water, while 4.23 kJ are rejected from the tank and 133.2 kJ are rejected by the molds.

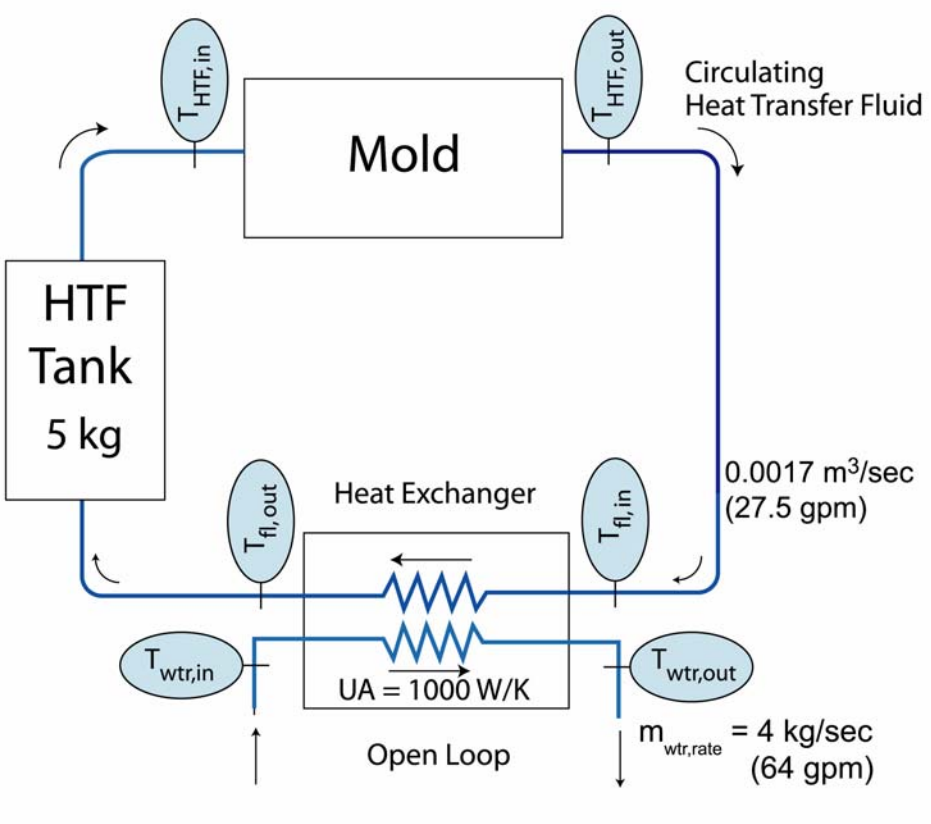

Figure 6.6: Open-Loop Cooling (Option 1)

6.4.2.2: Closed-Loop Cooling Water and Storage Tank (Option 2)

In this model, the open loop water is replaced by water flowing in a closed loop that includes a 200 kg water ($mass_{wtr,total}$) storage tank as shown in Figure 6.7. Water from this tank is supplied at the same mass flow rate ($m_{wtr,rate}$ =4 kg/sec) as in the open loop case and exchanges heat with the HTF flowing in the main loop. The heat exchange processes in this case are similar to those for the open loop case, except for the fact that the temperature of the cooling water ($T_{wtr,in}$) at the inlet to the heat-exchanger is *not* constant. Here, the water from the outlet of the water-to-HTF heat exchanger ($T_{wtr,out}$) is

routed back to the water tank, thus progressively raising the temperature of the heat sink as cooling proceeds. The same heat exchanger that was used in the open-loop case (with a UA of 1000 W/K) was used here.

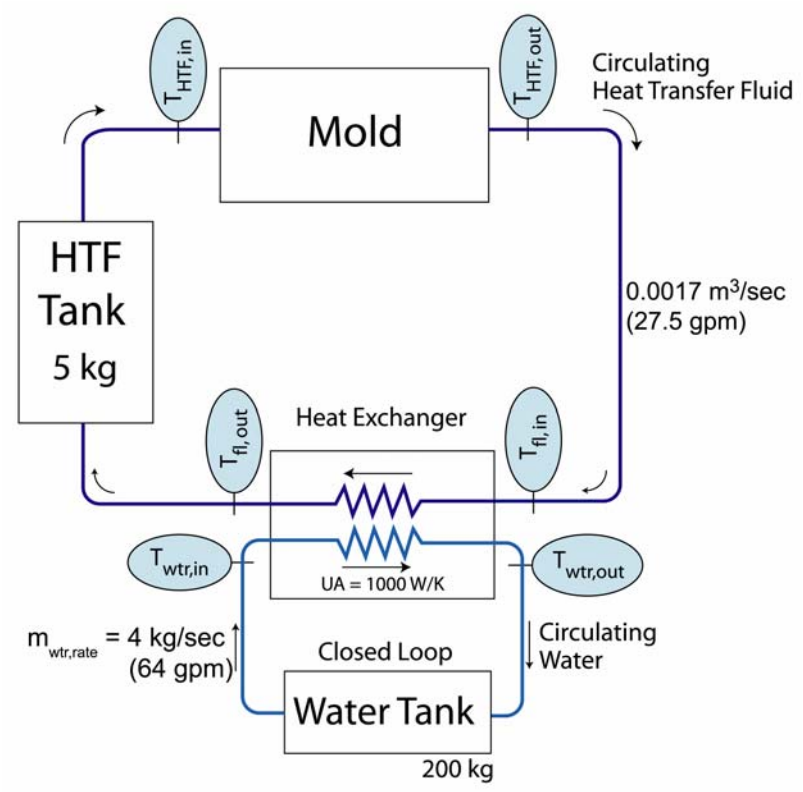

Figure 6.7: Closed-Loop Cooling with Water Storage (Option 2)

The simultaneous solution of the corresponding heat transfer equations gives the temperatures of the HTF and the water in the respective storage tanks. For a representative time step 5 minutes into the start of the cooling cycle, the HTF enters the water-to HTF heat exchanger at 75.7°C, and is cooled to a temperature of 67.9°C. The HTF storage tank temperature changes from 68.1°C to 67.8°C during a 5-second time step at this time. At the beginning of this time step, the fluid enters the molds at 68.1°C and exits at 75.7°C to return to the water-to HTF heat exchanger. During this process, 119.0 kJ are transferred from the fluid to the closed-loop water, while 2.8 kJ are rejected from the tank and 116.2 kJ are rejected by the molds. It should be noted that due to the closed-loop nature of the heat sink, 241.3 kW are rejected from the HTF into the water at the beginning of the cooling cycle, when the water in the tank is at 27°C. At the end of

the cooling cycle, the water temperature rises to 55.9°C (at which time the HTF enters the HTF-to-water heat exchanger at 57.8°C), reducing the rejection rate to 1.59 kW. The heated water in the tank at the end of the cycle is available for other process heating and building hot water needs in the plant.

6.4.3: Heating Option B – Jacket Heating with Pre-Heat/Recuperation

In this model, the HTF is pre-heated using a hot recuperation fluid that circulates in a secondary loop as shown in Figure 6.8. The pre-heating process continues for the first five minutes of the heating cycle, followed by heating of the HTF by combustion gases. The recuperation fluid is contained in a 200 kg ($mass_{cf,total}$) storage tank. The initial temperature of the fluid in this storage tank is 166°C, and the fluid flows through the recuperative heat exchanger at 4 kg/sec.

The 166°C temperature of the recuperation fluid is established by running the simulations over several recuperation and pre-heat cycles until the temperature cycles between 166°C and 146.5°C at the beginning and end of the pre-heat cycle. Details of the recuperation fluid are tabulated in Table 6.3. The recuperative heat exchanger is similar to the HTF cooling heat exchanger (UA = 1000 W/K) used in the previously discussed configurations.

Table 6.3: Recuperation Fluid Details

Fluid	Same as Heat Transfer Fluid (HTF)
Mass of fluid ($mass_{cf,total}$)	200 kg
Mass flow rate of fluid ($m_{cf,hx,rate}$)	4 kg/sec (68 gpm)
Pre-heat Duration	5 minutes
Initial Temperature	166°C

As preheating proceeds, the temperature of the recuperation fluid in the tank decreases from 166°C to 146.5°C over the 5 minute duration, and the heat transfer rate to the HTF decreases from an initial value of 112.7 kW to 8.1 kW at the end of the preheating phase. At the end of the preheat phase, the HTF flowing in the main loop is heated directly from the furnace as shown by the solid lines in Figure 6.8. Due to the

change in the heating mechanism, the heat transfer rate to the HTF suddenly increases to 27.8 kW.

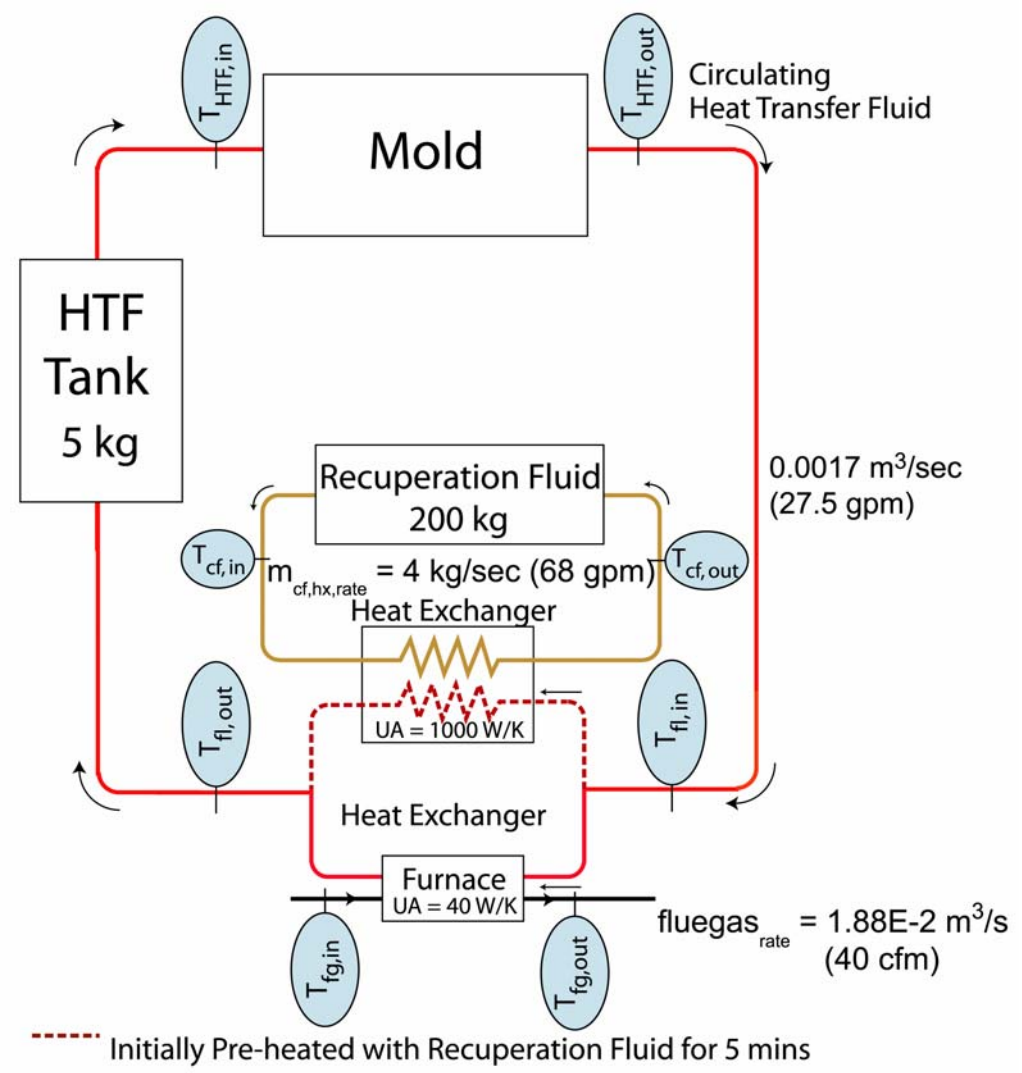

Figure 6.8: Circulation of HTF during Heating (Option B)

6.4.4: Corresponding Cooling Options

6.4.4.1: Open-Loop Cooling (Option 3)

At the end of the heating process, the HTF circulating through the main loop is initially cooled using the same recuperation fluid for a five minute duration as shown in Figure 6.9. The recuperation fluid is initially at a temperature of 146.5^{o}C as calculated in the heating phase, and is used to pre-cool the circulating HTF in the main loop. As pre-cooling proceeds, the recuperation fluid rises in temperature from 146.5 to 166^{o}C, beyond which recuperative cooling cannot be sustained. Heat rejection from the HTF falls from 196.7 kW at the start of the pre-cooling to 14.1 kW at the end of this stage. The volumetric flow rates of the recuperation fluid and water are different for the same mass flow rate due to difference in densities of the two fluids. At the beginning of pre-heating and cooling process, the densities of the recuperation fluid and water are 930.9 and 995.4 kg/m^3 respectively which yields flow rates of 68 and 64 gpm for the two fluids.

After this pre-cooling phase, the mold is cooled using the HTF flowing in the main loop, which now rejects energy to open-loop water. Due to this change in coolant, heat transfer from the HTF increases suddenly to 203.6 kW, and progressively decreases to 23.1 kW at the end of the cooling phase due to the decreasing temperature of the mold.

6.4.4.2: Closed-Loop Cooling (Option 4)

The open-loop water is replaced by a water tank (closed-loop) in this model as shown in Figure 6.10. The water is contained in a 150 kg storage tank. This is lower than the mass of water in the tank (200 kg) for closed loop cooling without recuperation because the pre-cooling step with the recuperation fluid is used to partially cool the HTF flowing in the main loop.

As pre-cooling proceeds, the recuperation fluid rises in temperature from 146.5 to 166^{o}C, beyond which recuperative cooling cannot be sustained. Heat rejection from the HTF falls from 136.2 kW at the start of the pre-cooling to 8.8 kW at the end of this stage.

The mold is subsequently cooled using the HTF flowing in the main loop, which now rejects energy to closed-loop water. Due to this change in coolant, heat transfer from the HTF increases suddenly to 125.8 kW, and progressively decreases to 8.5 kW at the end of the cooling phase due to the decreasing temperature of the mold.

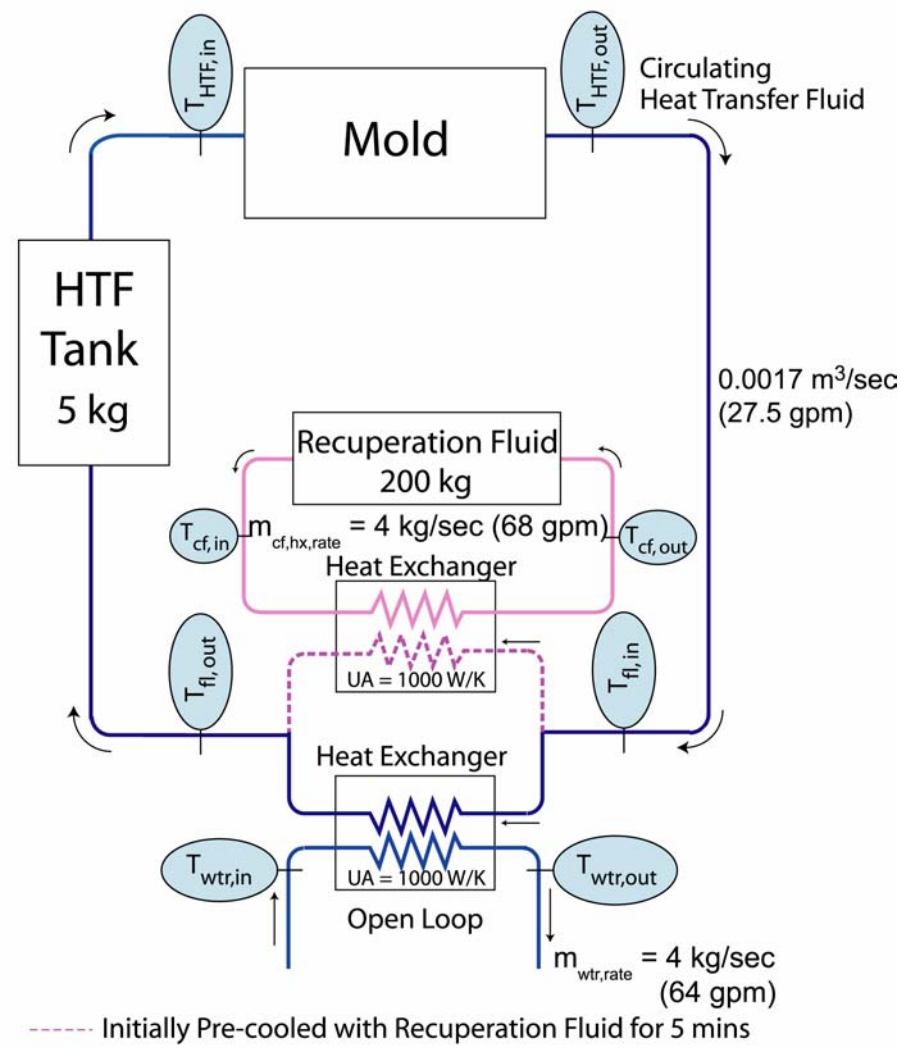

Figure 6.9: Open-Loop Cooling with Recuperation (Option 3)

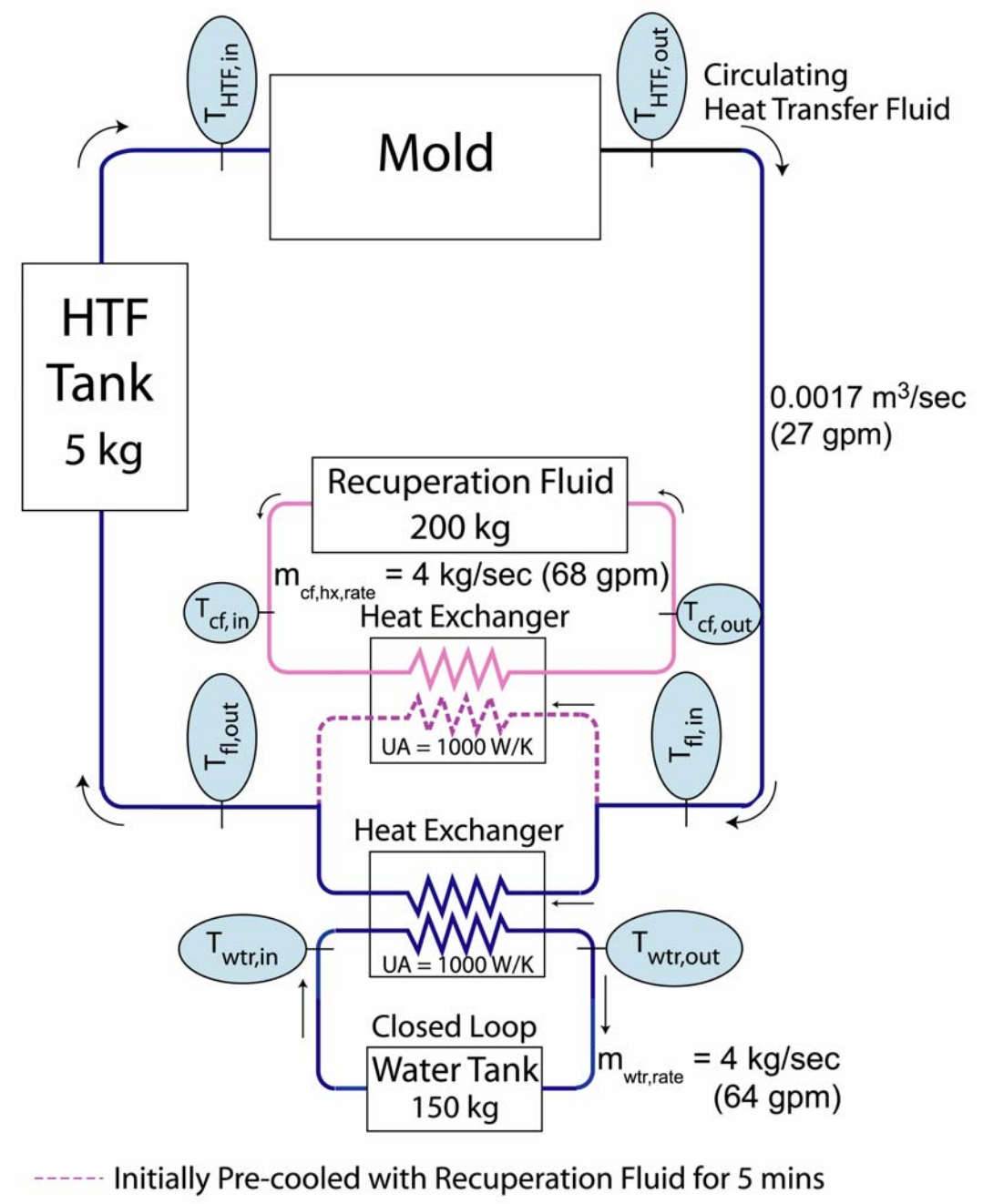

Figure 6.10: Closed-Loop Cooling with Recuperation (Option 4)

6.5: Results and Discussion

Transient temperature profiles for each of these four options during the heating and cooling stages are shown in Figures 6.11 to 6.14.

From Figure 6.11 (Option 1 – direct jacket heating coupled to open-loop cooling water), it is observed that the temperature profiles of the mold and the plastic are similar to those seen in the baseline furnace-heated molds (Figure 3.17). The HTF in the tank rises from 27^{o}C to 317.4^{o}C at the end of the heating process and cools to 29.26^{o}C during the cooling process. The heating duration lasts for 17 minutes 45 seconds. This consists of a transient heating phase of approximately 5 minutes followed by a phase change melting phase as indicated by the change in slope in the temperature profiles. During the cooling phase, the open-loop water outlet temperature first rises to 41.45^{o}C as it receives heat from the mold, followed by a gradual cool down to 27.2^{o}C as the heat rejection decreases. (The hottest outlet temperature occurs at the beginning of the cooling cycle.) The entire cooling process lasts for 21 minutes 17 seconds. This consists of a transient single phase cooling of the melt for approximately 3 minutes followed by solidification. The total energy consumption for this option is 25.2 MJ.

In Figure 6.12, which shows the temperature variation for Option 2 (direct jacket heating coupled to closed-loop cooling water), the water in the storage tank is heated from 27^{o}C to 55.87^{o}C as it receives the heat rejected by the mold. This can be used for other process needs in the plant. The temperature of the HTF in the tank decreases to 57.24^{o}C after the cooling schedule. This is higher than the previous option because the closed-loop water provides a lower heat transfer rate, because at the inlet to the heat exchanger, the temperature difference is always higher for the open loop than for the closed loop. The heating schedule for this option is unchanged from the previous option (17 minutes 45 seconds). However, the cooling cycle is extended to 25 minutes 35 seconds from the previous duration of 21 minutes 17 seconds.

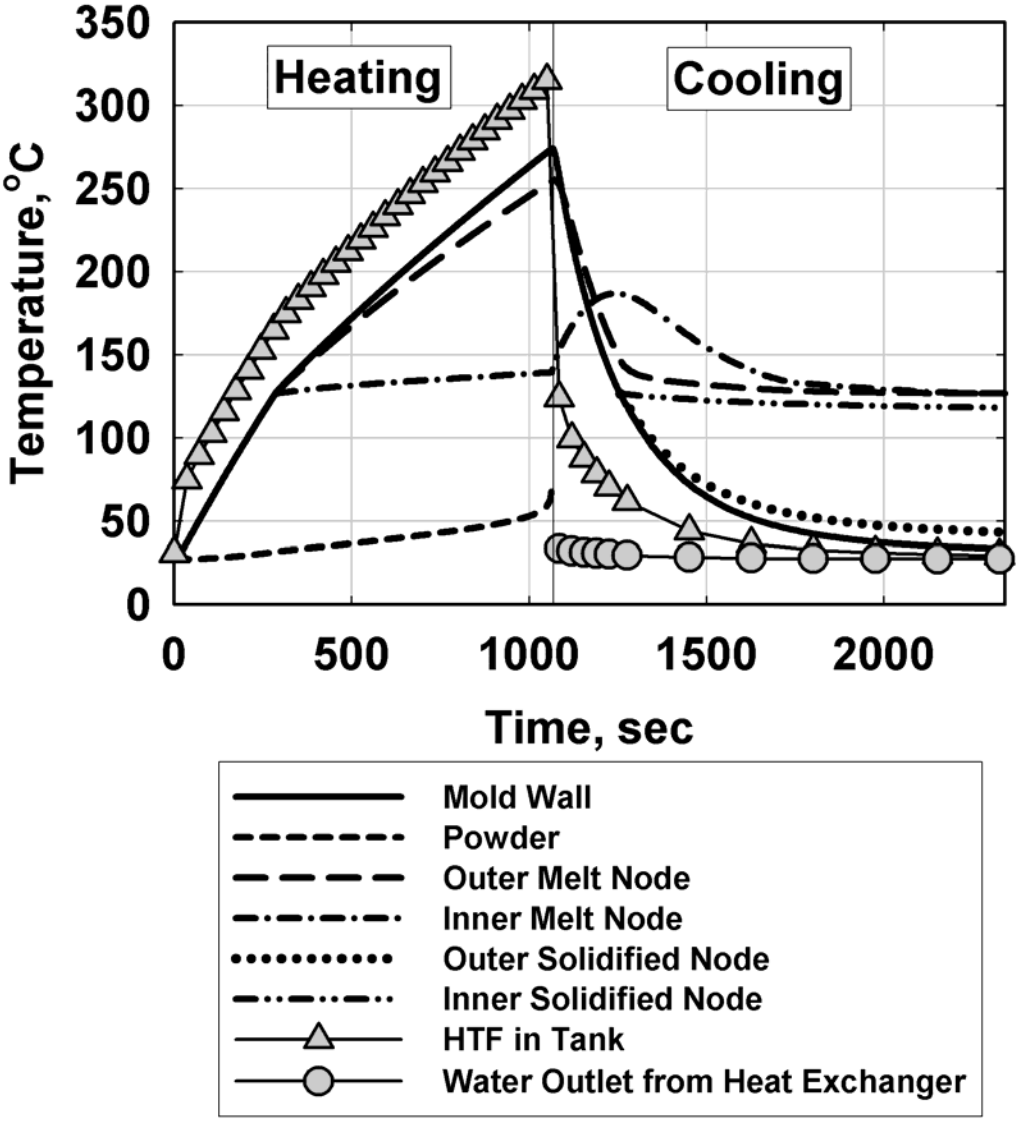

Figure 6.11: Temperature Profile for Direct Jacket Heating and Open-Loop Water Cooling

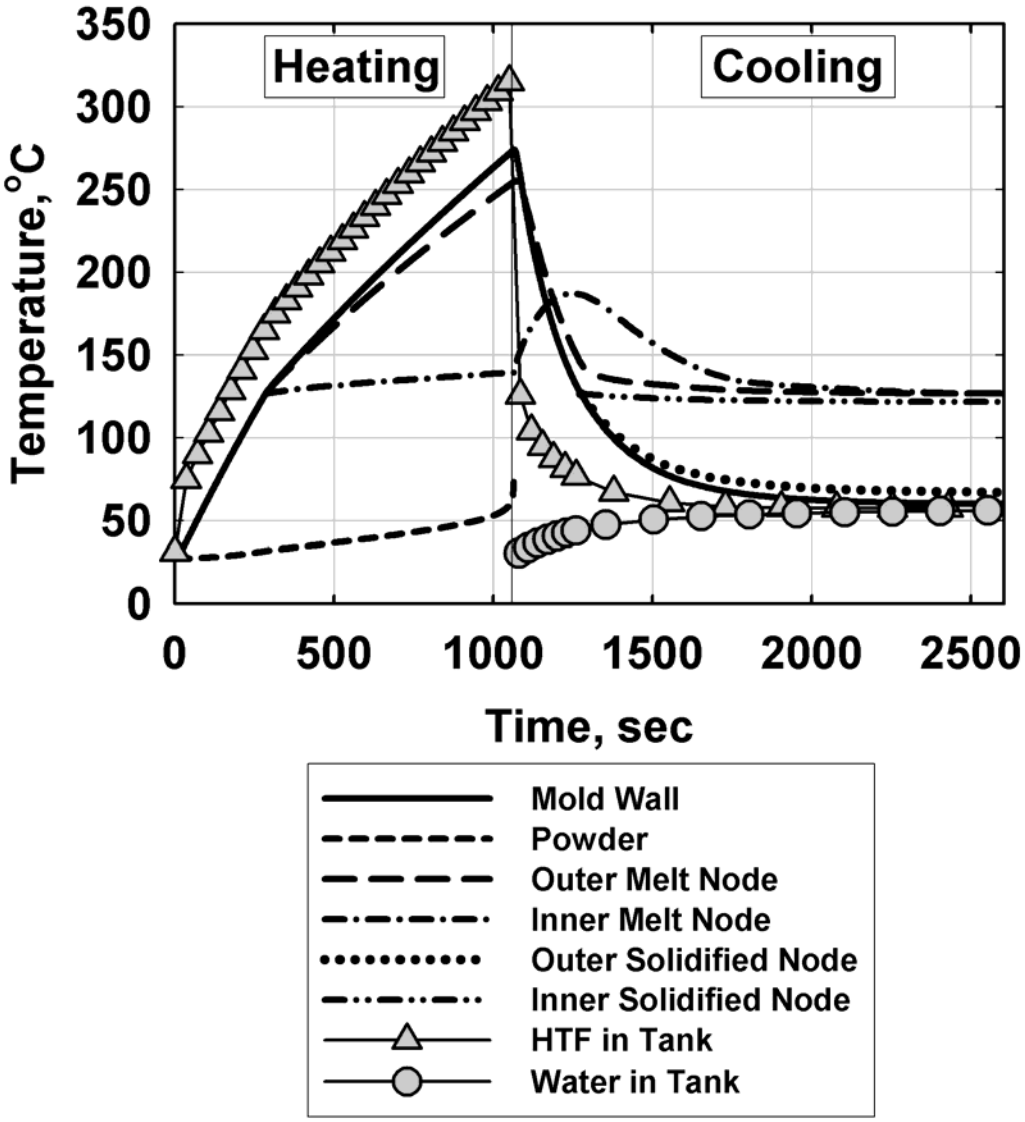

Figure 6.12: Temperature Profile for Direct Jacket Heating and Closed-Loop Water Cooling

Figure 6.13 shows the temperatures for Option 3 (jacket-heating with pre-heat/recuperation coupled to open-loop water). After pre-heating a batch of molds, the temperature of the recuperation HTF falls to 146.5^{o}C from 166^{o}C, and after combustion heating, this is used to pre-cool the same batch, during which it increases in temperature from 146.5^{o}C to 166^{o}C. This cycle continues for subsequent batches. The pre-heating process lasts for 5 minutes at the end of which the plastic powder begins to melt. This is followed by direct heating of the HTF in the main loop by the furnace, which lasts for 13 minutes. This is followed by a 5 minute pre-cooling process as mentioned before. Finally, the HTF is cooled by the open-loop water. During the cooling phase, the open-loop water outlet temperature first rises to 34.5^{o}C as it receives heat from the mold, followed a gradual cool down to 27.2^{o}C as the heat rejection decreases. The total cooling duration (including pre-cooling) lasts for approximately 25 minutes. The total energy consumption for this option is equal to 18.38 MJ for the 14 molds. This is significantly lower than the energy consumed in the previous options (25.2 MJ for Options 1 and 2) because the pre-heating avoids heat input from the furnace during the initial 5 minutes of the heating process.

Finally, the temperatures for Option 4 (jacket-heating with pre-heat/recuperation coupled to closed-loop water) are shown in Figure 6.14. The range of temperature variation for the recuperation HTF is from 146.5^{o}C to 166^{o}C. Hot water is available at a temperature of 53^{o}C for process needs. The total cooling duration (including the pre-cooling phase) is approximately 28 minutes.

The overall comparison of these four options with the baseline and optimized processes is shown in Table 6.4. It is observed that the heating duration is longer in the jacket heating than in the baseline process. This is because the jacket heating lasts until the entire plastic inventory melts, whereas, at the completion of the heating cycle in the baseline process, 0.226 kg (16% of the original mass) of the plastic remains in the powder form. At a representative time 5 minutes into the heating process, the temperature difference (ΔT) between the furnace and the molds is 214.2^{o}C for the baseline process and 36.7^{o}C between the HTF and the molds for jacket heating (with no recuperation). At the same time, the heat transfer coefficients (h) are 35.53 (h_{rad}+h_{conv})

W/m^2-K for the baseline process and 171.0 W/m^2-K for the HTF-to-mold heat transfer. Also, the heat transfer surface areas (A) are 0.218 and 0.279 m^2 respectively for these two cases. Thus, the rates of energy transfer to the plastic are 523.9 and 593.2 W for the baseline and the jacket heating process respectively. Thus, the improved heat transfer coefficient in the jacket heating case more than compensates for the lower ΔT compared to the furnace heating case. Also, the thermal energy consumed in the jacket-heated configurations is significantly lower than the energy consumption in the original case. This is because a significant fraction of the energy, which was consumed by the auxiliary housing, is avoided in jacket heating, as the thermal energy from the HTF is directly transferred to the molds.

Table 6.4: Overall Comparison of Various Options

	Original Process	**Optimized Process**	**Jacket Option 1**	**Jacket Option 2**	**Jacket Option 3**	**Jacket Option 4**
Total Heat Input, MJ	79.54	72.58	25.20	25.20	18.38	18.38
Auxiliary Mass Heat Input, MJ	58.07	53.98	-	-	-	-
Fuel Consumption, m^3	3.42	3.12	1.08	1.08	0.79	0.79
Heating Time, min	17	14	18	18	18	18
Cooling Time, min	46	47	21	26	25	28
Hot Water Available	-	-	-	200 kg @ 56°C	-	150 kg @ 53°C

The energy consumption for jacket heating with heat recuperation is lowest among all the options considered. In this case, a portion of the thermal energy expended during cooling is used to pre-heat the HTF in the main loop, thus resulting in lower external energy for heating.

Finally, the cooling duration for the alternative scheme (jacket cooling) is lower than the original configuration. This is because the heat transfer coefficients are much higher in the former. At a representative time 3 minutes into the cooling process, the rate

of energy transfer *to* the plastic is 90.53 W for the baseline process (because the mold is still at a higher temperature than the plastic at the early portion of the cooling process) and 764.97 W *from* the plastic for jacket cooling with no recuperation (because of the much better cooling mechanism in this case). Also, the cooling time is lower in the case of an open loop compared to the cooling time for a closed loop. This is because the open-loop water provides a higher heat transfer rate than the closed loop. The energy and fuel consumptions for these various configurations corresponding to Table 6.4 are shown in Figures 6.15 and 6.16 respectively.

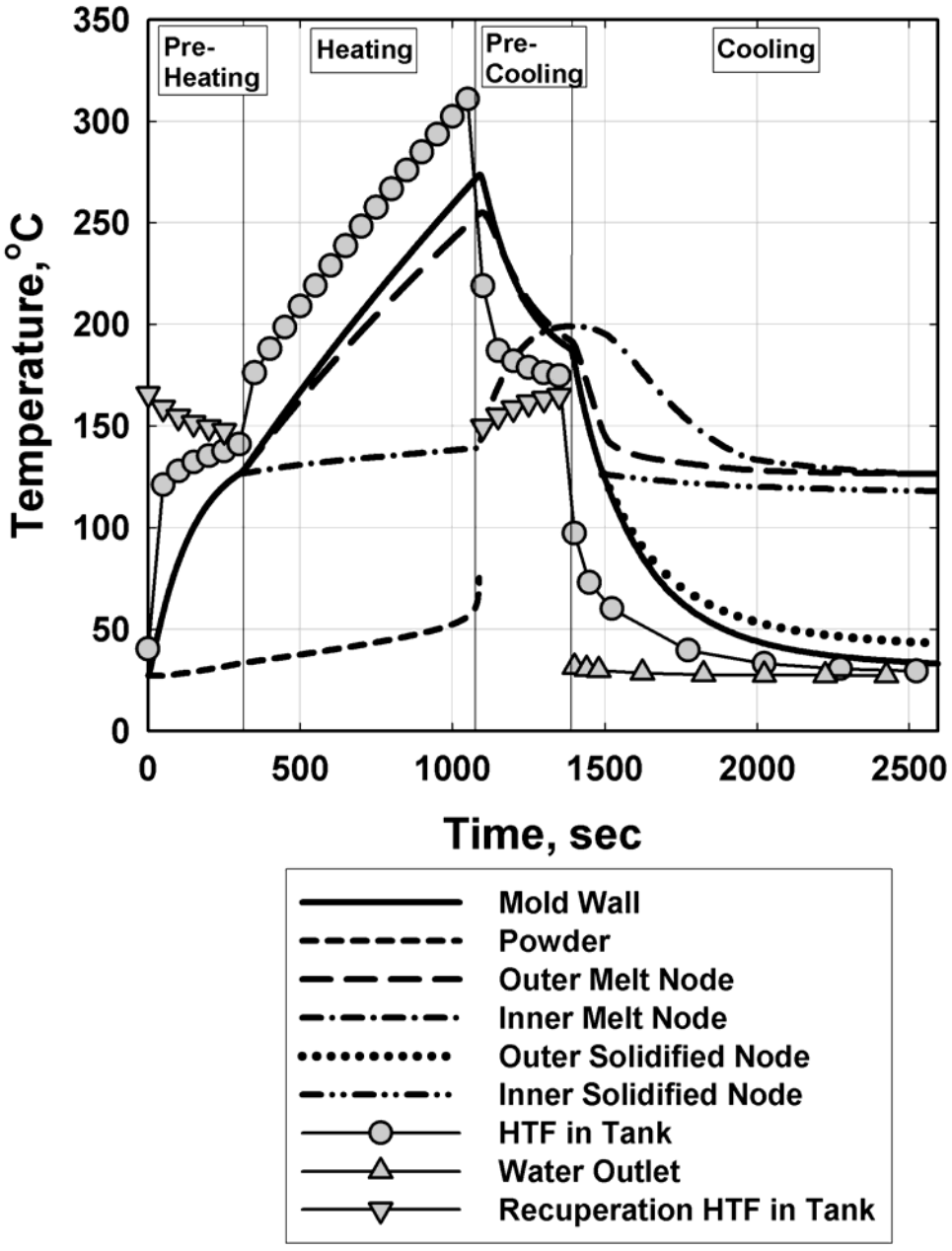

Figure 6.13: Temperature Profile for Jacket Heating with Pre-Heat/Recuperation and Open-Loop Water Cooling

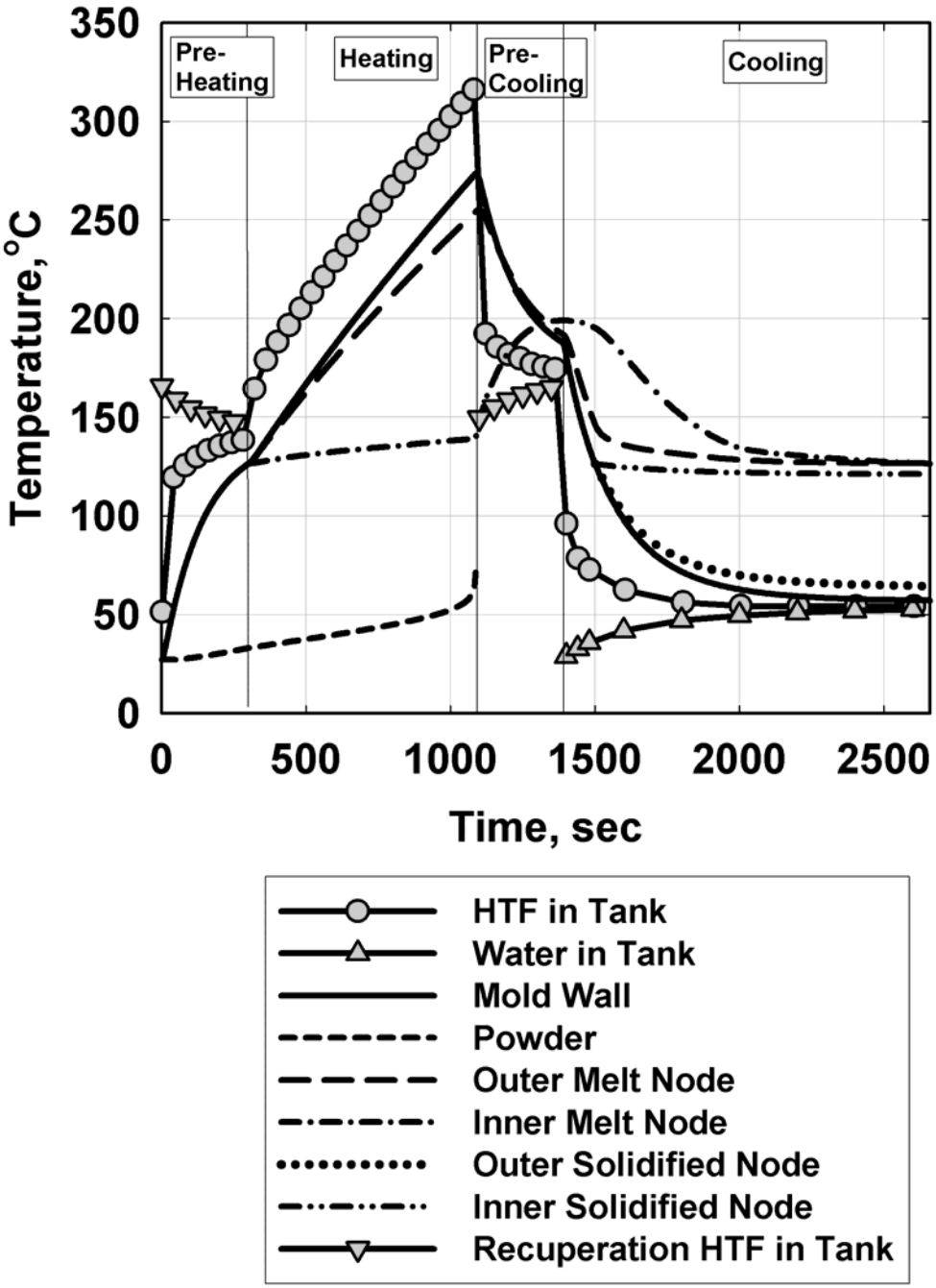

Figure 6.14: Temperature Profile for Jacket Heating with Pre-Heat/Recuperation and Closed-Loop Water Cooling

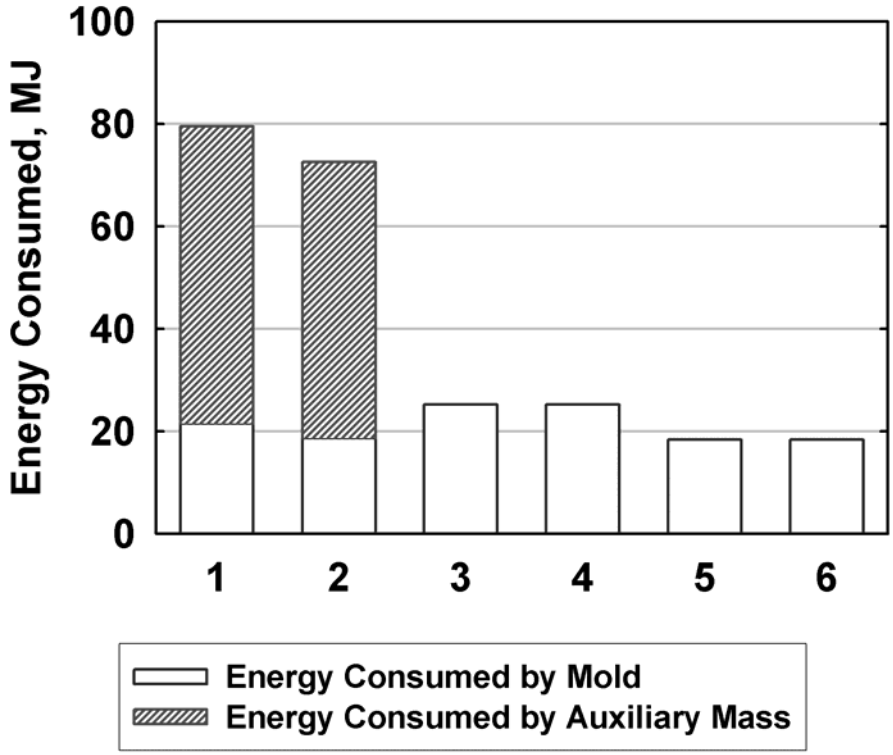

1	Original Molding Process
2	Optimized Molding Process
3	Jacket Heating and Cooling with Open-Loop Water
4	Jacket Heating and Cooling with Water Storage
5	Jacket Heating and Cooling with Heat Recuperation and Open-Loop Water
6	Jacket Heating and Cooling with Heat Recuperation and Water Storage

Figure 6.15: Energy Consumption for Various Configurations

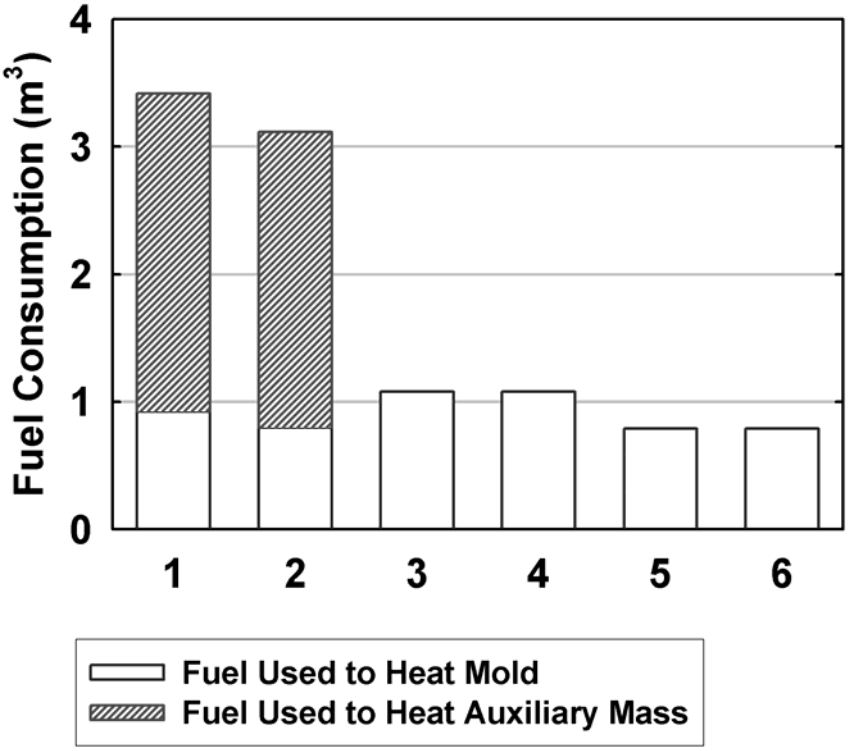

1	Original Molding Process
2	Optimized Molding Process
3	Jacket Heating and Cooling with Open-Loop Water
4	Jacket Heating and Cooling with Water Storage
5	Jacket Heating and Cooling with Heat Recuperation and Open-Loop Water
6	Jacket Heating and Cooling with Heat Recuperation and Water Storage

Figure 6.16: Fuel Consumption for Various Configurations

The variation of the heating and the cooling durations for the different process options considered in this study are shown in Figure 6.17. For the baseline and the optimized processes, the combinations of the heating and the cooling durations are 17 + 46 and 14 + 47 minutes, respectively. In both these cases, the melting of the plastic powder continues into the cooling stage. For the jacket heating options, the heating durations (18 minutes) are slightly longer because heating is continued until the entire plastic inventory is melted. The cooling durations for the jacket options are significantly lower because the higher heat transfer coefficient provided by the HTF flowing through the channels results in faster cooling. Also, it is observed that the cooling durations (21 and 25 minutes) are lower for the open-loop cooling options (Options 1 and 3) than the closed-loop cooling options (26 minutes for Option 2 and 28 minutes for Option 4). This is because open-loop cooling provides a higher temperature difference at the inlet than the closed-loop option, in which the water storage tank temperature rises as the process proceeds, reducing the effectiveness of the heat sink with time. The cooling durations in the recuperative heating and cooling options are longer than the durations for the options without recuperation because of the decreasing efficacy of the recuperative fluid as time progresses.

The total energy consumption for the baseline process is 79.5 MJ (0.75 therm) per batch. For the optimized process, this reduces to 72.6 MJ (0.69 therm) per batch. The commercial molding plant processes 12 cycles per day. Assuming 22 working days per month, the monthly energy consumption for the baseline and the optimized processes is 2.10×10^4 MJ (199 therm) and 1.92×10^4 MJ (182 therm) respectively. Based on the local gas utility (Georgia Natural Gas) rate of \$0.869 per therm and a \$5.95 monthly service charge, the monthly costs for these processes are \$179 and \$164, respectively. Therefore, the annual savings accruing from the optimization of the baseline process is \$181, which is not a very significant reduction in operating costs.

The monthly energy consumption for the jacket heating option without recuperation is 6.65×10^3 MJ (63 therm) for a monthly cost of \$61. For the jacket heating option with recuperation, the monthly energy consumption is 4.85×10^3 MJ (46 therm), resulting in a cost of \$46. Therefore, the estimated annual savings of \$1418 and \$1596

can be obtained from these two heating options over the baseline process. These fuel cost savings are summarized in Table 6.5.

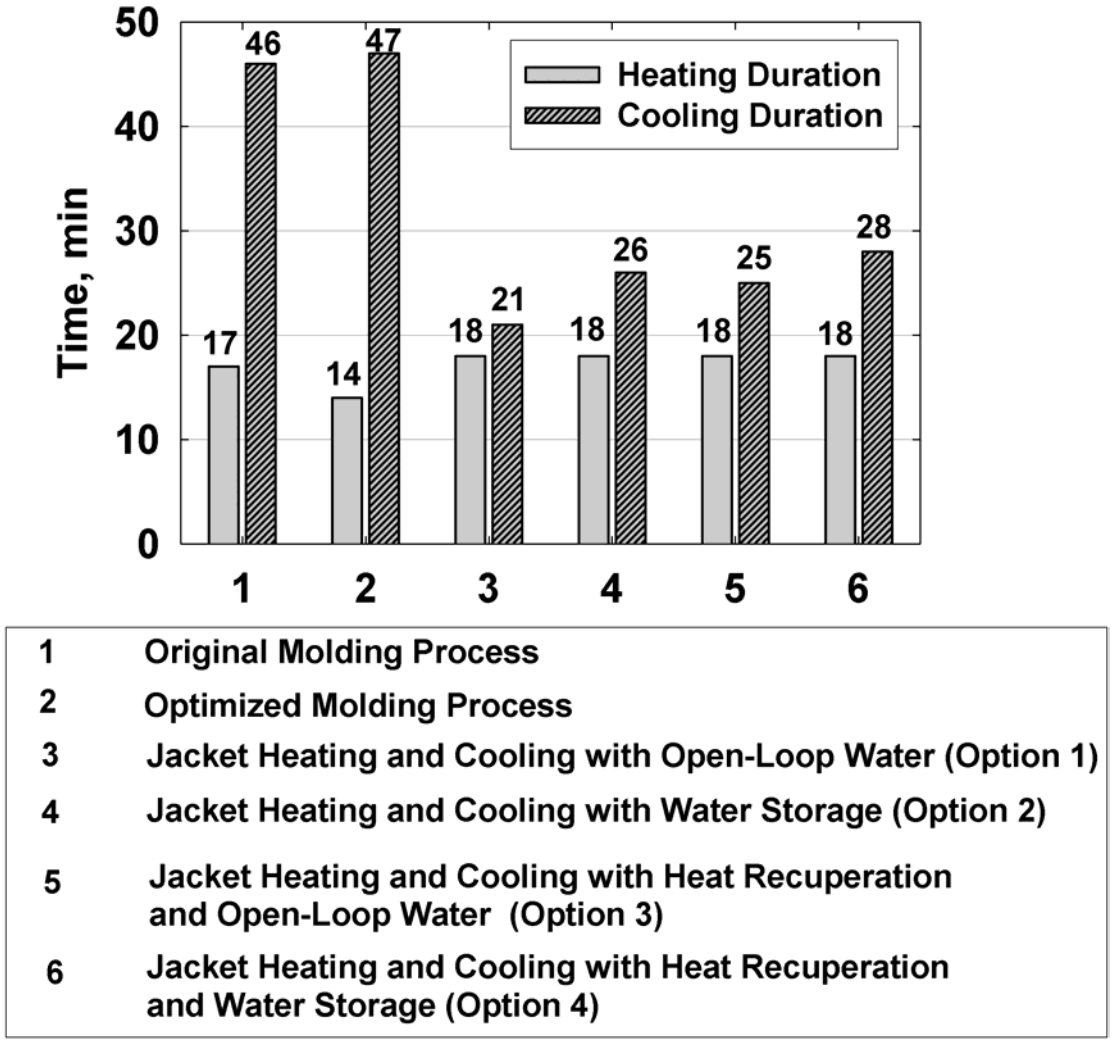

Figure 6.17: Variation of Heating and Cooling Durations for Various Jacket Heating and Cooling Combinations

Table 6.5: Heating Costs for the Various Configurations

	Baseline Molding Process	Optimized Molding Process	Jacket Heating *without* Recuperation	Jacket Heating *with* Recuperation
Annual Cost, $	2146	1965	729	550
Annual Savings over Baseline Molding Process, $	-	181	1418	1596

CHAPTER 7

CONCLUSIONS AND RECOMMENDATIONS

7.1: Conclusions

A detailed numerical analysis of the rotational molding process for LLDPE was conducted in this study. Particular attention was given to the transient temperature profiles within the melt and solid regions. Energy flows into and out of the mold during the heating and cooling phases were modeled through the entire molding duration. The model predicted the sensible heating of the powder, the movement of the phase-change front toward the core of the mold, the superheating of the liquid melt, and the subsequent solidification and subcooling of the plastic. In addition, the influence of the variation of heating and cooling durations on avoidable superheating of the melt and the excessive subcooling of the solid phase was documented. Parametric analyses with respect to heating and cooling durations revealed opportunities for the optimization of the molding process. The results of the study can be used to improve the energy efficiency of the molding process, and also to implement waste heat recovery systems to better utilize the heat removed during the cooling phases.

The model is further extended to compute the natural gas consumption for the molding process through the incorporation of a simple combustion module. The thermal masses of the auxiliary support structure required for rotational molding are computed and the energy consumed for heating and cooling of these structures included in the energy consumption estimates. This analysis showed that a significant portion (73%) of the energy supplied is consumed in heating the auxiliary mass. Finally, a detailed analysis of an alternate heating and cooling mechanism using jackets with and without recuperation and thermal storage is performed and energy estimates for the various options compared.

7.2: Recommendations

The present study represents a preliminary analysis of energy consumption in rotational molding using a simple, representative mold geometry. Models for molds of other shapes and sizes can be developed by making simple changes to the geometry inputs. Further, the results from these analyses may be scaled to estimate the time and energy savings in an overall molding plant. It is recommended that an experimental setup be developed to validate these preliminary results and to investigate the actual energy savings through the implementation of the alternative jacket heating and cooling system.

For the baseline process the introduction of a chilled water mist during the pre- and post-cooling phases should be investigated. The benefits of this modification in the form of faster cooling rates should be weighed against the increased capital cost.

In addition, in the present analysis, sizes of the recuperative heat exchangers, storage tanks, and fluid flow rates have been chosen somewhat arbitrarily for the purpose of illustrating the advantages of jacket heating and cooling. These sizes should be optimized through detailed parametric analyses that include consideration of the mix of the different parts being molded and the throughput across the entire plant.

APPENDIX A

Table A.1: Geometry Calculations

Variable	Formulation	Values
Dimensions	$l_i = (l_o - 2t_{wall})$	0.288 m
	$w_i = (w_o - 2t_{wall})$	0.168 m
	$h_i = (h_o - 2t_{wall})$	0.078 m
Volumes	$vol_{mold} = (l_o \cdot w_o \cdot h_o - l_i \cdot w_i \cdot h_i)$	0.0021 m^3
	$vol_i = l_i \cdot w_i \cdot h_i$	0.0040 m^3
Masses	$m_{mold} = \rho_{mold} vol_{mold}$	5.718 kg
Surface Areas	$A_{o,mold} = 2(w_o \cdot h_o + l_o \cdot h_o + w_o \cdot l_o)$	0.218 m^2
	$A_{i,mold} = 2(w_i \cdot h_i + l_i \cdot h_i + w_i \cdot l_i)$	0.168 m^2
	$A_{mold} = (A_{o,mold} + A_{i,mold})/2$	0.193 m^2

Table A.2: Summary of Heat Transfer Calculations for **Run 30** of Single-Phase Transient Heating

(2 minutes 25 seconds into Molding Process; Δt = 5 sec)

Input Variables		**Equations**	**Output Variables**	
Temperatures		$Q_{rad} = \varepsilon\sigma \cdot A_{o,mold} \cdot \left(T_{furnace}^{\ 4} - T_1^{\ 4}\right)$	***Temperatures***	
Furnace	$T_{furnace}$ = 343.3°C	$Q_{conv} = h_{coeff,o} \cdot A_{o,mold} \cdot \left(T_{furnace} - T_1\right)$	Furnace	$T_{furnace}$ = 343.3°C
Mold	$T_{1,s}$ = 79.93°C	$\sum_{j=1}^{2} Q_j = \left[\frac{T_j - T_{j+1}}{t/\left(k_{mold} A_{mold}\right)}\right]$	Mold	$T_{1,f}$ = 81.68°C
	$T_{2,s}$ = 79.84°C			$T_{2,f}$ = 81.57°C
	$T_{3,s}$ = 79.78°C			$T_{3,f}$ = 81.52°C
Powder	$T_{p,s}$ = 28.22°C	$\sum_{j=1}^{3} Q_{St,j} = \left(\frac{m_{mold}}{3}\right) \cdot C_{p,mold} \cdot \left(\frac{T_{j,f} - T_{j,s}}{\Delta t}\right)$	Powder	$T_{p,f}$ = 28.31°C
Masses				
Powder	m_p = 1.361 kg	$\sum_{j=1}^{3} Q_{j-1} = Q_{St,j} + Q_j$	***Heat Transfer Coefficients***	
Mold	m_{mold} = 5.718 kg			
Heat Transfer Coefficients		$Q_p = h_{coeff,p} \cdot A_{i,mold} \cdot \left(T_3 - T_p\right)$	Outer surface of mold/air	$h_{coeff,o}$ = 7.94 W/m^2-K
Outer surface of mold/air	$h_{coeff,o}$ = 7.96 W/m^2-K	$Q_p = m_p \cdot C_{p,p} \cdot \left(\frac{T_{p,f} - T_{p,s}}{\Delta t}\right)$		
Powder	$h_{coeff,p}$ = 5 W/m^2-K		Powder	$h_{coeff,p}$ = 5 W/m^2-K

Table A.3: Summary of Heat Transfer Calculations for **Run 70** of Phase-Change Melting in Furnace

(10 minutes 35 seconds into Molding Process; Δt = 5 sec)

Inputs		**Equations**	**Outputs**	
Temperatures		$Q_{rad} = \varepsilon\sigma \cdot A_{o,mold} \cdot \left(T_{furnace}^{\ 4} - T_1^{\ 4}\right)$	***Temperatures***	
Furnace	$T_{furnace} = 343.3^oC$	$Q_{conv} = h_{coeff,o} \cdot A_{o,mold} \cdot \left(T_{furnace} - T_1\right)$	Furnace	$T_{furnace} = 343.3^oC$
Mold	$T_{1,s} = 181.75^oC$	$\sum_{j=1}^{2} Q_j = \left[\frac{T_j - T_{j+1}}{t/\left(k_{mold} A_{mold}\right)}\right]$	Mold	$T_{1,f} = 182.41^oC$
	$T_{2,s} = 181.65^oC$			$T_{2,f} = 182.32^oC$
	$T_{3,s} = 181.59^oC$			$T_{3,f} = 182.25^oC$
Melt	$T_{4,s} = 175.57^oC$	$\sum_{j=1}^{3} Q_{St,j} = \left(\frac{m_{mold}}{3}\right) \cdot C_{p,mold} \cdot \left(\frac{T_{j,f} - T_{j,s}}{\Delta t}\right)$	Melt	$T_{4,f} = 176.15^oC$
	$T_{5,s} = 164.27^oC$			$T_{5,f} = 164.71^oC$
	$T_{6,s} = 153.47^oC$	$\sum_{j=1}^{3} Q_{j-1} = Q_{St,j} + Q_j$		$T_{6,f} = 153.77^oC$
	$T_{7,s} = 143.00^oC$			$T_{7,f} = 143.17^oC$
	$T_{8,s} = 132.15^oC$	$Q_3 = \left[\frac{T_3 - T_4}{(t/2)/\left(k_{mold} A_{mold}\right) + \left(\delta_{seg}/2\right)/\left(k_{pl,4} A_{avg}\right)}\right]$		$T_{8,f} = 132.20^oC$
Powder	$T_{p,s} = 39.64^oC$	$\sum_{j=4}^{8} Q_{St,j} = mass_j \cdot C_{p,pl,j} \cdot \left(\frac{T_{j,f} - T_{j,s}}{\Delta t}\right)$	Powder	$T_{p,f} = 39.76^oC$
		$\sum_{j=4}^{7} Q_j = \left[\frac{T_j - T_{j+1}}{\left(\delta_{seg}/2\right)/\left(k_{pl,j} A_{avg}\right) + \left(\delta_{seg}/2\right)/\left(k_{pl,j+1} A_{avg}\right)}\right]$		

Table A.3 (continued): Summary of Heat Transfer Calculations for **Run 70** of Phase-Change Melting in Furnace (10 minutes 35 seconds into Molding Process; Δt = 5 sec)

Inputs		**Equations**	**Outputs**	
Heat Transfer Coefficients		$\sum_{j=4}^{7} Q_{j-1} = Q_{St,j} + Q_j$	***Heat Transfer Coefficients***	
Outer surface of mold/air	$h_{coeff,o}$ = 6.66 W/m^2-K	$Q_7 = Q_{St,8} + Q_{front}$	Outer surface of mold/air	$h_{coeff,o}$ = 6.65 W/m^2-K
Powder	$h_{coeff,p}$ = 5 W/m^2-K	$\sum_{j=4}^{8} mass_j = \left(\frac{mass_{melt,s} + mass_{melt,f}}{2} \right)$	Powder	$h_{coeff,p}$ = 5 W/m^2-K
Melt Specifications		$Q_{front} = Q_{phasechange} + Q_p$	***Melt Specifications***	
Mass of melt formed	$mass_{melt,s}$ = 0.569 kg	$Q_{front} = \frac{k_{pl,8} \cdot A_{avg} \cdot (T_8 - T_{Melt})}{(\delta_{seg} / 2)}$	Mass of melt formed	$mass_{melt,f}$ = 0.577 kg
Thickness of melt formed	$\delta_{pl,s}$ = 4.24 mm	$Q_{phasechange} = [h_{fusion} + C_{p,p} \cdot (T_{Melt} - T_p)] \cdot \frac{\Delta mass}{\Delta t}$ $Q_p = h_{coeff,p} \cdot A_{melt/powder} \cdot (T_{Melt} - T_p)$	Thickness of melt formed	$\delta_{pl,f}$ = 4.31 mm
Heat of fusion	h_{fusion} = 133200 J/kg	$Q_p = mass_p \cdot C_{p,p} \cdot \left(\frac{T_{p,f} - T_{p,s}}{\Delta t} \right)$	Heat of fusion	h_{fusion} = 133200 J/kg

Table A.4: Summary of Heat Transfer Calculations for **Run 20** of Phase-Change Melting in Free-Convection (18 minutes 35 seconds into Molding Process; Δt = 5 sec)

Inputs		**Equations**	**Outputs**	
Temperatures		$Q_{rad} = \varepsilon\sigma \cdot A_{o,mold} \cdot \left(T_{amb}^{\ 4} - T_1^{\ 4}\right)$	***Temperatures***	
Ambient	$T_{amb} = 27.00^oC$	$Q_{conv} = h_{coeff,o} \cdot A_{o,mold} \cdot \left(T_{amb} - T_1\right)$	Ambient	$T_{amb} = 27.00^oC$
Mold	$T_{1,s} = 206.51^oC$	$\sum_{j=1}^{2} Q_j = \left[\frac{T_j - T_{j+1}}{t/\left(k_{mold} A_{mold}\right)}\right]$	Mold	$T_{1,f} = 205.61^oC$
	$T_{2,s} = 206.52^oC$			$T_{2,f} = 205.66^oC$
	$T_{3,s} = 206.54^oC$	$\sum_{j=1}^{3} Q_{St,j} = \left(\frac{m_{mold}}{3}\right) \cdot C_{p,mold} \cdot \left(\frac{T_{j,f} - T_{j,s}}{\Delta t}\right)$		$T_{3,f} = 205.67^oC$
Melt	$T_{4,s} = 202.11^oC$	$\sum_{j=1}^{3} Q_{j-1} = Q_{St,j} + Q_j$	Melt	$T_{4,f} = 201.38^oC$
	$T_{5,s} = 188.43^oC$			$T_{5,f} = 187.98^oC$
	$T_{6,s} = 171.97^oC$	$Q_3 = \left[\frac{T_3 - T_4}{(t/2)/\left(k_{mold} A_{mold}\right) + \left(\delta_{seg}/2\right)/\left(k_{pl,4} A_{avg}\right)}\right]$		$T_{6,f} = 171.73^oC$
	$T_{7,s} = 154.14^oC$			$T_{7,f} = 154.04^oC$
	$T_{8,s} = 135.76^oC$	$\sum_{j=4}^{8} Q_{St,j} = mass_j \cdot C_{p,pl,j} \cdot \left(\frac{T_{j,f} - T_{j,s}}{\Delta t}\right)$		$T_{8,f} = 135.73^oC$
Powder	$T_{p,s} = 55.45^oC$	$\sum_{j=4}^{7} Q_j = \left[\frac{T_j - T_{j+1}}{\left(\delta_{seg}/2\right)/\left(k_{pl,j} A_{avg}\right) + \left(\delta_{seg}/2\right)/\left(k_{pl,j+1} A_{avg}\right)}\right]$	Powder	$T_{p,f} = 55.78^oC$

Table A.4 (continued): Summary of Heat Transfer Calculation for **Run 20** of Phase-Change Melting in Free-Convection (18 minutes 35 seconds into Molding Process; Δt = 5 sec)

Inputs		**Equations**	**Outputs**	
Heat Transfer Coefficients		$\sum_{j=4}^{7} Q_{j-1} = Q_{St,j} + Q_j$	***Heat Transfer Coefficients***	
Outer surface of mold/air	$h_{coeff,o}$ = 7.87 W/m^2-K	$Q_7 = Q_{St,8} + Q_{front}$	Outer surface of mold/air	$h_{coeff,o}$ = 7.86 W/m^2-K
Powder	$h_{coeff,p}$ = 5 W/m^2-K	$\sum_{j=4}^{8} mass_j = \left(\frac{mass_{melt,s} + mass_{melt,f}}{2} \right)$	Powder	$h_{coeff,p}$ = 5 W/m^2-K
Melt Specifications		$Q_{front} = Q_{phasechange} + Q_p$	***Melt Specifications***	
Mass of melt formed	$mass_{melt,s}$ = 1.251 kg	$Q_{front} = \frac{k_{pl,8} \cdot A_{avg} \cdot (T_8 - T_{Melt})}{(\delta_{seg} / 2)}$	Mass of melt formed	$mass_{melt,f}$ = 1.257 kg
Thickness of melt formed	$\delta_{pl,s}$ = 9.84 mm	$Q_{phasechange} = \left[h_{fusion} + C_{p,p} \cdot (T_{Melt} - T_p) \right] \cdot \frac{\Delta mass}{\Delta t}$	Thickness of melt formed	$\delta_{pl,f}$ = 9.91 mm
Heat of fusion	h_{fusion} = 133200 J/kg	$Q_p = h_{coeff,p} \cdot A_{melt/powder} \cdot (T_{Melt} - T_p)$	Heat of fusion	h_{fusion} = 133200 J/kg
		$Q_p = mass_p \cdot C_{p,p} \cdot \left(\frac{T_{p,f} - T_{p,s}}{\Delta t} \right)$		

Table A.5: Summary of Heat Transfer Calculations for **Run 95** of Single-Phase Transient Cooling in Free-Convection (28 minutes into Molding Process; Δt = 5 sec)

Inputs		**Equations**	**Outputs**	
Temperatures		$Q_{rad} = \varepsilon\sigma \cdot A_{o,mold} \cdot \left(T_{amb}{}^4 - T_1{}^4\right)$	***Temperatures***	
Ambient	$T_{amb} = 27.00^oC$	$Q_{conv} = h_{coeff,o} \cdot A_{o,mold} \cdot \left(T_{amb} - T_1\right)$	Ambient	$T_{amb} = 27.00^oC$
Mold	$T_{1,s} = 148.47^oC$	$\sum_{j=1}^{2} Q_j = \left[\frac{T_j - T_{j+1}}{t/\left(k_{mold} A_{mold}\right)}\right]$	Mold	$T_{1,f} = 148.17^oC$
	$T_{2,s} = 148.49^oC$			$T_{2,f} = 148.20^oC$
	$T_{3,s} = 148.51^oC$			$T_{3,f} = 148.22^oC$
Melt	$T_{4,s} = 152.14^oC$	$\sum_{j=1}^{3} Q_{St,j} = \left(\frac{m_{mold}}{3}\right) \cdot C_{p,mold} \cdot \left(\frac{T_{j,f} - T_{j,s}}{\Delta t}\right)$	Melt	$T_{4,f} = 151.86^oC$
	$T_{5,s} = 157.14^oC$	$\sum_{j=1}^{3} Q_{j-1} = Q_{St,j} + Q_j$		$T_{5,f} = 156.91^oC$
	$T_{6,s} = 160.38^oC$			$T_{6,f} = 160.19^oC$
	$T_{7,s} = 162.27^oC$	$Q_3 = \left[\frac{T_3 - T_4}{(t/2)/\left(k_{mold} A_{mold}\right) + \left(\delta_{seg}/2\right)/\left(k_{pl,4} A_{avg}\right)}\right]$		$T_{7,f} = 162.12^oC$
	$T_{8,s} = 163.13^oC$			$T_{8,f} = 162.99^oC$
Powder	No powder	$\sum_{j=4}^{8} Q_{St,j} = mass_j \cdot C_{p,pl,j} \cdot \left(\frac{T_{j,f} - T_{j,s}}{\Delta t}\right)$	Powder	No powder

Table A.5 (continued): Summary of Heat Transfer Calculation for **Run 95** of Single-Phase Transient Cooling in Free-Convection (28 minutes into Molding Process; Δt = 5 sec)

Inputs		**Equations**	**Outputs**	
Heat Transfer Coefficients			***Heat Transfer Coefficients***	
Outer surface of mold/air	$h_{coeff,o}$ = 7.29 W/m^2-K	$\sum_{j=4}^{7} Q_j = \left[\frac{T_j - T_{j+1}}{(\delta_{seg}/2)/(k_{pl,j}A_{avg}) + (\delta_{seg}/2)/(k_{pl,j+1}A_{avg})} \right]$	Outer surface of mold/air	$h_{coeff,o}$ = 7.29 W/m^2-K
Powder	No powder		Powder	No powder
Melt Specifications		$\sum_{j=4}^{7} Q_{j-1} = Q_{St,j} + Q_j$	***Melt Specifications***	
Mass of melt formed	$mass_{pl,s}$ = 1.361 kg	$Q_7 = Q_{St,8}$	Mass of melt formed	$\delta_{pl,s}$ = 1.361 kg
Thickness of melt formed	$\delta_{pl,s}$ = 10.82 mm	$\sum_{j=4}^{8} mass_j = m_p$	Thickness of melt formed	$\delta_{pl,s}$ = 10.90 mm
Heat of fusion	h_{fusion} = 133200 J/kg		Heat of fusion	h_{fusion} = 133200 J/kg

Table A.6: Summary of Heat Transfer Calculations for **Run 25** of Phase-Change Solidification in Free-Convection (37 minutes 55 seconds into Molding Process; Δt = 5 sec)

Inputs		**Equations**	**Outputs**	
Temperatures		$Q_{rad} = \varepsilon\sigma \cdot A_{o,mold} \cdot \left(T_{amb}{}^4 - T_1{}^4\right)$	***Temperatures***	
Ambient	$T_{amb} = 27.00^oC$	$Q_{conv} = h_{coeff,o} \cdot A_{o,mold} \cdot \left(T_{amb} - T_1\right)$	Ambient	$T_{amb} = 27.00^oC$
Mold	$T_{1,s} = 123.58^oC$	$\overset{2}{\underset{j=1}{Q_j}} = \left[\dfrac{T_j - T_{j+1}}{t/\left(k_{mold}A_{mold}\right)}\right]$	Mold	$T_{1,f} = 123.58^oC$
	$T_{2,s} = 123.60^oC$			$T_{2,f} = 123.60^oC$
	$T_{3,s} = 123.62^oC$	$\overset{3}{\underset{j=1}{Q_{St,j}}} = \left(\dfrac{m_{mold}}{3}\right) \cdot C_{p,mold} \cdot \left(\dfrac{T_{j,f} - T_{j,s}}{\Delta t}\right)$		$T_{3,f} = 123.62^oC$
Solidified-Melt	$T_{4,s} = 123.95^oC$		Solidified-Melt	$T_{4,f} = 123.83^oC$
	$T_{5,s} = 124.56^oC$	$\overset{3}{\underset{j=1}{Q_{j-1}}} = Q_{St,j} + Q_j$		$T_{5,f} = 124.48^oC$
	$T_{6,s} = 125.14^oC$			$T_{6,f} = 125.09^oC$
	$T_{7,s} = 125.70^oC$	$Q_3 = \left[\dfrac{T_3 - T_4}{\left(t/2\right)/\left(k_{mold}A_{mold}\right) + \left(sol_{seg}/2\right)/\left(k_{pl,4}A_{avg,sol}\right)}\right]$		$T_{7,f} = 125.67^oC$
	$T_{8,s} = 126.24^oC$			$T_{8,f} = 126.23^oC$
Melt	$T_{9,s} = 129.62^oC$		Melt	$T_{9,f} = 129.58^oC$
	$T_{10,s} = 133.84^oC$	$\overset{13}{\underset{j=4}{Q_{St,j}}} = mass_j \cdot C_{p,pl,j} \cdot \left(\dfrac{T_{j,f} - T_{j,s}}{\Delta t}\right)$		$T_{10,f} = 133.75^oC$
	$T_{11,s} = 136.91^oC$			$T_{11,f} = 136.77^oC$
	$T_{12,s} = 139.00^oC$	$\overset{7}{\underset{j=4}{Q_{j-1}}} = Q_{St,j} + Q_j$		$T_{12,f} = 138.84^oC$
	$T_{13,s} = 140.07^oC$			$T_{13,f} = 139.89^oC$
Powder	No powder	$\overset{12}{\underset{j=9}{Q_{j-1}}} = Q_{St,j} + Q_j$	Powder	No powder

Table A.6 (continued): Summary of Heat Transfer Calculation for **Run 25** of Phase-Change Solidification in Free-Convection (37 minutes 55 seconds into Molding Process; Δt = 5 sec)

Inputs		**Equations**	**Outputs**	
Heat Transfer Coefficients		$\sum_{j=4}^{7} Q_j = \left[\frac{T_j - T_{j+1}}{(sol_{seg}/2)/(k_{pl,j} A_{avg,sol}) + (sol_{seg}/2)/(k_{pl,j+1} A_{avg,sol})} \right]$	***Heat Transfer Coefficients***	
Outer surface of mold/air	$h_{coeff,o}$ = 6.95 W/m^2-K	$Q_7 = Q_{St,8} + Q_{front}$	Outer surface of mold/air	$h_{coeff,o}$ = 6.94 W/m^2-K
Powder	No powder	$Q_{front} = \left[\frac{T_8 - T_{Melt}}{(sol_{seg}/2)/(k_{pl,8} A_{avg,sol})} \right]$	Powder	No powder
Melt Specifications		$\sum_{j=4}^{8} mass_j = \left(\frac{mass_{sol,s} + mass_{sol,f}}{2} \right)$	***Melt Specifications***	
Mass of solidified melt formed	$mass_{sol,s}$ = 0.067 kg	$Q_{front} = Q_{phasechange} + Q_8$	Mass of solidified-melt formed	$mass_{sol,f}$ = 0.070 kg
Thickness of solidified-melt formed	sol_s = 0.458 mm	$Q_{phasechange} = -h_{fusion} \cdot \left(\frac{mass_{sol,f} - mass_{sol,s}}{\Delta t} \right)$	Thickness of solidified-melt formed	sol_s = 0.479 mm
Heat of fusion	h_{fusion} = 133200 J/kg	$Q_8 = \left[\frac{T_{Melt} - T_9}{(\delta_{seg}/2)/(k_{pl,9} A_{avg})} \right]$	Heat of fusion	h_{fusion} = 133200 J/kg
		$\sum_{j=9}^{12} Q_j = \left[\frac{T_j - T_{j+1}}{(\delta_{seg}/2)/(k_{pl,j} A_{avg}) + (\delta_{seg}/2)/(k_{pl,j+1} A_{avg})} \right]$		
		$Q_{12} = Q_{St,13}$		
		$\sum_{j=4}^{13} mass_j = m_p$		

Table A.7: Summary of Heat Transfer Calculations for **Run 140** of Phase-Change Solidification in Forced-Convection (51 minutes 35 seconds into Molding Process; Δt = 5 sec)

Inputs		**Equations**	**Outputs**	
Temperatures		$Q_{rad} = \varepsilon\sigma \cdot A_{o,mold} \cdot \left(T_{amb}{}^4 - T_1{}^4\right)$	***Temperatures***	
Ambient	$T_{amb} = 27.00^oC$	$Q_{conv} = h_{coeff,o} \cdot A_{o,mold} \cdot \left(T_{amb} - T_1\right)$	Ambient	$T_{amb} = 27.00^oC$
Mold	$T_{1,s} = 84.59^oC$	$\overset{2}{\underset{j=1}{Q_j}} = \left[\frac{T_j - T_{j+1}}{t/\left(k_{mold} A_{mold}\right)}\right]$	Mold	$T_{1,f} = 84.41^oC$
	$T_{2,s} = 84.61^oC$			$T_{2,f} = 84.43^oC$
	$T_{3,s} = 84.63^oC$	$\overset{3}{\underset{j=1}{Q_{St,j}}} = \left(\frac{m_{mold}}{3}\right) \cdot C_{p,mold} \cdot \left(\frac{T_{j,f} - T_{j,s}}{\Delta t}\right)$		$T_{3,f} = 84.45^oC$
Solidified-Melt	$T_{4,s} = 90.05^oC$		Solidified-Melt	$T_{4,f} = 89.88^oC$
	$T_{5,s} = 99.98^oC$	$\overset{3}{\underset{j=1}{Q_{j-1}}} = Q_{St,j} + Q_j$		$T_{5,f} = 99.86^oC$
	$T_{6,s} = 109.14^oC$			$T_{6,f} = 109.05^oC$
	$T_{7,s} = 117.67^oC$	$Q_3 = \left[\frac{T_3 - T_4}{(t/2)/\left(k_{mold} A_{mold}\right) + \left(sol_{seg}/2\right)/\left(k_{pl,4} A_{avg,sol}\right)}\right]$		$T_{7,f} = 117.62^oC$
	$T_{8,s} = 124.13^oC$			$T_{8,f} = 124.12^oC$
Melt	$T_{9,s} = 127.07^oC$	$\overset{13}{\underset{j=4}{Q_{St,j}}} = mass_j \cdot C_{p,pl,j} \cdot \left(\frac{T_{j,f} - T_{j,s}}{\Delta t}\right)$	Melt	$T_{9,f} = 127.06^oC$
	$T_{10,s} = 128.09^oC$			$T_{10,f} = 128.07^oC$
	$T_{11,s} = 128.85^oC$	$\overset{7}{\underset{j=4}{Q_{j-1}}} = Q_{St,j} + Q_j$		$T_{11,f} = 128.83^oC$
	$T_{12,s} = 129.35^oC$			$T_{12,f} = 129.33^oC$
	$T_{13,s} = 129.60^oC$	$\overset{12}{\underset{j=9}{Q_{j-1}}} = Q_{St,j} + Q_j$		$T_{13,f} = 129.57^oC$
Powder	No powder		Powder	No powder

Table A.7 (continued): Summary of Heat Transfer Calculation for **Run 140** of Phase-Change Solidification in Forced-Convection (51 minutes 35 seconds into Molding Process; Δt = 5 sec)

Inputs		**Equations**	**Outputs**	
Heat Transfer Coefficients		$\sum_{j=4}^{7} Q_j = \left[\frac{T_j - T_{j+1}}{(sol_{seg}/2)/(k_{pl,j}A_{avg,sol}) + (sol_{seg}/2)/(k_{pl,j+1}A_{avg,sol})} \right]$	***Heat Transfer Coefficients***	
Outer surface of mold/air	$h_{coeff,o}$ = 22.05 W/m^2-K	$Q_7 = Q_{St,8} + Q_{front}$	Outer surface of mold/air	$h_{coeff,o}$ = 22.06 W/m^2-K
Powder	No powder	$Q_{front} = \left[\frac{T_8 - T_{Melt}}{(sol_{seg}/2)/(k_{pl,8}A_{avg,sol})} \right]$	Powder	No powder
Melt Specifications		$\sum_{j=4}^{8} mass_j = \left(\frac{mass_{sol,s} + mass_{sol,f}}{2} \right)$	***Melt Specifications***	
Mass of solidified melt formed	$mass_{sol,s}$ = 0.699 kg	$Q_{front} = Q_{phasechange} + Q_8$	Mass of solidified-melt formed	$mass_{sol,f}$ = 0.703 kg
Thickness of solidified-melt formed	sol_s = 0.491 mm	$Q_{phasechange} = -h_{fusion} \cdot \left(\frac{mass_{sol,f} - mass_{sol,s}}{\Delta t} \right)$	Thickness of solidified-melt formed	sol_s = 0.494 mm
Heat of fusion	h_{fusion} = 133200 J/kg	$Q_8 = \left[\frac{T_{Melt} - T_9}{(\delta_{seg}/2)/(k_{pl,9}A_{avg})} \right]$	Heat of fusion	h_{fusion} = 133200 J/kg
		$\sum_{j=9}^{12} Q_j = \left[\frac{T_j - T_{j+1}}{(\delta_{seg}/2)/(k_{pl,j}A_{avg}) + (\delta_{seg}/2)/(k_{pl,j+1}A_{avg})} \right]$		
		$Q_{12} = Q_{St,13}$		
		$\sum_{j=4}^{13} mass_j = m_p$		

A.1: Estimation of Volume for Auxiliary Mass

The volume of tubes along the length ($l_{housing}$), as shown in Figure 5.2 and Figure A.1, is calculated as follows:

$$vol_l = l_{housing} \cdot \left(cross_{sec} \cdot cross_{sec} - \left(cross_{sec} - 2 \cdot thk\right) \cdot \left(cross_{sec} - 2 \cdot thk\right)\right) \cdot N_{tubes,l} \quad (A.1)$$

where $cross_{sec}$ (3.8 cm) is the outer dimension of the square tubes, thk (4 mm) denotes the tube thickness and $N_{tubes,l}$ (10) is the number of these tubes along the length (at the top and bottom) (Figure A.1). Similarly, along the width ($w_{housing}$), the volume of the tubes is given by the following:

$$vol_w = w_{housing} \cdot \left(cross_{sec} \cdot cross_{sec} - \left(cross_{sec} - 2 \cdot thk\right) \cdot \left(cross_{sec} - 2 \cdot thk\right)\right) \cdot N_{tubes,w} \quad (A.2)$$

where $N_{tubes,w}$ (12) denotes the number of these tubes along the width (at the top and bottom) (Figure A.1). The volume of the connector tubes (of approximate length $l_{housing}/5$) is given by the following:

$$vol_c = \left(l_{housing}/5\right) \cdot \left(cross_{sec} \cdot cross_{sec} - \left(cross_{sec} - 2 \cdot thk\right) \cdot \left(cross_{sec} - 2 \cdot thk\right)\right) \cdot N_{tubes,c} \quad (A.3)$$

where $N_{tubes,c}$ (4) denotes the number of these connector tubes (at the top and bottom). As shown in Figure A.1, the volume of the bottom plate is as follows:

$$vol_b = \left(l_{housing}/5\right) \cdot \left(w_{housing}/3\right) \cdot \left(cross_{sec}/2\right) \quad (A.4)$$

where the dimensions of the bottom plate are approximated as $l_{housing}/5 \times w_{housing}/3 \times cross_{sec}/2$. Also, the volume of square frames (estimated length $l_f = 0.25$ m) placed at the top and bottom of each mold is accounted for as follows:

$$vol_f = \left(l_f \cdot N_f\right) \cdot \left(cross_{sec} \cdot cross_{sec} - \left(cross_{sec} - 2 \cdot thk\right) \cdot \left(cross_{sec} - 2 \cdot thk\right)\right) \cdot N_{frames} \quad (A.5)$$

where N_f (4) is the number of tubes on each frame and N_{frames} (28) denote the number of frames. Additionally, the volume of various fittings such as bolts is calculated as follows:

$$vol_{fittings} = \left(\frac{\pi}{4} \cdot d_b^{\,2} \cdot h_b\right) \cdot N_b \quad (A.6)$$

where d_b (2 cm) is the estimated diameter, h_b is the length (5 cm), and N_b (40) are the number of these bolts. These calculations are summarized in Table A.8.

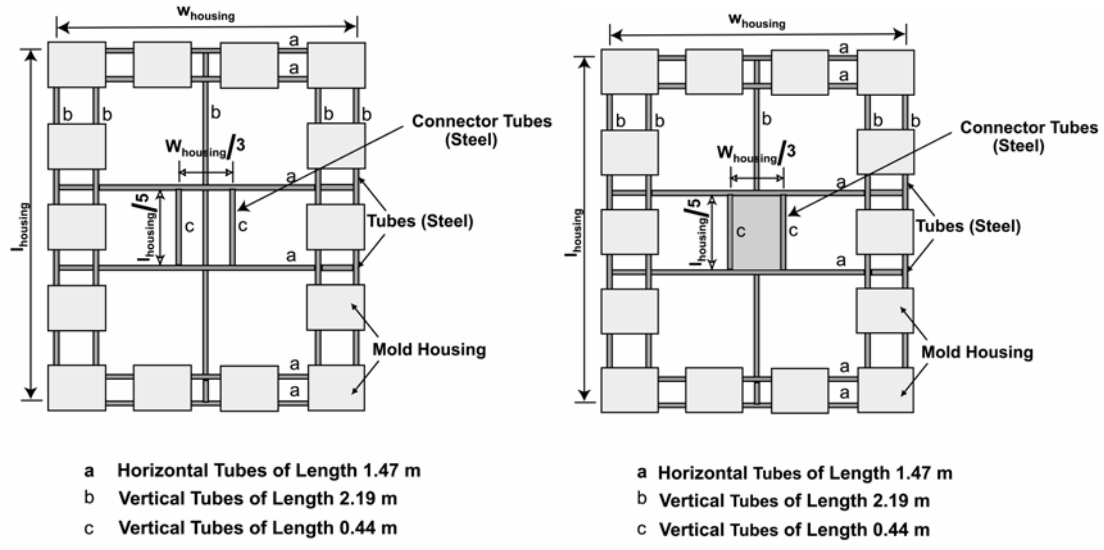

Figure A.1: Approximated Model of the Housing (Top and Bottom Views)

A.2: Estimation of Surface Area for Auxiliary Mass

The surface areas of the tubes along the length and width are respectively given by:

$$A_{s,l} = l_{housing} \cdot (4 \cdot cross_{sec}) \cdot N_{tubes,l} \quad (A.7)$$

$$A_{s,w} = w_{housing} \cdot (4 \cdot cross_{sec}) \cdot N_{tubes,w} \quad (A.8)$$

The surface areas of: i) connector tubes, ii) bottom plate, iii) square plates placed at the top and bottom of mold, and, iv) various connectors such as bolts are given by the following:

$$A_{s,c} = \left(l_{housing} / 5 \right) \cdot (4 \cdot cross_{sec}) \cdot N_{tubes,c} \quad (A.9)$$

$$A_{s,b} = \left(l_{housing} / 5 \right) \cdot \left(w_{housing} / 3 \right) \quad (A.10)$$

$$A_{s,f} = (l_f \cdot N_f) \cdot (4 \cdot cross_{sec}) \cdot N_{frames} \quad (A.11)$$

$$A_{s,fittings} = (\pi \cdot d_b \cdot h_b) \cdot N_b \quad (A.12)$$

These calculations are summarized in Table A.9.

Table A.8: Calculation of Individual Volumes of the Auxiliary Mass

Dimension	Inputs	Calculation of Volume	Calculated Value
Volume of steel tubes along the length	$N_{tubes,l} = 10$	$vol_l = l_{housing} \cdot (cross_{sec} \cdot cross_{sec} - (cross_{sec} - 2 \cdot thk) \cdot (cross_{sec} - 2 \cdot thk)) \cdot N_{tubes,l}$	0.014 m^3
Volume of steel tubes along the width	$N_{tubes,w} = 12$	$vol_w = w_{housing} \cdot (cross_{sec} \cdot cross_{sec} - (cross_{sec} - 2 \cdot thk) \cdot (cross_{sec} - 2 \cdot thk)) \cdot N_{tubes,w}$	0.011 m^3
Volume of steel connector tubes	$N_{tubes,c} = 4$	$vol_c = \left(l_{housing} / 5\right) \cdot (cross_{sec} \cdot cross_{sec} - (cross_{sec} - 2 \cdot thk) \cdot (cross_{sec} - 2 \cdot thk)) \cdot N_{tubes,c}$	0.001 m^3
Volume of bottom plate		$vol_b = \left(l_{housing} / 5\right) \cdot \left(w_{housing} / 3\right) \cdot \left(cross_{sec} / 2\right)$	0.004 m^3
Volume of square plates placed at the top and bottom	$N_{frames} = 28$	$vol_f = (l_f \cdot N_f) \cdot (cross_{sec} \cdot cross_{sec} - (cross_{sec} - 2 \cdot thk) \cdot (cross_{sec} - 2 \cdot thk)) \cdot N_{frames}$	0.018 m^3
Volume of various fittings (bolts)	$N_b = 40$	$vol_{fittings} = \left(\frac{\pi}{4} \cdot d_b^{\,2} \cdot h_b\right) \cdot N_b$	0.001 m^3
Total volume		$vol_{total} = vol_l + vol_w + vol_c + vol_b + vol_f + vol_{fittings}$	0.049 m^3

Table A.9: Calculation of Individual Surface Areas of the Auxiliary Mass

Dimension	Inputs	Calculation of Surface Areas	Calculated Value
Surface area of steel tubes along the length	$N_{tubes,l} = 10$	$A_{s,l} = l_{housing} \cdot (4 \cdot cross_{sec}) \cdot N_{tubes,l}$	3.348 m^2
Surface area of steel tubes along the width	$N_{tubes,w} = 12$	$A_{s,w} = w_{housing} \cdot (4 \cdot cross_{sec}) \cdot N_{tubes,w}$	2.694 m^2
Surface area of connector steel tubes	$N_{tubes,c} = 4$	$A_{s,c} = \left(l_{housing} / 5 \right) \cdot (4 \cdot cross_{sec}) \cdot N_{tubes,c}$	0.268 m^2
Surface area of bottom plate. (This is neglected)		$A_{s,b} = \left(l_{housing} / 5 \right) \cdot \left(w_{housing} / 3 \right)$	0.216 m^2
Surface area of square plates placed at the top and bottom of mold	$N_{frames} = 28$	$A_{s,f} = (l_f \cdot N_f) \cdot (4 \cdot cross_{sec}) \cdot N_{frames}$	4.267 m^2
Surface of various fittings (bolts). (This is neglected)	$N_b = 40$	$A_{s,fittings} = (\pi \cdot d_b \cdot h_b) \cdot N_b$	0.126 m^2
Total surface area		$A_{s,total} = A_{s,l} + A_{s,w} + A_{s,c} + A_{s,f}$	10.578 m^2

APPENDIX B

B.1: Flue Gas-to-HTF Heat Exchanger Design

The basic design of the flue gas-to-heat transfer fluid (HTF) crossflow heat exchanger made of steel is shown in Figure B.1. The cross-section of the tubes and geometrical details of the multi-louver fins are shown in Figure B.2. Flue gas flows though the multi-

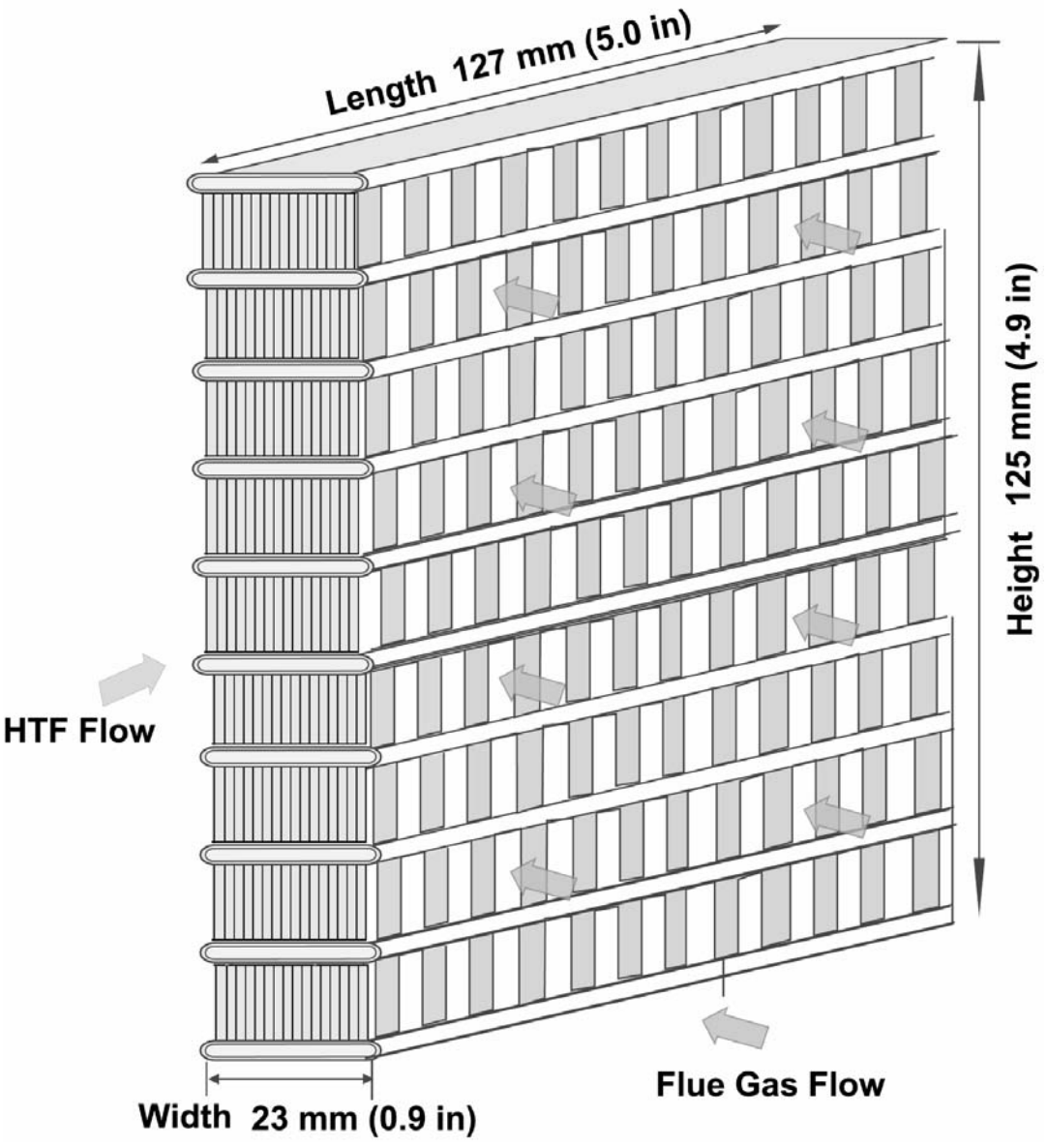

Figure B.1 Crossflow Heat Exchanger Design for the Flue Gas Heat Exchanger

louver fins, which provide a higher surface area for heat transfer (since air has a much lower heat transfer coefficient than the HTF), while the HTF flows through the bank of tubes. In addition, the louvers in the fins enhance the gas-side heat transfer coefficient. The HTF flows through the bank of 10 tubes in a parallel flow arrangement

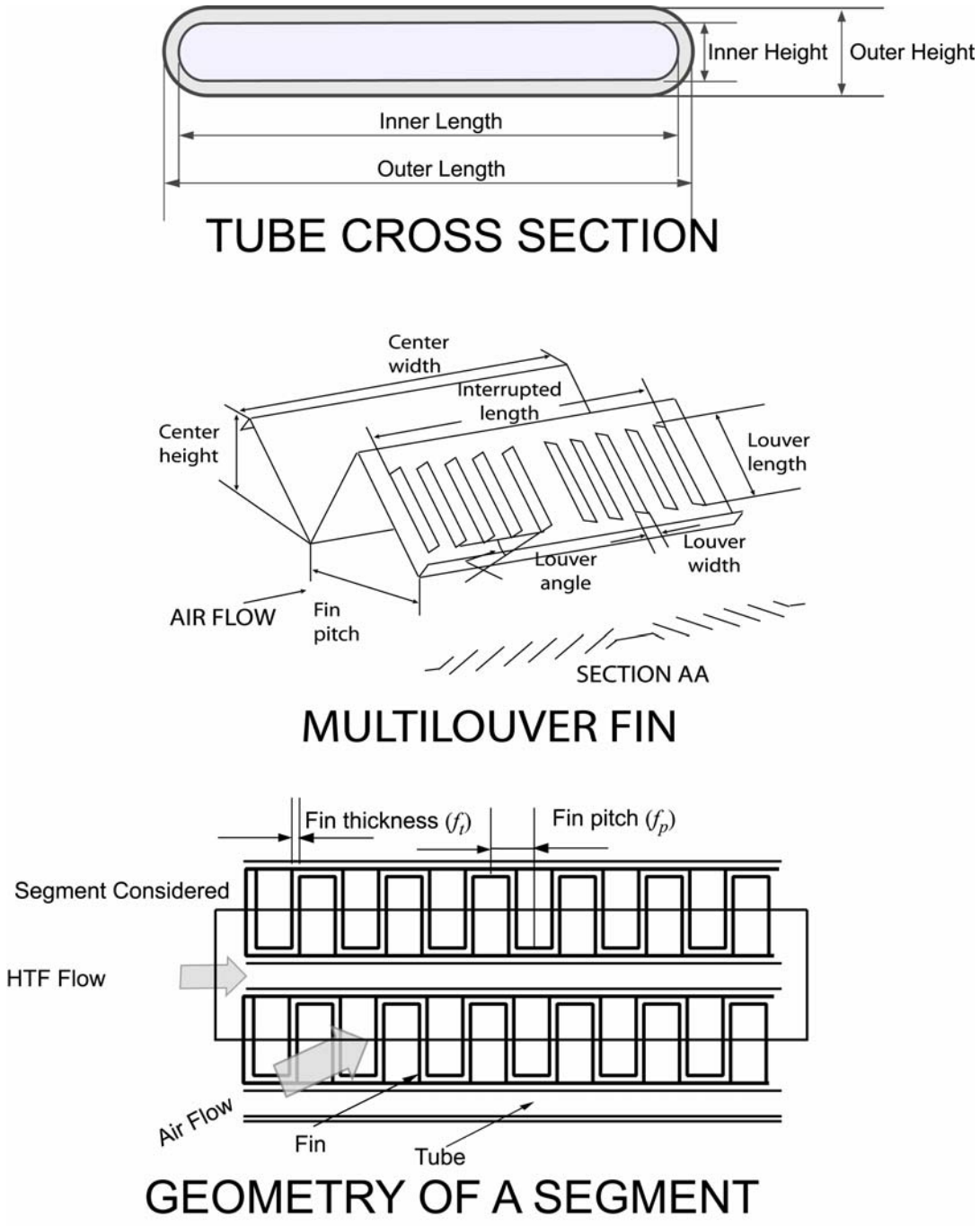

Figure B.2 Salient Features of the Flue Gas Heat Exchanger

Tube-Side Geometry

The tube-side geometry consists of a rectangular tube with semicircular ends as shown in Figure B.2. The various geometric parameters are shown in Table B.1. The total cross sectional area of the tube is given by Equation B.1, where $t_{h,i}$ and $t_{w,i}$ are the tube inner height and width respectively.

Table B.1: Dimensional Details of Crossflow Heat Exchanger

Tube side		**Fin**		**Louver**	
Pass Arrangement	One pass, 10 tubes	No. of fins per unit length	6 fins per cm (15 fins per inch)	Louver angle	30^o
Outer tube height	1.27 mm (0.05 in)	Fin height	10.2 mm (0.4 in)	Louver pitch	1.0 mm (0.039 in)
Outer tube depth	23 mm (0.9 in)	Fin thickness	0.11 mm (0.0045 in)	Louver length	9.1 mm (0.36 in)
Tube wall thickness	0.32 mm (0.0125 in)	Fin depth	23 mm (0.9 in)		
Tube length	127 mm (5.0 in)	Mass of fins	0.06 kg (0.13 lb)		
Heat Exchanger Height	125 mm (4.9 in)	Conductivity of Tube and Fin material	60.4 W/mK (34.89 Btu/hr-ft-F)		
Mass of tubes	0.14 kg (0.32 lb)				
Total mass	0.22 kg (0.46 lb)				

$$A_{tube} = N_t \left[t_{h,i} \cdot \left(t_{w,i} - t_{h,i} \right) + \frac{\pi}{4} \cdot {t_{h,i}}^2 \right] \tag{B.1}$$

The tube inner height and width being 0.63 mm and 22.4 mm respectively, the tube cross sectional area is 140 mm^2. The inner perimeter $perim_{tube}$ and the hydraulic diameter $D_{h,tube}$ are calculated using the following equations:

$$perim_{tube} = N_t \left[\pi \cdot t_{h,i} + 2 \cdot \left(t_{w,i} - t_{h,i} \right) \right] \tag{B.2}$$

$$D_{h,tube} = \frac{4 \cdot A_{tube}}{perim_{tube}} \tag{B.3}$$

The resulting perimeter and hydraulic diameter are 45.2 cm and 0.124 mm respectively. The tube-side heat transfer area (per tube per unit length) is given by the following:

$$A_{effect,tube} = N_t\left[2\cdot\left(t_{w,i} - t_{h,i}\right) + \pi\cdot t_{h,i}\right] \tag{B.4}$$

The tube-side effective heat transfer area for the entire length of all the tubes is 573.7 cm^2.

Air-Side Geometry

The total face area of the heat exchanger, A_c is given by the following equation:

$$A_c = \left(N_t\cdot t_{h,o} + N_c\cdot c_h\right)\cdot L_t \tag{B.5}$$

where N_t, N_c and c_h represents the number of tubes, number of centers (fins) and center height respectively, and L_t is the length of the tube per pass. The outer tube height and the center (fin) height are 1.27 mm and 10.2 mm respectively and the total face area is 158.1 cm^2. The flow area blocked by the fins and the free flow area can be calculated as follows:

$$A_{b,a} = \frac{L_t}{f_p}\cdot\left(c_h\cdot f_t + \left(f_p - f_t\right)\cdot f_t\right)\cdot N_c \tag{B.6}$$

$$A_{f,a} = A_c - \left(A_{b,a} + N_t\cdot t_{h,o}\cdot L_t\right) \tag{B.7}$$

where, f_p and f_t are the fin pitch and fin thickness respectively, as shown in Figure B.2. The fin pitch is 1.7 mm and the flow area blocked by the fins and free flow area are 11.1 cm^2 and 130.8 cm^2 respectively. The fin-side perimeter and hydraulic diameter are calculated as follows:

$$perim_{air} = 2\cdot N_c\cdot L_t\cdot\left[\left(\frac{c_h - f_t}{f_p}\right) + \left(1 - \frac{f_t}{f_p}\right)\right] + 2\cdot N_c\cdot c_h \tag{B.8}$$

$$D_{h,a} = \left(\frac{4\cdot A_{f,a}}{perim_{air}}\right) \tag{B.9}$$

The fin-side perimeter and hydraulic diameter are 19.4 m and 2.7 mm respectively. The number of fins per center is given by the following:

$$N_{fins} = \frac{L_t}{f_p} \tag{B.10}$$

There are 75 fins over the tube length for the present geometry. The air-side direct and indirect heat transfer areas per unit length are given by:

$$A_{d,air} = 2 \cdot \left(t_{w,o} - t_{h,o}\right) \cdot \left(1 - \frac{f_t}{f_p}\right) + \pi \cdot t_{h,o} \tag{B.11}$$

and

$$A_{id,air} = 2 \cdot c_w \cdot \left(\frac{c_h - f_t}{f_p}\right) \tag{B.12}$$

respectively. The air-side direct and indirect heat transfer area for the total length of the heat exchanger is 577.2 cm^2 and 3445 cm^2 respectively. Hence, the fin efficiency and the effective finned area are obtained as follows:

$$\eta_{f,air} = \frac{\tanh\left[\sqrt{\frac{2 \cdot h_a}{k_f \cdot f_t}} \cdot \frac{c_h}{2}\right]}{\sqrt{\frac{2 \cdot h_a}{k_f \cdot f_t}} \cdot \frac{c_h}{2}} \tag{B.13}$$

and

$$A_{effect,air} = A_{d,air} + \eta_{f,air} \cdot A_{id,air} \tag{B.14}$$

respectively, where k_f and f_t are the thermal conductivity and thickness of the fin, respectively. The fin material is mild steel with a thermal conductivity of 60.4 W/m-K. The fin efficiency and the effective finned area are 0.92 and 3728 cm^2.

Tube-Side Heat Transfer and Pressure Drop

The heat transfer fluid (Dowtherm RP) enters the furnace at a lower temperature and leaves at a higher temperature. In addition, these temperatures change as the heating and cooling phases of the molding cycle proceed. The physical properties of the heat transfer fluid change with temperature. Hence to predict the furnace performance accurately, the flow path was divided into 100 segments of equal length. The heat

transfer coefficients and pressure drop were calculated at each segment and the heat duties added across all the segments to obtain the overall performance of the furnace.

The applicable flow regime is determined using the transition criterion provided by Bhatti and Shah (1987). This criterion is based on the ratio of maximum and mean velocities in the duct given by Purday (1949) and Natarajan and Lakshmanan (1972). These in turn depend on the duct aspect ratio, which is a ratio of the tube height to the tube width. In the case of laminar flow, the tube-side Nusselt number is calculated by the expression for flow through rectangular ducts given by Bhatti and Shah (1987). The turbulent flow Nusselt number is computed using the expression developed by Churchill (1977a) for circular tubes. This Nusselt number expression depends on the friction factor, which is given by Churchill (1977b).

The pressure drop in the case of laminar flow is calculated using a correlation for the friction factor in rectangular ducts recommended by Shah and London (1978). In the case of turbulent flow, a correction factor in terms of the duct aspect ratio recommended by Bhatti and Shah (1987) is applied to the Churchill friction factor for circular tubes.

For a representative case where the heat transfer fluid inlet at 400^{o}F (204^{o}C) the tube-side velocity, heat transfer coefficient and pressure drop are 1.53 m/s, 7274 W/m^{2}K (1281 Btu/hr-ft^2-F) and the pressure drop to be 0.8 kPa (0.11 psi).

Air-Side Heat Transfer and Pressure Drop

The air-side heat transfer coefficient and pressure drop are calculated from the correlations for Stanton number and friction factor suggested by Sunden and Svantesson (1992):

$$St_a = 3.67 \cdot \mathrm{Re}_a^{-0.591} \cdot \left(\frac{f_p}{l_p}\right)^{0.0206} \cdot \left(\frac{c_h}{l_p}\right)^{-0.285} \cdot \left(\frac{l_p \sin\theta}{2 \cdot l_p}\right)^{0.0671} \cdot \left(\frac{c_w}{l_p}\right)^{-0.243} \qquad \text{(B.15)}$$

$$f_a = 9.2 \cdot \mathrm{Re}_a^{-0.54} \cdot \left(\frac{f_p}{l_p}\right)^{-0.022} \cdot \left(\frac{c_h}{l_p}\right)^{-1.085} \cdot \left(\frac{l_p \cdot \sin\theta}{2 \cdot l_p}\right)^{0.0671} \cdot \left(\frac{c_w}{l_p}\right)^{-0.31} \qquad \text{(B.16)}$$

It should be noted that the Reynolds number for these models is based on the louver pitch, and not the hydraulic diameter.

The flue gas inlet temperature is 1516^{o}C (2761^{o}F), which is the adiabatic flame temperature of the combustion products. The air face velocity and core velocity are 1.2 m/s and 1.6 m/s respectively. The air-side Reynolds number, Stanton number and friction factor are 9.7, 0.21 and 0.51 respectively. The air-side heat transfer coefficient is 111.2 W/m^{2}K (19.6 Btu/hr-ft^2-F) and the air-side pressure drop is 5.0 Pa (0.02 in H_2O).

Having calculated the tube-side and air-side heat transfer coefficients and pressure drop, the heat duty of each segment is calculated using the effectiveness-NTU method. The output condition for a segment is calculated by subtracting the segment heat duty from the fluid enthalpy and the segment pressure drop from the fluid pressure at the segment inlet. The outlet conditions of a segment are taken as the inlet for the subsequent segment. The overall heat duty and UA for the furnace are obtained by summing up the contributions of the individual segments.

For the representative case considered, the overall heat transfer coefficient based on air-side heat transfer area is 110.2 W/m^{2}K (19.4 Btu/hr-ft^2-F) and the UA of the heat exchanger is 41.1 W/K (77.8 Btu/hr-ft^2-F).

APPENDIX C

C.1: Shell-and-Tube Heat Exchanger Design

This section explains the design for the water-to-HTF shell-and-tube heat exchanger. The design conditions for the heat exchanger are shown in Table C.1. The hot HTF flows through the tubes and water flows on the shell side. The water-HTF heat exchanger dimensions are listed in Table C.2. This heat exchanger is used for the following functions: i) HTF-to-water (open-loop); ii) HTF-to-water (closed-loop); and iii) Recuperation fluid-to-HTF heat transfer.

Table C.1: Design Conditions

	Tube-Side	**Shell-Side**
Fluid	HTF	Water
Inlet Temperatures, ^{o}C	311.1	27.0
Outlet Temperatures, ^{o}C	241.9	41.4
Mass flow rate, kg/sec	1.5	4
Allowable Pressure Drops, kPa	34.47 kPa (5 psi)	34.47 kPa (5 psi)
Heat Duty, kW	241.27	
UA, W/K	1000	
LMTD	241.3 K	

Table C.2: Heat Exchanger Dimensions

Parameter	**SI Units**	**British Units**
Shell Internal Diameter (D_s)	5.08 cm	2.00 in
Tube Outside Diameter (D_o)	6.35 mm	0.25 in
Tube Inside Diameter (D_i)	5.84 mm	0.23 in
Tube Wall Thickness	0.25 mm	0.01 in
Tube Pitch (Square) (P_T)	10.8 mm	0.43 in
Number of Baffles (N_B)	10	
Shell Length (L_s)	1.00 m	3.28 ft
Thickness of Baffles (t_b)	5 mm	0.19 in
Number of Tube-Side passes (n)	1	
Number of Tubes per pass (N_{tube})	14	

These values are selected to provide the UA required to cool the HTF to the desired temperature.

Tube-Side Calculations

The flow velocity of the HTF per tube is calculated as:

$$\mathrm{vel}_{\mathrm{tube}} = \frac{\mathrm{m}_{\mathrm{HTF,rate}}}{\rho_{\mathrm{HTF}} \cdot \mathrm{A}_{\mathrm{tube}}} \tag{C.1}$$

where $m_{HTF,rate}$ is the total mass flow rate of the HTF and A_{tube} is the total cross sectional area of the tubes (N_{tube} = 14). For the given mass flow rate of the HTF (1.5 kg/sec) and the cross-sectional area of the tubes (3.75E-4 m^2), the flow velocity is calculated to be 4.63 m/sec. The properties of the HTF are calculated at the mean temperature of the inlet and the outlet from the heat exchanger (@ T= 276.5^{o}C; ρ_{HTF} = 843.5 kg/m^3; μ_{HTF} = 4.598E-4 kg/m-sec; $C_{p,HTF}$ = 2384 J/kg-K; k_{HTF} = 0.098 W/m-K)

The Reynolds number is calculated from the following:

$$\mathrm{Re}_{\mathrm{tube}} = \frac{\rho_{\mathrm{HTF}} \cdot \mathrm{vel}_{\mathrm{tube}} \cdot \mathrm{D}_{\mathrm{i}}}{\mu_{\mathrm{HTF}}} \tag{C.2}$$

and is equal to 49577. The friction factor (f_{tube}) and Nusselt number (Nu_{tube}) based on the inner diameter (D_i) were calculated using correlations by Churchill (1977b; 1977a) to be 0.021 and 405.2 respectively. The heat transfer coefficient ($h_{coeff,tube}$) and the pressure drop (Δp_{tube}) on the tube side are as follows:

$$\mathrm{h}_{\mathrm{coeff,tube}} = \frac{\mathrm{Nu}_{\mathrm{tube}} \cdot \mathrm{k}_{\mathrm{HTF}}}{\mathrm{D}_{\mathrm{i}}} \tag{C.3}$$

$$\Delta \mathrm{p}_{\mathrm{tube}} = (1/2) \cdot \frac{\rho_{\mathrm{HTF}} \cdot f_{\mathrm{tube}} \cdot \mathrm{vel}_{\mathrm{tube}}^{\ 2} \cdot \mathrm{L}_{\mathrm{s}}}{\mathrm{D}_{\mathrm{i}}} \tag{C.4}$$

where L_s is the shell length of the heat exchanger. These are equal to 6807 W/m^2-K and 32.1 kPa (4.67 psi), respectively.

Shell-Side Calculations

The hydraulic diameter (D_e) on the shell side is given by the following:

$$D_e = \frac{4 \cdot \left(P_T{}^2 - \frac{\pi \cdot D_o{}^2}{4} \right)}{\pi \cdot D_o} \tag{C.5}$$

for a square pitch arrangement and is obtained to be 17 mm. The water properties are calculated at the mean temperature of the inlet and outlet (@ T= 34.21°C; ρ_{wtr} = 994.3 kg/m^3; μ_{wtr} = 7.31E-4 kg/m-sec; $C_{p,wtr}$ = 4179 J/kg-K; k_{wtr} = 0.622 W/m-K). Therefore, the Reynolds number is calculated from the following:

$$Re_{shell} = \left(\frac{\rho_{wtr} \cdot vel_{wtr} \cdot D_e}{\mu_{wtr}} \right) \tag{C.6}$$

where the velocity of water through the shell-side is calculated as follows:

$$vel_{wtr} = \frac{m_{wtr,rate}}{\rho_{wtr} \cdot A_s} \tag{C.7}$$

where $A_{s,}$ the crossflow area at the diameter of the shell is as follows:

$$A_s = \frac{D_s}{P_T} \cdot (P_T - D_o) \cdot L_B \tag{C.8}$$

where L_B, the baffle spacing in the shell is calculated using the following:

$$N_B = \frac{L_s}{L_B + t_b} - 1 \tag{C.9}$$

The mass flux of water through the shell-side is as follows:

$$G = \frac{m_{wtr,rate}}{A_s} \tag{C.10}$$

The Reynolds number for this configuration is obtained to be 51846 for a flow velocity of 2.24 m/sec. The crossflow area A_s is 1.79E-3 m^2, the baffle spacing is 8.59 cm and the mass flux is 2226 kg/m^2-sec. The pressure drop on the shell side is given by the following (Kern 1950):

$$\Delta p_{shell} = \frac{f_{shell} \cdot G^2 \cdot D_s (N_B + 1)}{2 \cdot \rho_{wtr} \cdot D_e} \tag{C.11}$$

where f_{shell} is the Churchill friction factor (Churchill 1977b). Substituting respective values, the friction factor and the pressure drop on the shell side are 0.021 and 1.68 kPa

(0.24 psi) respectively. The shell-side Nusselt number is calculated from the correlation provided by Kern (1950):

$$Nu_{shell} = 0.36 \cdot Re_{D_e}^{0.55} Pr^{1/3} \tag{C.12}$$

and is equal to 239.7.

The heat transfer coefficient is calculated as follows:

$$h_{shell,coeff} = Nu_{shell} \cdot \frac{k_{wtr}}{D_e} \tag{C.13}$$

to be 8763 W/m^2-K. Therefore, the effective size (UA) of the heat exchanger is as follows:

$$\frac{1}{UA} = \left(\frac{1}{h_{coeff,tube} \cdot A_i} + R_w + \frac{1}{h_{coeff,shell} \cdot A_o} \right) \tag{C.14}$$

where A_i (0.2569 m^2), A_o (0.2793 m^2) are the total heat transfer areas of the tubes based on the inner (D_i) and outer (D_o) diameters respectively and R_w is the wall resistance given by the following:

$$R_w = \frac{1}{2 \cdot \pi \cdot L_s \cdot k \cdot N_{tube}} \cdot \ln\left(\frac{D_o}{D_i} \right) \tag{C.15}$$

where k is the conductivity of the tubes (carbon steel) and is equal to 51.29 W/m-K. The values of the tube-side, wall and shell-side resistances are calculated to be 5.72E-4, 1.85E-5 and 4.08E-4 K/W respectively. The resulting UA of 1001.1 W/K satisfies the design requirement of UA = 1000 W/K.

REFERENCES

Attaran, M. T., Wright, E. J. and Crawford, R. J. (1998), "Computer Modelling of the Rotational Moulding Process," *Journal of Reinforced Plastics and Composites*, **17** (14): 1307-1318.

Beall, G. L. (1998). Rotational Molding : Design, Materials, Tooling, and Processing, Munich : Hanser Publishers ; Cincinnati : Hanser/Gardner Publications.

Bellehumeur, C. T. and Tiang, J. S. (2002), "Simulation of Non-Isothermal Melt Densification of Polyethylene in Rotational Molding," *Polymer Engineering and Science*, **42** (1): 215-229.

Bhatti, M. S. and Shah, R. K. (1987). Turbulent and Transition Flow Convective Heat Transfer in Ducts. Handbook of Single-phase Convective Heat Transfer. S. Kakac, R. K. Shah and W. Aung, Wiley-Interscience**:** 4.1-4.166.

Bruins, P. F. (1971). Basic Principles of Rotational Molding. New York, New York, Gordon and Breach.

Churchill, S. W. (1977a), "Comprehensive Correlating Equations for Heat, Mass and Momentum Transfer in Fully Developed Flow in Smooth Tubes," *Industrial & Engineering Chemistry, Fundamentals*, **16** (1): 109-116.

Churchill, S. W. (1977b), "Friction-Factor Equation Spans All Fluid-Flow Regimes," *Chemical Engineering (New York)*, **84** (24): 91-92.

Churchill, S. W. and Chu, H. H. S. (1975), "Correlating Equations for Laminar and Turbulent Free Convection from a Vertical Plate," *International Journal of Heat and Mass Transfer*, **18**: 1323.

Crawford, R. J. (1996). Rotational Moulding of Plastics, Taunton, Somerset, England : Research Studies Press ; New York : Wiley.

Crawford, R. J. and Nugent, P. J. (1992), "New Process Control System for Rotational Moulding," *Plastics, Rubber and Composites Processing and Applications*, **17** (1): 23-31.

Crawford, R. J. and Scott, J. A. (1985), "Experimental Study of Heat Transfer during Rotational Moulding of Plastics," *Plastics and Rubber Processing and Applications*, **5** (3): 239-248.

DOW (2004). High Temperature Thermal Fluids. http://www.dow.com/heattrans/high.htm.

Farrell, R. E., Fisher, K. J. and Johnson, D. H. (1996), "Rotational Mold System having Energy Storage and Recovery," *Proceedings of the 1996 ASME International Mechanical Engineering Congress & Exhibition*, Atlanta, GA, USA, ASME, New York, NY, USA, pp. 1-6.

Frados, J. (1976). Plastics Engineering Handbook of the Society of the Plastics Industry, Inc, New York : Van Nostrand Reinhold, pp. 348-356.

Gogos, G., Olson, L., Liu, X. and Pasham, V. R. (1997), "Computational Model for Rotational Molding of Thermoplastics," *Proceedings of the 1997 55th Annual Technical Conference, ANTEC. Part 3 (of 3)*, Toronto, Canada, Soc of Plastics Engineers, Brookfield, CT, USA, pp. 3216-3219.

Gogos, G., Olson, L. G., Liu, X. and Pasham, V. R. (1998), "New Models for Rotational Molding of Plastics," *Polymer Engineering and Science*, **38** (9): 1387-1398.

Griffith, R. and Nassersharif, B. (1990), "Comparison of One-dimensional Interface-following and Enthalpy Methods for the Numerical Solution of Phase Change," *Numerical Heat Transfer, Part B (Fundamentals)*, **18** (2): 169-187.

Hilpert, R. (1933), *Forsch. Geb. Ingenieurwes.*, **4**: 215.

Incropera, F. P. and DeWitt, D. P. (1996). Introduction to Heat Transfer, John Wiley and Sons.

Kays, W. M. and London, A. L. (1984). Compact Heat Exchangers, New York : McGraw-Hill.

Kern, D. Q. (1950). Process Heat Transfer, McGraw-Hill, New York.

Klein, S. A. (2003). Engineering Equation Solver.

Krott, A. M. (1995), "A Comparison between Hot-Oil and Conventional Mold Heating for Rotational Molding," *Proceedings of the 53rd Annual Technical Conference. Part 3 (of 3)*, Boston, MA, USA, Soc of Plastics Engineers, Brookfield, CT, USA, pp. 4342-4346.

Liu, G., Park, C. B. and Lefas, J. A. (1998), "Rotational Molding of Low-Density LLDPE Foams," *Proceedings of the 1998 56th Annual Technical Conference, ANTEC. Part 2 (of 3)*, Atlanta, GA, USA, Soc Plast Eng, Brookfield, CT, USA, pp. 1822-1831.

Liu, S.-J. and Tsai, C.-H. (1999), "An Experimental Study of Foamed Polyethylene in Rotational Molding," *Polymer Engineering and Science*, **39** (9): 1776-1786.

Merrill, R. F. (1979), "Calculating Heat-Exchanger Capacity for a Heat-Recovery System," *Plastics Engineering*, **35** (8): 30-32.

Natarajan, N. M. and Lakshmanan (1972), "Laminar Flow in Rectangular Ducts: Prediction of Velocity Profiles and Friction Factor," *Indian Journal of Technology*, **10** (12): 435-438.

Nugent, P. J. (1990). "A Study of Heat Transfer and Process Control in the Rotational Moulding of Polymer Powders," PhD, Queen's University of Belfast (Northern Ireland)

Nugent, P. J., Crawford, R. J. and Xu, L. (1992), "Computer Prediction of Cycle Times During Rotational Molding of Plastics," *Advances in Polymer Technology*, **11** (3): 181-191.

Olson, L. G., Gogos, G., Pasham, V. and Liu, X. (1997), "Numerical Modeling for Rotational Molding of Thermoplastics," *Proceedings of the 1997 ASME International Mechanical Engineering Congress and Exposition. Part 1 (of 3)*, Dallas, TX, USA, ASME, Fairfield, NJ, USA, pp. 113-119.

Olson, L. G., Gogos, G., Pasham, V. and Liu, X. (1998), "Axisymmetric Finite Element Models of Rotational Molding," *Proceedings of the 1998 56th Annual Technical Conference, ANTEC. Part 1 (of 3)*, Atlanta, GA, USA, Soc Plast Eng, Brookfield, CT, USA, pp. 1116-1120.

Purday, H. F. P. (1949). An Introduction to the Mechanics of Viscous Flow; Film Lubrication, the Flow of heat by Conduction and Heat Transfer by Convection. New York, Dover.

Rao, M. A. and Throne, J. L. (1972), "Principles of Rotational Molding," *Polymer Engineering and Science*, **12** (4): 237-264.

Scott, J. A. (1986). "A Study of the Effect of Process Variables on the Properties of Rotationally Moulded Plastic Articles," PhD, Mechanical Engineering, Queen's University of Belfast.

Shah, R. K. and London, A. L. (1978). Laminar Flow Forced Convection in Ducts: A Source Book for Compact Heat Exchanger Analytical Data. New York, Academic Press.

Sun, D.-W. and Crawford, R. J. (1993), "Computer Simulation of Rotational Moulding Heat Transfer Processes," *Plastics, Rubber and Composites Processing and Applications*, **19** (1): 47-53.

Sunden, B. and Svantesson, J. (1992), "Correlations of j - and f - factors for Multilouvered Heat Transfer Surfaces," *3rd UK National Conference incorporating 1st European Conference on Thermal Sciences*, Birmingham, Engl, Publ by Inst of Chemical Engineers, Rugby, Engl, pp. 805-811.

Tadmor, Z. and Gogos, C. G. (1979). Principles of Polymer Processing. New York, John Wiley and Sons, Inc.

Throne, J. L. (1976), "Rotational Molding Heat Transfer - An Update," *Polymer Engineering and Science*, **16** (4): 257-264.

Touloukian, Y. S. and Ho, C. Y. (1972). Thermophysical Properties of Matter, Plenum Press, New York.

Xu, L. and Crawford, R. J. (1994), "Computer Simulation of the Rotational Moulding Process," *Plastics, Rubber and Composites Processing and Applications*, **21** (5): 257-273.